High-Power Ultrafast Light

Generation of 1 ps-to-70 fs, 5 mJ-to-μJ Pulses and Low-Harmonic-Generation at High Repetition Rates

Lauryna Petraviciute - Lötscher

SIGILL·UNIVERSITAT·LUDOVIC·MAXIM

München 2020

High-Power Ultrafast Light

Generation of 1 ps-to-70 fs, 5 mJ-to-μJ Pulses and Low-Harmonic-Generation at High Repetition Rates

Lauryna Petraviciute - Lötscher

Dissertation
an der Fakultät für Physik
der Ludwig–Maximilians–Universität
München

vorgelegt von
Lauryna Petraviciute - Lötscher

München, den 12. Dezember 2019

Erstgutachter: Prof. Dr. Ferenc Krausz
Zweitgutachter: Prof. Dr. Monika Aidelsburger
Tag der mündlichen Prüfung: 8. Mai 2020

To my Grandmother

Contents

List of Figures

List of Tables

List of Acronyms

AOM acousto-optic modulator

CEP carrier-envelope phase

COLTRIMS cold target recoil ion magnetic spectroscopy

CPA chirped-pulse amplification

DFG difference frequency generation

DFWM degenerated four-wave mixing

FWM four-wave mixing

GDD group delay dispersion

HHG high-order harmonic generation

HNLF highly nonlinear photonic crystal fiber

LHG low-order harmonic generation

LMA large mode area

MED multi-electron dynamics

MFD mode field diameter

NOPA noncollinear optical parametric amplifier

NPC nonlinear pulse compression

OHG optical harmonic generation

OPA optical parametric amplifier

OPCPA optical parametric chirped pulse amplifier

PCF photonic crystal fiber

PLL phase lock loop

SFG sum-frequency generation

SHG second harmonic generation

SPM	self-phase modulation
SSFS	soliton self-frequency shift
TOD	third order dispersion
VMI	velocity map imaging
WLG	white light generation
XPW	cross polarized wave generation
ZDW	zero order dispersion wavelength

Abstract

The largest laboratories on Earth are accelerator-based particle and light sources, generating EUV, X-ray and high-energy particle beams. These facilities are extremely important for humankind as sources of treatments for various serious diseases such as cancer [5, 6, 7]. They are also important for fundamental research in different fields, such as molecular, biophysics [8, 9, 10, 11, 12], and particle physics [13, 14]. An alternative technique for generation of this ionising radiation is optical harmonic generation (OHG) with carrier-envelope phase (CEP) stable femtosecond table-top lasers [15, 16]. Using this technology, coherent ultrashort EUV and X-ray radiation [17, 18] have been generated [19, 20] and applied to time-resolved (pump-probe) experiments [21, 22]. These table-top sources allow studies of one of the grand questions of quantum physics: multi-electron dynamics (MED). This is done using different experimental techniques, such as cold target recoil ion magnetic spectroscopy (COLTRIMS) for investigation of non-sequential double ionization [23] and velocity map imaging (VMI) combined with CEP tagging [24]. With the development of few-cycle intense femtosecond lasers a new epoch of physics, attosecond science, was founded [25]. We also note that particle acceleration can be driven by ultrashort laser pulses [26, 27, 28].

For the applications detailed above, data acquisition time and statistics can be significantly improved using higher repetition rates and thus higher average powers. Also, for free-electron laser facilities, increased repetition rate of laser pulses would be beneficial for laser pump and X-ray probe methodologies [29]. Frequency comb spectroscopy in EUV [30] would profit from repetition rates at multi-megahertz, because the distance between the comb lines in a frequency domain are proportional to the repetition rate, thus the repetition rate should be high enough for comb lines to be well resolved [31]. OHG at multi-megahertz repetition rate opens the door for amazing applications, such as spectroscopy of hydrogenic systems [32], investigation on variations of fundamental constants [33], and time of flight photoelectron emission microscopy with attosecond pulses [34]. Additionally, investigations on DNA and other bio-molecules can be performed using table-top coherent X-ray sources in the water window (4.4 - 2.3 nm) with high contrast and spatial resolution [35].

Common laser sources for experiments described above are Ti:sapphire chirped pulse amplifiers with nonlinear pulse compression (NPC) or Ti:sapphire front-end optical parametric chirped pulse amplifier (OPCPA). Ti:sapphire chirped pulse amplifiers require complex cooling to reach 10s of watts so this technology can not be scaled further to high average powers [36]. In contrast, an OPCPA has the advantage of a low thermal load on the amplification medium and so is more scalable. However, it requires appropriate pump lasers emitting average power up to kilowatts [37, 38]. Even if a high average pump power can cause heating due to absorption of crystals [39], this can be solved by using high quality nonlinear crystals characterized by a low absorption of the pump radiation [40, 41]. Previously demonstrated high power OPCPA systems were with a Ti:sapphire frontend, meaning that a Ti:sapphire oscillator provides a seed for an OPCPA and a seed for a pump. Even if using the same frontend ensures optical synchronization between seed and pump, slow temporal drifts and fast jitters in the laser amplifier system are not compensated completely [42]. Active stabilization has been shown to improve the stability significantly, however, it is limited to Ti:sapphire amplifiers, since the active stabilization requires a high power broadband seed [42]. Thus, the reliable and stable generation of a broadband seed from a narrowband Yb amplifier is very important for the further scaling of OPCPA systems.

In laser technology, Ytterbium ions (Yb^{3+}) have secured a prominent role as laser-active dopants in crystals and glasses. Commercially available Yb-doped materials have good optical and thermo-mechanical properties. Due to the low number of quantum defects it can be pumped efficiently by high-power diode laser modules and therefore has scalable average power. This is a significant advantage, since numerous applications, such as attosecond metrology, demand or at least highly profit from a laser system with high repetition rates of 100 kHz - 100 MHz. Due to high repetition rates data acquisition time and statistics can be significantly improved. However, as a gain material Yb has a serious drawback for ultrashort applications: it is intrinsically narrowband with correspondingly long (in a range of hundreds of femtoseconds to picoseconds) generating and/or amplifying pulses. This disadvantage can be partially solved by implementing NPC techniques.

In this thesis, NPC in solid core fibers is investigated in details at different repetition rates. A reliable and simple NPC setup for μJ-level pulses is demonstrated, wich can be used as part of a larger system for applications such as time-resolved electron diffraction to investigate atomic motion during chemical and biological processes. Results show that, for OPCPA, a broadband seed can also be successfully generated from picosecond Yb-based laser sources at kHz and MHz repetition rates.

A high power laser at 100 kHz repetition rate, based on Yb laser technology was developed; its purpose was to pump a broadband OPCPA. Complicated synchronization schemes between a pump and a seed can be avoided by direct generation of a broadband seed from a pump laser, which simplifies the overall setup significantly and allows further scaling in average power.

Finally, extreme ultraviolet (EUV, 10 - 121 nm) generation using an Yb laser at 50 MHz repetition rate is reported. EUV generation at multimegahertz repetition rate is a rapidly growing field of high interest, however, because of low efficiency of the process it is necessary to have a high photon flux. This spectral region is available through OHG techniques such as low-order harmonic generation (LHG) and high-order harmonic generation (HHG). Two different approaches are followed: cavity-assisted OHG [1, 2] and single-pass OHG [3, 4]. There are several advantages of a single-pass OHG compared to a cavity-assisted OHG, mainly that several experimental conditions can be easily controlled, such as repetition rate and quasi-phase matching. On the other hand, cavity-assisted OHG can more easily achieve high intensities, but it is harder to couple light out of the cavity effectively.

Outline of the thesis and the main results

Chapter 1 provides an overview of the generation of femtosecond pulses at high average powers. Firstly, nonlinear pulse compression (NPC) is described and its impact to the laser physics is reviewed. The value of a group delay dispersion (GDD) necessary to compress a broadband continuum is estimated theoretically, with two different regimes defined depending on the laser input parameters. Secondly, optical parametric amplifiers are described with a focus on the performance at high average power. The description is followed by advantages and disadvantages of a Ti:sapphire- and a Yb-frontend. In addition, different synchronization techniques between pump and seed are discussed. Thirdly, all the types of high power Yb laser designs, such as fiber, regenerative, and Innoslab lasers, are presented briefly. Finally, challenges of LHG at high repetition rates are discussed.

Chapter 2 presents the experimental results of NPC at repetition rates from kilohertz to multi-megahertz. The study concentrates on solid-core large mode area (LMA) photonic-crystal fibers (PCF). Different properties of the system are investigated in detail, such as the long-term stability, the maximal compression factor, the polarization extinction ratio, and the damage threshold. In addition, different realizations of further spectral broadening and second stage compression are addressed. The results show that a broadband seed for an OPCPA can be generated from a narrowband Yb-based laser source at kHz and MHz repetition rates by combining spectral broadening in a fiber and supercontinuum generation in a bulk material.

Chapter 3 presents the design and the realization of a high average power laser at 100 kHz repetition rate. The purpose of the laser was to pump high power few-cycle CEP-stable OPCPA. All the state-of-art techniques of high-power Yb-based amplifiers, described in Chapter 1, were brought together to build a pump laser. The required seed can be provided by a broadband Ti:sapphire oscillator or generated from a narrowband Yb laser, as shown in Chapter 2. Both Ti:sapphire- and Yb-frontend OPCPA schemes were considered regarding their advantages and disadvantages.

Low-harmonic generation using a Yb laser at 50 MHz repetition rate is reported in Chapter 4. The powers generated in extreme ultraviolet are not comparable to those produced by cavity-assisted LHG. However, following rapid progress in the amplifier development, single-pass LHG may compete with a cavity-assisted multi-MHz LHG sources for establishing a versatile, easy to operate, table-top, high repetition rate EUV source for the frequency-comb spectroscopy and other applications in near future.

The measurements in Chapter 2 at 3 kHz, 50 kHz, and at 11 MHz repetition rates were performed by me. The measurements of the second spectral broadening stage in a bulk at 11 MHz repetition rate were performed together with Dr. Hanieh Fattahi and Dr. Thomas Ganz. The measurements at 20 MHz repetition rate were performed together with Thomas Sartorius and Dr. Johannes Weitenberg at ILT, Aachen. The realization of the stretcher and compressor in Chapter 3 was completed together with Harald Fuest. The experiments described in Chapter 4 were performed with Dr. Waldemar Schneider.

In Chapter 1, the formula of GDD due to self-phase modulation was derived by Dr. László Veisz. The published version of the formula differs from that used in this thesis, because it was derived in the context of a different investigation [43]. For clarity, the formula is introduced in the theoretical section of this thesis.

Claims

- The long-term stabilisation of 70 fs pulses derived from 1 ps pulses in a nonlinear fiber-compressor was demonstrated for the first time [44]. This is significant for several demanding nonlinear applications.
- A robust chain consisting of Yb-doped fiber amplifiers and an Innoslab laser amplifier (with 100 kHz repetition rate and 5 mJ pulse energy) was realized for the first time. It was used for the generation of CEP-phase stable few-cycle pulses by OPCPA and DFG processes for investigations of ultrafast phenomena in atoms and molecules [45].
- Single-pass generation of low harmonics (LHG) in gas at 50 MHz repetition rate was demonstrated for the first time, showing that single-pass LHG may compete with the intracavity LHG technique as an EUV source [46]. A significant advantage of a single-pass LHG technique compared to an enhancement cavity is the absence of complex output coupling.

Publications

- P. Wnuk, H. Fuest, M. Neuhaus, L. Lötscher, E. Riedle, Z. Major, P. Rußbüldt, D. Hoffmann, F. Krausz, and M. F. Kling, “Discrete dispersion scanning as a simple method for broadband femtosecond pulse characterization,” *Opt. Express*, vol. 24, pp. 18551-18558, 2016.

  The design and the realization of the laser system used for these experiments are given in chapter 3.

- L. Lötscher, L. Vámos, L. Veisz and A. Apolonski, “Long-term stability of nonlinear pulse compression using solid-core large-mode-area fibers,” *J. Laser Opt. Photon.*, vol. 2, pp. 1-5, 2015.

  A detailed description of the experiment and the results of this paper are given in chapter 2.

Conference contributions

- M. Seidel, X. Xiao, A. Hartung, O. Pronin, L. Lötscher, A. Apolonski, and F. Krausz, “Spectral broadening and peak power limitations of normally dispersive photonic crystal fibres for high-power fs light sources,” in *Lasers and Electro-Optics Europe (CLEO EUROPE/IQEC)*, IEEE, 2015.

  The experimental data for the conference contribution are described in chapter 2.

- L. Lötscher, W. Schneider, P. Rußbüldt, B. Gronloh, H. D. Hoffmann, M. F. Kling, and A. Apolonski, “Direct low-harmonic generation in gas at MHz repetition rate,” in *Lasers and Electro-Optics Europe (CLEO EUROPE/IQEC)*, IEEE, 2013.

  A detailed description of the experiment and the results of the conference contribution are given in chapter 4.

Chapter 1

Realization of femtosecond pulses at high average power

In this chapter, different techniques for ultrashort pulse generation at high average power are reviewed, such as nonlinear pulse compression (section 1.1), optical parametric chirped-pulse amplification (section 1.2), and ultrafast lasers (section 1.3). Additionally, we discuss the importance of high power femtosecond Ytterbium lasers as pumps for high power, few-cycle, optical parametric chirped-pulse amplifiers. Techniques for the EUV generation are described in section 1.4.

1.1 Nonlinear pulse compression

The concept of nonlinear pulse compression is simple as shown in Fig. 1.1. In the first step, the optical bandwidth is increased, typically with a nonlinear interaction such as self-phase modulation (SPM), leading to chirped pulses. Different spectral broadening platforms (bulk and waveguides) can be used depending on laser input parameters. In the second step, the pulse duration is strongly reduced by a compressor: a grating compressor, a prism pair, or chirped mirrors.

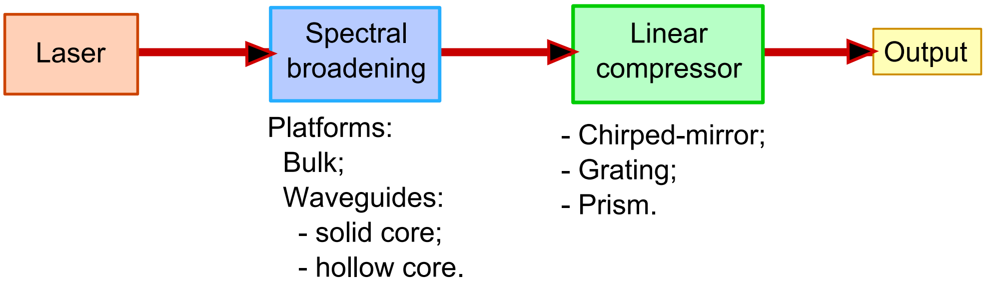

Figure 1.1: Concept of nonlinear pulse compression.

1.1.1 Overview

In the history of laser development, nonlinear pulse compression (NPC) has played a significant role in reducing the pulse duration, with this technique holding the record value for pulse duration for a long time (Table 1.1). NPC with a spectral broadening in a single mode silica fiber was first demonstrated in 1981, when input pulses of 5.5 ps duration were compressed to 1.5 ps [47]. The paper focused on the temporal profile measurements of chirped pulses to indicate changes induced by self-phase modulation. NPC swiftly gained attention when the record for shortest pulses was beaten in 1982 (30 fs) with a reported compression factor of 3 [48]. One year later, a compression factor of 65 with 2 stages of NPC was demonstrated [49]; the input pulse duration was 6 ps and the output 90 fs. Thereafter, shorter and shorter pulses were generated approaching a fundamental limit of a single wave cycle [50, 51, 52, 53, 54, 55, 56, 57]. Pulse energies did not exceed nJ-level using solid core fibers (step-index or photonic-crystal fibers with a core diameter of a few-micrometers) due to the damage threshold of these waveguides.

Table 1.1: Chronological overview of nonlinear pulse compression

Year	Input → output pulse duration	Remarks	Ref.
1981	5.5 ps → 1.5 ps	First implementation of fibers	[47]
1982	90 fs → 30 fs	Shortest pulses	[48]
1983	6 ps → 90 fs	Compression factor 65, 2 stages	[49]
1984	65 fs → 16 fs	Shortest pulses	[50]
1984	110 fs → 12 fs	Shortest pulses	[51]
1985	40 fs → 8 fs	Shortest pulses	[52]
1987	50 fs → 6 fs	Shortest pulses	[53]
1996	140 fs → 10 fs	240 μJ, 1 kHz	[58]
1997	13 fs → 4.9 fs	Shortest pulses	[54]
1997	20 fs → 4.5 fs	Shortest pulses, 20 μJ, 1 kHz	[55]
2003	810 fs → 33 fs	μJ-level, 34 MHz	[60]
2003	9 fs → 4 fs	nJ-level, 24 MHz	[56]
2009	800 fs → 68 fs	μJ-level, 30 kHz	[67]
2011	480 fs → 35 fs	μJ-level, 50 kHz	[68]
2011	6 fs → Shortest pulses, 3.6 fs	nJ-level, 76 MHz	[57]
2013	340 fs → 26 fs	mJ-level, 250 kHz	[69]
2015	250 fs → 7.7 fs	μJ-level, 38 MHz	[70]

NPC with spectral broadening in a gas filled capillary was shown, reaching hundredths of μJ pulses [58, 55]. Critical self-focusing in gas, as a fundamental limit of a damage threshold, happens at orders of magnitude higher peak power than in glass. This is because self-focusing is proportional to the nonlinear refractive index [59], which is significantly lower in gas compared to glass. This progress was based on a Ti:sapphire chirped pulse amplifier approach, which in combination with NPC, enabled extraordinary experiments and a new field of physics: attosecond science [25]. The technology opened the door to few-cycle pulses of high intensities. Unfortunately, Ti:sapphire amplifiers require complex pump lasers and cooling in order to reach tens of watts of average power and are no-longer scalable [36]. A number of applications would profit from high pulse repetition rates (and average power), because data acquisition time and statistics could be significantly improved.

NPC was further extended to high average powers and μJ-level pulse energies by using Yb:YAG oscillators and new types of waveguides, such as solid-core large-mode area (LMA) fibers [60, 61, 62] and kagomé fibers [63, 64, 65]. These waveguides belong to the class of photonic crystal fiber (PCF) and have an advantage over step-index fibers due to the flexibility of their design, allowing a wide range of important properties to be modified easily. The core of LMA fibers can be larger by more than a factor of 10 over the core of a conventional single mode step-index fiber. At core of kagomé fibers, is a hole that can be filled with gas in a similar way to a capillary. The advantage of a kagomé over a capillary is that its core can be smaller than that of a capillary whilst maintaining low transmission losses. Transmission losses of capillary increase rapidly if its core is smaller than 100 μm [66]. A smaller size of a core is crucially important for working with μJ-level few-picosecond input pulses, this is especially true for Yb:YAG oscillators.

NPC with a spectral broadening in a kagomé is the newest and the most promising way to compress pulses at high repetition rates and high pulse energies, derived from Yb:YAG oscillators and amplifiers. It is important to note that, in order to reach stable operation while operating with gas pressure of a few bar, one needs to overcome thermal problems. However, there are still outstanding questions regarding solid core NPC, and there are applications interested in a reliable and simple NPC setup for μJ-level pulses to be used within a larger system, for example: OPCPA seed generation and time-resolved electron diffraction. Due to the development of high power Yb fiber amplifiers, NPC with a spectral broadening in hollow core fibers has been demonstrated at tenths and hundredths of kHz repetition rates [67, 68, 69]. Pulses as short as sub-100 fs at μJ-level were reported, however, these did not reach a few-cycle regime. Reasons for these problems will be discussed in Chapter 3.

In summary:

- By combining NPC with spectral broadening in a fiber and supercontinuum generation in a bulk, 250 fs pulses from a Yb:YAG oscillator were compressed to few-cycle pulses (7.7 fs). In addition, CEP stabilization by means of an intra-cavity acousto-optic modulator (AOM) was realized. [70].

- A similar approach can be used to generate a broadband seed for an OPCPA from an Yb amplifier. Since this seed generation setup is a part of a larger and more complex system, its long-term stability is crucially important.

- Some questions are unanswered regarding solid core NPC, and there are applications interested in a reliable and simple NPC setup for μJ-level pulses for use within larger systems such as OPCPA and time-resolved electron diffraction. The main open question is the long term stability of NPC.

1.1.2 Theoretical background

A good overview of nonlinear effects in fibers can be found in [59]. The induced polarization of a medium by light can be written as:

$$\mathbf{P} = \epsilon_0(\chi^{(1)} \cdot \mathbf{E} + \chi^{(2)} : \mathbf{E}\ \mathbf{E} + \chi^{(3)} \vdots \mathbf{E}\ \mathbf{E}\ \mathbf{E} + ...) \tag{1.1}$$

where ϵ_0 is the vacuum permittivity; $\mathbf{E}$ – electric field vector; $\chi^{(j)}$ is the electrical susceptibility, represented as a tensor of rank $j+1$.

The fiber response to light becomes nonlinear for intense electromagnetic fields. Quadratic effects such as second harmonic generation (SHG), sum-frequency generation (SFG), and difference frequency generation (DFG) are described by $\chi^{(2)}$. These quadratic effects are negligible in glass, because SiO_2 is a symmetric molecule. Nonlinear effects such as self-phase modulation (SPM), four-wave mixing (FWM) can be described by the tensor $\chi^{(3)}$. The polarization extinction ratio of broadened spectra is reduced, because $\chi^{(3)}$ is also responsible for the origin of the nonlinear polarization rotation [59, 71]. The nonlinear polarization rotation is an intensity-dependent change in the polarization state, it is usually a change to an elliptical polarization state rather than a simple rotation of a linear polarization [72].

SPM refers to the self-induced phase shift during propagation in a medium and can be described by the intensity and time dependent refractive index:

$$n(t) = n_0 + n_2 I(t), \tag{1.2}$$

where n_0 – linear refractive index; n_2 – nonlinear refractive index; $I(t)$ – optical intensity.

As pulses propagate, the intensity at any one point in the medium changes, thus producing a time-varying refractive index:

$$\frac{dn(I)}{dt} = n_2 \frac{dI}{dt} \tag{1.3}$$

Let us consider a Gaussian pulse with the complex temporal electric field $\tilde{E}(t)$:

$$\tilde{E}(t) = E(t)e^{i\Phi(t)}, \tag{1.4}$$

where $E(t)$ is the amplitude function of the electric field and $\Phi(t)$ is the phase function:

$$\Phi(t) = \omega_0 t - k(t)L, \tag{1.5}$$

where k – wave vector and L is fiber length. The wave vector is defined as following:

$$k(t) = \frac{2\pi n(t)}{\lambda}, \tag{1.6}$$

where n is given by Eq. 1.2 and λ is the central wavelength of a laser.

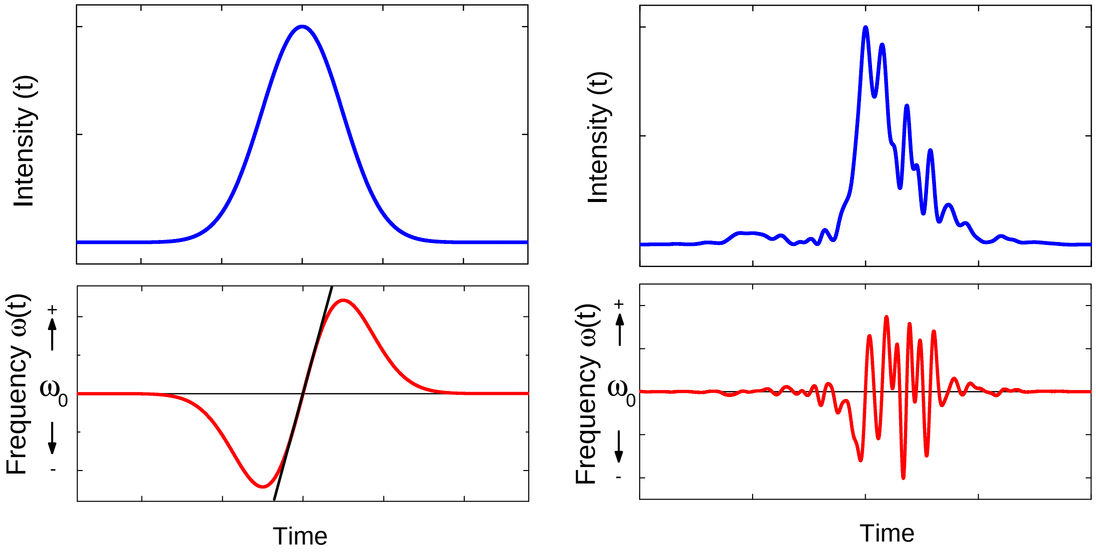

Figure 1.2: A pulse with a Gaussian and a non-Gaussian shape (blue curves) undergoes a self-frequency shift due to SPM. Pulses are shifted to lower and higher frequencies (red curves). The instantaneous frequency peaks once (repeatedly) within the pulse duration for a pulse with a Gaussian (non-Gaussian) shape. In the center of a Gaussian pulse the frequency shift is approximately linear (black line).

The variation in refractive index produces a shift in the temporal phase of the pulse $\Phi(t)$. This phase shift results in a frequency shift of the pulse. The instantaneous frequency is given by:

$$\nu(t) = \frac{1}{2\pi}\frac{d\Phi}{dt} \propto \frac{dn(I)}{dt} = n_2\frac{dI}{dt}. \tag{1.7}$$

In Fig. 1.2 pulses with a Gaussian and a non-Gaussian shape (blue curves) are shown undergoing a self-frequency shift due to SPM (red curves). Pulses are shifted to lower and higher frequencies as shown in the red curves. For a Gaussian pulse, instantaneous frequency has a single maximum and a single minimum. Each instantaneous frequency is repeated twice. The frequency shift is approximately linear in the center of the pulse (black line). For a non-Gaussian pulse, the same spectral components are generated, but with a different time dependency, meaning that the frequency peaks multiple times. This results in a complex spectral phase, which is hard to compensate.

To the best of our knowledge, a systematic investigation of compressor dispersion has not yet been performed. We apply the term dispersion to a compressor (and materials), whereas chirp is used to describe the pulse. A pulse is characterised by temporal amplitude and phase. The lower limit of the pulse duration for a given optical spectrum is called the transform limit (or Fourier limit), this is achieved when spectral phase is frequency independent. To understand this, let us consider the intensity of a Gaussian pulse (as given by Eq. 1.4) at the $1/e^2$ beam radius:

$$I(t) = I_0 e^{-4(ln2)\frac{t^2}{\tau_p^2}} \approx I_0(1 - 4(ln2)\frac{t^2}{\tau_p^2}), \tag{1.8}$$

where I_0 is the average intensity and τ_p is the full-width-half-maximum (FWHM) pulse duration. When using fibers the beam radius equals half of the mode field diameter (MFD) of the fiber. Here we approximate the Gaussian function with a parabola by Taylor expansion in order to simplify the derivatives required. For a Gaussian beam with peak power P and a $1/e^2$ radius of w, the average intensity on the beam axis is:

$$I_0 = \frac{P}{\pi w^2} \tag{1.9}$$

The peak power P is found from τ_p and the pulse energy E_p:

$$P \approx \frac{0.94 E_p}{\tau_p} \tag{1.10}$$

The spectrum $\tilde{E}(\omega)$ is calculated via Fourier transformation:

$$\begin{aligned}
\tilde{E}(\omega) &= E(\omega)e^{i\varphi(\omega)} \\
&= \int_{-\infty}^{\infty} \tilde{E}(t)e^{-i\omega t}dt \\
&= \int_{-\infty}^{\infty} E_0 e^{-at^2+i(\omega_0 t+bt^2+c)}e^{-i\omega t}dt \\
&= E_0 e^{ic}\sqrt{\frac{\pi}{a-ib}}e^{-\frac{(\omega-\omega_0)^2}{4(a-ib)}} \\
&= E_0 e^{ic}\sqrt{\frac{\pi(a+ib)}{a^2+b^2}}e^{-\frac{(\omega-\omega_0)^2}{4(a^2+b^2)}(a+ib)}.
\end{aligned} \tag{1.11}$$

$$a = \frac{2(ln2)}{\tau_p^2}$$
$$b = \frac{8\pi(ln2)n_2 I_0 L}{\lambda\tau_p^2} = \frac{4\pi n_2 I_0 L}{\lambda}a$$
$$c = \frac{2\pi L}{\lambda}(n_0 + n_2 I_0)$$

where ω denotes circular frequency, ω_0 is the carrier frequency, and φ is the spectral phase.

The spectral phase can be expanded in Taylor series around the carrier frequency ω_0, if it varies slowly with the frequency ω, allowing each derivative to be compensated separately using materials or a compressor, such that the derivatives of phase are equal to zero.

$$\varphi(\omega) = \varphi_0 + \frac{\partial\varphi}{\partial\omega}|_{\omega_0}(\omega - \omega_0) + \frac{1}{2}\frac{\partial^2\varphi}{\partial\omega^2}|_{\omega_0}(\omega - \omega_0)^2 + ..., \tag{1.12}$$

where φ_0 is the absolute phase of the pulse.

Group delay dispersion (GDD) and third order dispersion (TOD) are first and second order approximations of the compensation which can be applied using materials and compressors. The GDD is given by the second partial derivative of φ with respect to ω. This means that Eq. 1.11 can be used to calculate the GDD contribution to SPM:

$$GDD_{SPM} = \frac{\partial^2\varphi}{\partial\omega^2}|_{\omega_0} = -\frac{b}{2(a^2 + b^2)} \tag{1.13}$$

Since $b >> a$, we can reduce this to:

$$GDD_{SPM} \approx -\frac{1}{2b} \tag{1.14}$$

Finally, we can combine equations 1.11 and 1.14 to give:

$$GDD_{SPM} = -\frac{\lambda\tau_p^2}{16\pi(ln2)n_2 I_0 L} \tag{1.15}$$

The total GDD of a linear dispersion compressor is calculated by summing the contributions from chromatic dispersion and SPM. Chromatic dispersion means that the phase velocity and the group velocity (also described by the linear refractive index) is different for different wavelengths. The dependence of the linear refractive index on wavelength is given by an empirical relationship, known as the Sellmeier equation. Coefficients of the Sellmeier equation for fused silica can be found in [73, 74]. The value of the GDD from chromatic dispersion is given by [59]:

$$GDD_{chromatic} = \frac{\lambda^3 L}{2\pi c^2}\frac{d^2 n(\lambda)}{d\lambda^2} \tag{1.16}$$

Two different regimes can be defined, because the SPM GDD is proportional to the square of the input pulse duration (Eq. 1.15):

1. For long input pulses (around 1 ps available from Yb lasers), the SPM GDD can be significantly larger than the chromatic dispersion GDD.
2. For short input pulses (sub-100 fs, available, for example, from Ti:Sapphire systems), the SPM GDD can be neglected. This may explain the lack of literature addresing in SPM GDD.

SPM is a dominant nonlinear effect responsible for the increase of the optical bandwidth. However, especially for a supercontinuum generation, different nonlinear effects still play a role, for example: FWM [75] and cross polarized wave generation (XPW) [76].

1.2 Optical parametric chirped pulse amplifiers

Optical parametric amplifiers allow generating high-energy pulses in the spectral ranges where no lasers exist. The principle of an optical parametric amplifier (OPA) can be described as follows: in an appropriate nonlinear crystal energy is transferred from a higher frequency and intensity laser beam (pump) to a lower frequency and intensity laser beam (seed). In addition, a third beam (idler) is generated. For a broadband seed (> octave) amplification, noncollinear optical parametric amplifier (NOPA) was developed. Noncollinear geometry leads to the highest gain bandwidths for an OPA. Phase matching conditions in noncolinear geometry result in an angularly dispersed idler wave. It is illustrated by the phase-matching wave-vector triangle in Fig. 1.3.

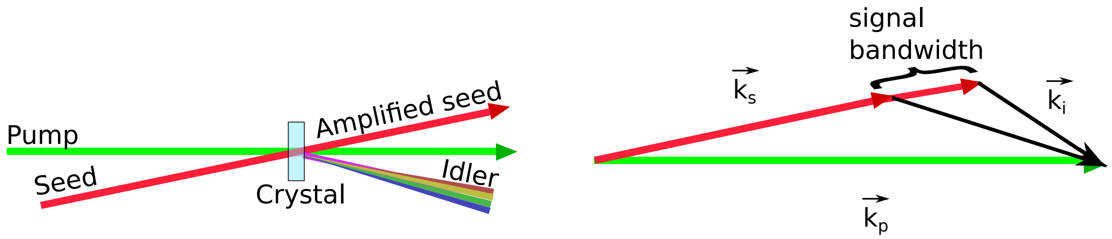

Figure 1.3: Concept of noncollinear optical parametric amplification (left) with phase-matching wave-vector triangle (right).

Phase matching is a key requirement for an efficient energy transfer from a pump to a signal and an idler. An OPA can satisfy the phase matching condition over a very broad frequency range. Thus, the efficient energy transfer from an intense narrowband pump laser to a weak broadband seed laser is feasible. This technique became especially powerful after a combination with a chirp pulse amplification of a seed [77, 78]. The idea enabled generation of peak power reaching petawatts. Besides a very high and a broadband gain, a thermal load on a nonlinear crystal is negligible, because the parametric process deposits no energy in the nonlinear medium. That is why, an OPCPA is a suitable technique to generate ultrashort pulses at mJ-level pulse energies and hundreds of kHz and MHz repetition rates.

It is important to note, that the **gain of an OPA** depends not only on the crystal length, but also on the **pump intensity**. A large bandwidth and a high gain in the OPA can be achieved by using high pump intensity and a short crystal. Since the limits of intensity resulting from either the nonlinear processes or damage should not be exceeded, short pump pulses (<10 ps) are preferable [79]. The length of the pump pulse should be shorter than the thickness of the nonlinear crystal in the OPA to avoid parasitic oscillation and amplification of post-pulses due to reflections of the amplified seed pulses from the crystal surfaces [80]. The condition is well fulfilled by 1 ps pulses, since their spatial length is significantly less than 1 mm in a crystal. A high average power few-cycle OPCPA reaching petawatt peak powers requires a robust, ultrashort, and high power pump source. Luckily, the second and third harmonic of Yb lasers (described in section 1.3) fulfill these requirements.

1.2.1 Pump-seed synchronization

Pump-seed synchronization is crucially important for a stable output of an OPCPA. The synchronization is especially aggravated with short pump pulses (fs to ps). In general, a passive synchronization technique, also known as optical synchronization, is used, which is obtained by deriving a seed and a pump from the same laser source (Fig. 1.4).

Regarding the optical synchronization two different front-ends can be considered:

- Ti:sapphire - frontend (broadband);
- Yb - frontend (narrowband).

The advantage of a Ti:Sapphire front-end is a broadband seed. An octave-spanning Ti:sapphire oscillator can deliver enough power to seed an OPCPA and its pump [81]. In addition, the use of a broadband Ti:sapphire oscillator with CEP stabilization [82] permits further straightforward amplification of CEP-controlled pulses [83, 84]. A Ti:Sapphire front-end OPCPA system with a passive synchronization was demonstrated in [85]. Since enough power was not available directly from a Ti:Sapphire oscillator at 1030 nm, a small part of the Ti:sapphire oscillator was coupled in a photonic crystal fiber to generate a soliton centered at a pump wavelength similar to [86]. This type of passive synchronization is called the soliton self-frequency shift (SSFS) synchronization. A detailed theoretical and

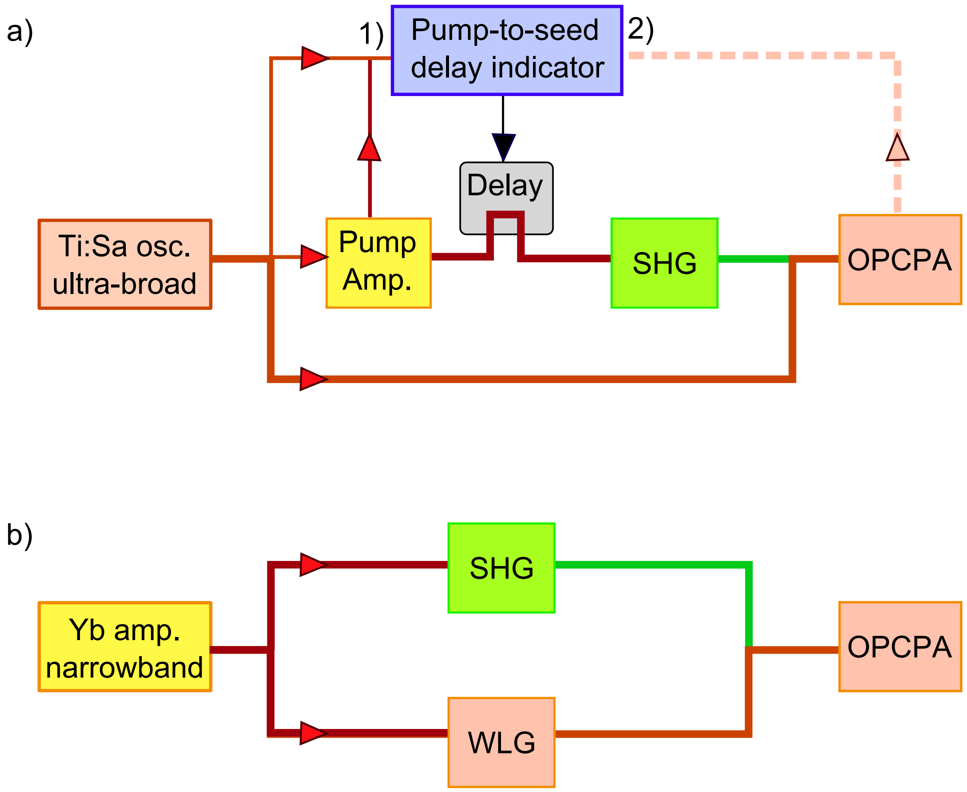

Figure 1.4: Concept of pump-seed synchronization: a) Passive synchronization with active stabilization commonly required for Ti:sapphire front-end OPCPA; Pump-to-seed delay indicator can be obtained by: 1) cross-correlation between pump and seed; 2) adjusting the spectral center of gravity of OPCPA output; b) Passive synchronization of Yb-frontend OPCPA. SHG – second harmonic generation; WLG – white light generation.

experimental investigation revealed an optimal type of a photonic crystal fiber [87]. The stability of the SSFS synchronization was significantly improved by using photonic crystal fibers with zero order dispersion wavelength (ZDW) at 850 nm instead of previously used fibers with ZDW at 750 nm. The system was used for the generation of isolated attosecond pulses showing its reliability and readiness for the applications. Isolated attosecond pulses at 600 kHz were demonstrated implementing SSFS synchronization [88].

The main disadvantage of a Ti:Sapphire front-end is its complexity. Some systems use additional active stabilization to compensate for temporal drifts in an OPCPA introduced by thermal changes in the path length of pump amplifiers [42, 89]. As a result, pump and seed overlap was stabilized and fluctuations of a few-cycle pulse duration was minimized. For the active stabilization, an indicator proportional to the pump-to-seed delay (Δt) is established (Fig. 1.4a). The indicator can be (1) a signal of a balanced optical cross-correlator between a pump and a seed or (2) the spectral center of gravity of the amplified OPCPA output. Thereafter, a pump delay is controlled according to the indicator's signal.

The advantage of a Yb front-end OPCPA is the stable optical synchronization. A broadband seed can be generated by white light generation (WLG) from a part of a pump laser, reducing the path length between the seed and the pump significantly, so that no additional stabilization is required (Fig. 1.4b). This makes an OPCPA system significantly simpler and easier to scale [89]. Yb-frontend OPCPA systems based on a seed generation by 300 fs to 1 ps pulses were demonstrated in [90, 89, 91, 92, 40]. However, shorter pulses have clear advantages for generating powerful and stable white-light supercontinuum [93].

Last but not least, Yb-frontend OPCPAs are more efficient due to diode-pumped Yb lasers. Ti:Sapphire lasers are commonly pump with SHG of Yb:YAG lasers.

1.2.2 Carrier-envelope phase stabilization

When laser pulses reached the few-cycle barrier, the importance of the carrier-envelope phase (CEP) and its influence on light-matter interactions was realized for the first time [15]. Few-cycle radiation allows atom-field interaction in the strong-field regime, because the rise-time of the electromagnetic field determines the maximum field strength atoms can be exposed to before the ionization [19]. Experimentally the CEP preservation in OPCPAs was demonstrated [83]. The CEP control allows one to vary the strength of the electric field in highly nonlinear experiments. The CEP control is also important in EUV and X-ray generation in a reproducible manner. A year later, a CEP-stable terawatt class OPCPA system was reported [94]. The first few-cycle Ti:Sapphire-frontend OPCPA system at MHz repetition rate was shown in 2012 [85]. With the same system, however at 0.6 MHz repetition rate, generation of isolated attosecond pulses were reported [88].

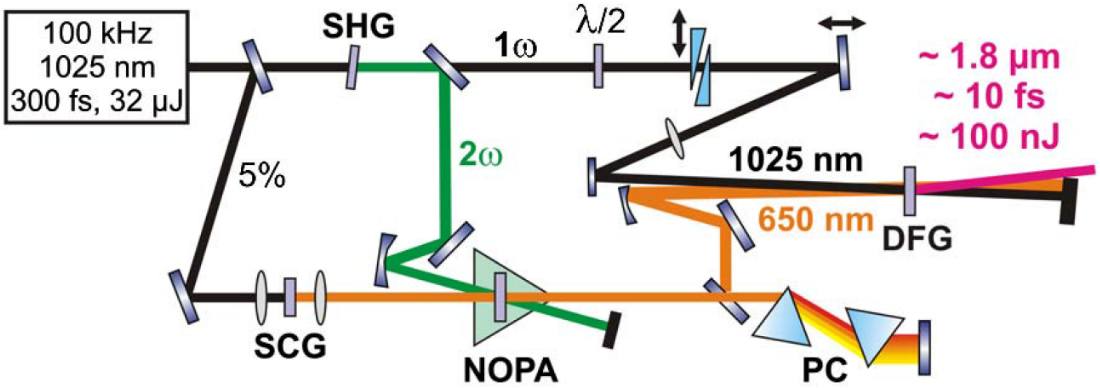

Figure 1.5: Setup of Yb-frontend few-cycle CEP-stable OPCPA. SCG – supercontinuum generation; NOPA – noncollinear optical parametric amplifier; PC – prism compressor; DFG – difference frequency generation. Courtesy of C. Homann [91].

Yb-frontend OPCPAs can also be CEP-stabilized. The first method is based on the CEP-stabilized Yb laser by the feed-forward method [95, 96, 70]. The second concept is based on the broadband DFG between the output of an OPCPA and the narrow-band pump laser [91]. The setup of an Yb-frontend few-cycle CEP-stable OPCPA is shown in Fig. 1.5 [91]. A commercial Yb:KYW laser was used as a frontend. A small part of the laser (5 %) was used for the WLG in an YAG crystal to obtain a seed for the OPCPA. The rest was frequency doubled to generate a pump. After optical parametric amplification in a BBO crystal, the OPCPA output and the pump were mixed by using a difference generation process. The IR output was measured to be CEP stable, as expected from [97, 98]. A pair of wedges in a pump beam path was used to control the CEP.

1.3 High power Yb pulse laser designs

Improvements in brightness and power of laser diodes paved the way to new solid-state kW-class femtosecond laser designs. The temperature management of a gain material is crucially important for all of these designs, such as:

- Fiber (Fig. 1.6a);
- Thin-disk (Fig. 1.6b);
- Innoslab (Fig. 1.6c).

The technology of **fiber amplifiers** was scaled-up due to the development of LMA fibers [100, 101, 102]. The high average power can be obtained due to the high surface-to-volume ratio of a fiber, which enables efficient air-cooling. For kW-class lasers, a water-cooling is required [38]. The advantage of the fiber amplifiers, besides temperature management, is high amplification gain. The gain of the preamplifiers can be as high as 60 dB, however amplified spontaneous emission should be kept under control [103]. In fiber amplifier systems consisting of a chain of fiber ampifiers, the gain of the main amplifier is still as high as >> 10 dB [38, 105]. By combining chirped-pulse amplification (CPA) and LMA PCF fibers, 640 fs pulses with 830 W average power at 76 MHz repetition rate have been demonstrated [38]. The disadvantage of the fiber technology is the fundamental limitation of the peak power by self-focusing to 6 MW (circular polarization) [104].

Thin-disks provide a low single-pass gain in the range of 10 %. Beside oscillators [106, 107, 108, 70], thin-disks are also used in regenerative amplifiers [81] and multipass amplifiers [109]. A typical setup of a **regenerative amplifier** is shown in Fig. 1.6b. The gain medium is commonly a Yb:YAG crystal, pumped from the back side by a diode laser. The gain medium is placed in an optical resonator realized by mirrors M_{1-4} and a thin-film polarizer (TFP_2). An optical switch is obtained with a Pockels cell (PC) and a polarizer. A pulse is coupled through an optical isolator consisting of a thin-film polarizer (TFP_1), Faraday-rotator (FR) and a half-wave plate (HWP). The optical isolator is used to couple-out pulses after a desired number of cavity round-trips. Also, the isolator protects an oscillator from any back reflections. Pulses in p polarization propagate through the thin-film polarizer (TFP_2), the Pockels cell (PC) and the quarter-wave plate (QWP).

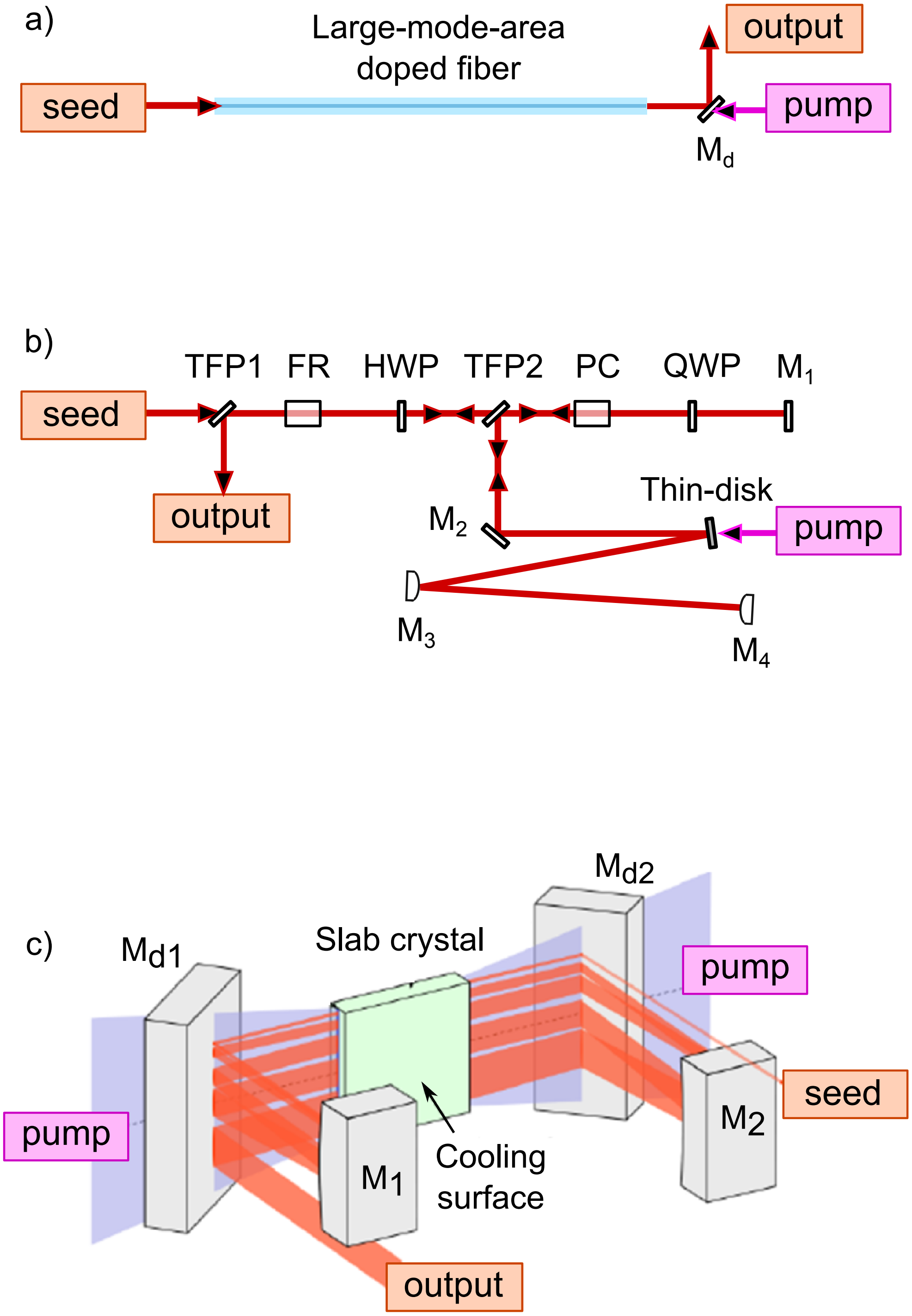

Figure 1.6: Different designs of high power Yb amplifiers: a) Fiber; b) Thin-disk regenerative; c) Innoslab. $M_{d,d1-2}$ – dichroic mirrors; TFP_{1-2} – thin-film polarizers; FR – Faraday rotator; HWP – half-wave plate; PC – Pockels cell; QWP – quarter-wave plate; M_{1-4} – cavity mirrors. Part c) is adopted from [99] with courtesy of P. Russbueldt.

The required voltage to turn the polarization by 45° in a crystal of the Pockels cell can be calculated by [110]:

$$V_{1/4} = \frac{\lambda d}{4n_0^2 r_{22} L}, \tag{1.17}$$

where λ is laser wavelength; d – crystal thickness for applied voltage; n_0 – linear refractive index; r_{22} – electro-optic coefficient, which is 2.2 pm/V for a BBO crystal; L – crystal length for optical pulses.

When the voltage is applied, pulses are circulating in the cavity, when the voltage is off - pulses are coupled-out. A BBO crystal is commonly used for a Pockels cell because of the negligible piezoelectric ringing and the high optical damage threshold. However, the disadvantage of a BBO material is relatively low electro-optic coefficient r_{22}. In addition, the quarter-wave voltage (Eq. 1.17) is unfavorably directly proportional to the thickness of the crystal and indirectly proportional to its length. Thus, one chooses an aperture as small as possible and a length as high as possible for the BBO crystal in order to keep voltage practically manageable. However, the exact opposite is preferable in order to keep the nonlinear effects under control: as short as possible crystals with as high as possible aperture. The Pockels cell is the main limiting factor for the scaling-up regenerative amplifiers in terms of the output power and the pulse energy, since a BBO crystal is a single bulk material in the cavity. Due to a BBO crystal as a Pockels cell, the average power is limited to approximately 100 W for these type of amplifiers [111].

Innoslab lasers are single-pass amplifiers. A scheme of an Innoslab amplifier is shown in Fig. 1.6c [99]. A slab crystal Yb:YAG with dimensions of 1 mm x 10 mm x 10 mm is pumped from both sides by a laser diode stack. The water-cooled crystal is braced in a metal mount with an indium foil in between for good thermal conduction. A homogeneous pump line in the middle of the crystal is crucially important for the quality of the output beam. The output beam is elliptical, because it expands mainly in one axis in the crystal. The beam does not exceed the dimensions of the pump line, because of the gain-guiding. The ellipticity can be corrected to a certain optimal value with an optimized cylindrical telescope. The exclusive feature of the Innoslab amplifier are different values of M^2 parameter in horizontal- and vertical-, respectively x- and y-axis. Since the beam in the x-axis is guided by the gain, its M^2 value is almost diffraction limited with a common value of $<$ 1.1. This value is almost output power independent. The beam expansion in the other axis is advantageous: it balances the increase of the power, avoids optical damage and keeps the B-integral small [112]. However, inhomogeneity of a crystal, which might be due to thermal load, influences a spatial wave-front of a beam. As a result, the M^2 value in y-axis increases with the output power. The optimized M^2 value at 600 W in y-axis is commonly between 1.3 and 1.4.

As a gain material Yb has a serious drawback for ultrashort applications: it is intrinsically narrowband in comparison to Ti:sapphire, with correspondingly long generating and/or amplifying pulses (commonly between 250 fs - 1 ps). However, Yb lasers are perfectly suitable for the OPCPA pumping, as described in section 1.2.

1.4 Extreme ultraviolet generation at megahertz repetition rate

The extreme ultraviolet (EUV, 10 - 121 nm) region receives attention both in microscopy and spectroscopy. It is still a rather unexplored range due to the lack of suitable direct laser sources. Frequency comb spectroscopy in EUV [30] profits from repetition rates at multi-megahertz, because the distance between the comb lines are proportional to the repetition rate. The repetition rate should be high enough, so that the lines of the comb can be well resolved [31]. EUV at multimegahertz repetition rate opens the door for the amazing applications, such as spectroscopy of hydrogenic systems [32], investigation on variations of fundamental constants [33], and time of flight photoelectron emission microscopy with attosecond pulses [34]. Investigations on DNA and other bio-molecules can be performed using table-top coherent X-ray sources in the water window (4.4 - 2.3 nm) with high contrast and spatial resolution [35]. For applications in microscopy high repetition rate of an EUV source not only reduces the exposure time, but also makes real-time microscopy with short wavelength radiation feasible [113].

The EUV spectral region is available by optical harmonic generation (OHG) and lamps. Low-order harmonic generation (LHG) is produced with an efficiency that rapidly decreases with the harmonic order. LHG can be explained by a perturbative solution of Maxwells equations [114]. EUV at MHz repetition rates can be generated in an enhancement cavity [1] or in a conventional single-pass geometry, as used originally at low repetition rates.

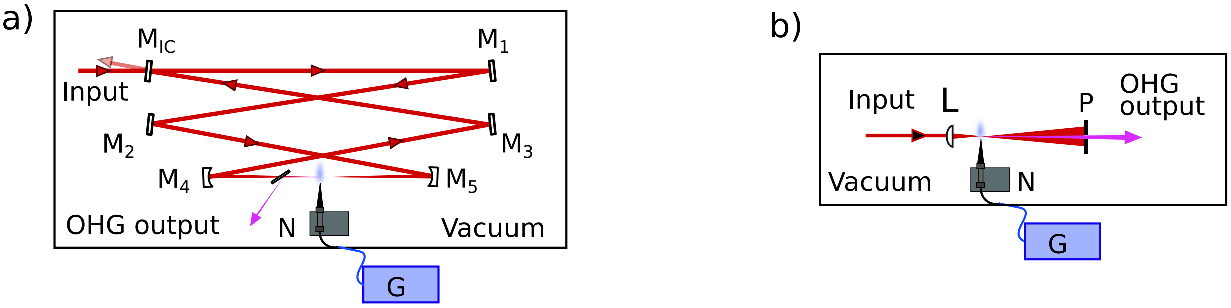

Figure 1.7: Concept of optical harmonic generation at MHz repetition rate: a) Cavity-assisted; b) Single-pass. M_{IC} – input coupler; M_{1-5} – cavity mirrors; G – gas supply; N – gas nozzle; L – lens; P – pinhole.

A concept of the enhancement cavity is presented in Fig. 1.7a. Ultrashort pulses can be coherently overlapped in an optical resonator. A gas target is placed, where the laser intensity is the highest in the resonator. The generated EUV radiation can be coupled-out by a fused silica plate placed at the Brewster-angle for the fundamental radiation, because the losses in the cavity should be negligible. A feedback system can be used to stabilize the cavity length, for example by phase lock loop (PLL) synchronization. Timing jitter of 20 fs was obtained using this type of synchronization [115]. However, this is a very complex system and its long-term stability is challenging.

The development of Yb laser systems makes LHG generation possible without field enhancements in so called single-pass geometry, because such laser systems can provide direct access to high field processes at multi-MHz repetition rates [116]. In this case, laser pulses are simply focused into a gas target (Fig. 1.7b). The output power of the fundamental can be reduced by placing a pinhole (P), since the divergence of harmonics is smaller than the divergence of the fundamental. The rest of the fundamental radiation on the optical axis can be separated from the harmonic radiation by diffraction gratings, dichroic mirrors or other EUV optics. The setup of single-pass LHG is significantly easier compared to cavity-assisted LHG. Moreover, quasi-phase-matching techniques [117, 118, 119] can be implemented to increase the efficiency of LHG, which is impossible in enhancement cavities.

Chapter 2

Nonlinear pulse compression

Many experiments in high field science benefit from sub-100 fs μJ-level pulses, stable on a time scale of hours. Some experiments require optically synchronized sub-100 fs to ps pulses. One example is time-resolved electron diffraction for the investigation of atomic motions during chemical and biological processes with sub-atomic spatial resolution [121, 122, 123]. For this experiment, electron pulse characterization is very important. It can be performed by streaking electron pulses in THz fields, generated from the same laser source [124]. For THz pulse generation, picosecond pulses emitted by Yb:YAG amplifiers are optimal [125, 126]. For generating fs electron pulses, pulse compression combined with the second or the third harmonic generation is required depending on the cathode material, after which, electron pulses can be compressed with a microwave cavity [127, 128].

Another example use high-energy Yb-frontend OPCPA. High repetition rates and pulse energies can be achieved by this technique, due to a low thermal load during the parametric process. As Yb amplifiers can deliver up to kW average powers [37, 38], they are useful for pumping high-power OPCPAs. An OPCPA system seeded by WLG from a 1 ps Yb:YAG laser was demonstrated in [90], alongside a detail discussion of why 1 ps pulses are unfavorable for WLG. In later work more complicated systems have been implemented in which one part of an Yb oscillator (pulse duration 400 fs) was used to generate a seed for an OPCPA and the other part was amplified in a chain of Yb amplifiers until sufficient energies were achieved for an OPCPA pumping [89, 92, 40]. Unfortunately, this more complex set-up is disadvantageous for pump-seed synchronization due to thermal path length drifts affecting temporal pump-seed overlap (for more information, see 1.2.1). An elegant design of a few-cycle OPCPA with a 300 fs 40 W Yb:YAG amplifier front-end was demonstrated at 100 kHz repetition rate [91]. However, when scaling an OPCPA from nJ to mJ, as required for many ultrafast applications (such as COLTRIMS and EUV), higher pump powers are needed. We note that, on further amplification, the pulse duration of any amplifier output increases because of the gain-narrowing effect [129]. However, sub-100 fs pulses have a clear advantage for generating a broader, more coherent and stable white-light supercontinuum [93]. We can conclude from this brief review on existing work, that long-term stable pulse compression of a part of an Yb:YAG amplifier output combined with WLG is very important for the scaling-up OPCPA systems.

The NPC experiments were performed with different Yb:YAG laser systems, whose parameters are listed in Table 2.1.

Table 2.1: List of Yb:YAG laser systems for nonlinear pulse compression experiments

Laser	Repetition rate	Pulse duration duration, ps	Pulse energy	Ref.
Regenerative thin-disk amplifier	3 kHz	1.6	25 mJ	[81]
Regenerative thin-disk amplifier	50 kHz	1.1	400 μJ	[111]
Thin-disk oscillator	11 MHz	1.0	4.5 μJ	[120]
Innoslab amplifier	20 MHz	0.7	30 μJ	[112]

Firstly, experiments at 50 kHz repetition rate with an LMA-35 fiber are described in this chapter. Secondly, results regarding the use of LMA-15, LMA-25 and LMA-35 fibers at 11 MHz repetition rate and thus significantly higher average power are presented. Finally, a description of measurements with an LMA-100 fiber will be given at both low and high average powers, corresponding to 3 kHz and 20 MHz pulse repetition rates.

2.1 Experiments at 50 kHz repetition rate

2.1.1 First stage

An experiment was driven by an Yb:YAG regenerative amplifier described in [111]. The amplification factor of the device was 40 dB, corresponding to input pulses of 100s pJ and output of 10s nJ. The repetition rate was adjusted from 50 kHz to 300 kHz, resulting into measured pulse durations of 1.1 ps and 0.8 ps respectively. As this was a chirped pulse amplifier, the introduced chirp was compensated by a linear dispersion compressor optimized at 300 kHz repetition rate. The dependence of pulse duration on the repetition rate was not investigated in detail, but we presume that, it can be explained by the thermal expansion of the air-cooled fused silica transmission gratings in the compressor when operating at high average power. The average powers were 20 W and 100 W at 50 kHz and 300 kHz, respectively. For the NPC experiments, a repetition rate of 50 kHz was selected due to its applicability to electric diffraction experiments, in which a balance is needed between the speed of data acquisition and thermal effects of the thin films being studied.

The experimental setup is shown in Fig. 2.1a. A small part of the output of the amplifier (a maximum of 2 % due to the critical self-focusing limit of a fiber) was focused into a LMA-35 fiber (NKT Photonics). The remaining power was used for experiments described in [111]. In order to avoid stress-induced birefringence due to mounting, the fiber was laid (without a fixative) in a V-groove aluminium mount, which was then mounted on a XYZ translation stage (Thorlabs NanoMax) (Fig. 2.1b). Commercially available solid core passive LMA PCFs are limited to a mode field diameter of 26 μm [130], thus defining our choice of fiber and the range of pulse energies. A cross-section of the fiber is shown in Fig. 2.1c.

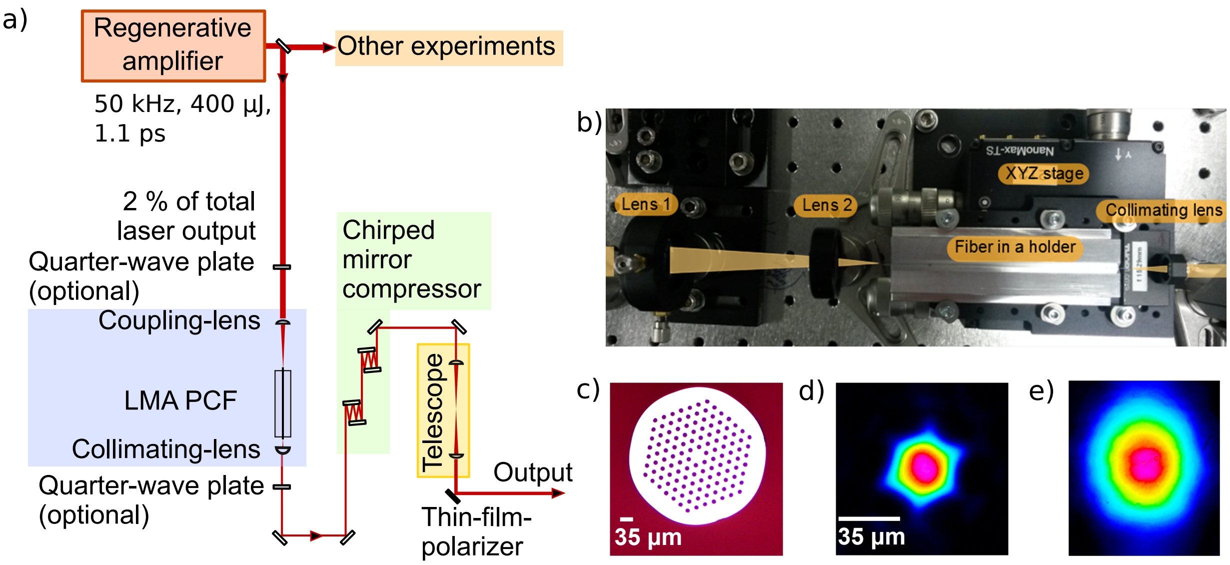

Figure 2.1: a) Nonlinear pulse compression setup at 50 kHz repetition rate. Comprising of a Yb:YAG thin-disk regenerative amplifier, a synthesized coupling-lens (focal length 75 mm, beam diameter 4 mm at $1/e^2$ level), a LMA-35 fiber (NKT Photonics, mode field diameter 26 μm), a collimating lens (focal length 18 mm), and a chirped mirror compressor (average value of GDD -540 fs^2/reflection in the spectral range from 980 nm to 1060 nm, 22 reflections). b) Photo of fiber holder, coupling and collimating lenses. c) Fiber cross-section. d) Near-field image of the fiber end-facet. e) Mode in far-field.

For fiber mode-matching, the complex q parameter of the laser beam was evaluated by measuring the beam diameter (at $1/e^2$ level) with a beam profiling camera within a distance of 2 m. This allowed both the beam diameter at the fiber input-facet and the beam divergence angle to be evaluated. The required focal length and numerical aperture (NA) of the coupling lens were calculated using an ABCD matrix to match the fiber mode, so that the MFD equaled the focus diameter and the NA of the fiber equaled the NA of the lens. The laser beam (4 mm in diameter at $1/e^2$ level) was coupled in by a 75 mm AR-coated N-BK7 lens. The end-facet of the fiber was imaged by an aspheric lens (focal length $f \approx 18.4$ mm) onto a beam profiling camera to optimize the coupling. The near-field image of coupled light in the fiber core is shown in Fig. 2.1d. To optimize the throughput we coupled the light using two spherical lenses separated by a variable distance, giving us the advantage (over a single lens) of an adjustable effective focal length, modified by changing the separation of the lenses. We note that the distance between the second lens and the fiber should be also changed when changing the lens separation. The estimated optimal coupling efficiency into the fiber core was 77 %. For these measurements, a pinhole was placed at the near-field image of the fiber end-facet, this meant that cladding modes were blocked by the pinhole and only the power coupled into the fiber core was measured. The result agreed well with an additional measurement in the far-field without a pinhole, when the cladding-modes were blocked by an iris diaphragm. We also wished to couple circularly polarized

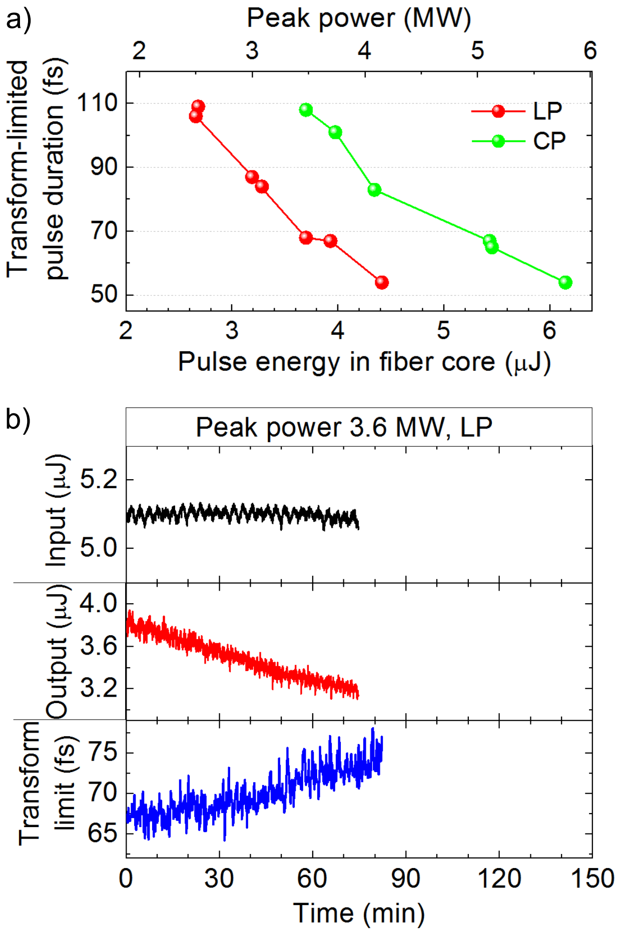

Figure 2.2: a) Transform-limited pulse duration of spectra with linear (LP) and circular (CP) polarization; b) Long-term stability of input, output, and transform-limited pulse duration of spectra. Peak power 3.6 MW; Fiber length 35 mm; LP.

light, because it is well known that the critical self-focusing limit is higher for circularly than linearly polarized light [131, 104]. In order to do this, an achromatic quarter-wave plate was placed before the coupling lens as an optional element in the setup for transforming the laser polarization from linear to circular. The polarization was transformed back by another achromatic quarter-wave plate after the collimating lens. Pulses were compressed with a chirped mirror compressor built for a linear polarization with the average GDD value of -540 fs^2/reflection in the spectral range from 980 nm to 1060 nm.

The aim of the experiment was to generate pulses that are the shortest possible, with the highest pulse energy possible, whilst also maintaining stable operation for hours, as is important for applications described above. We used a value of a transform-limited pulse duration to characterize broadened spectra. This value plotted versus a pulse energy and a peak power in the fiber core is shown in Fig. 2.2a for linear and circular polarization.

According to literature, the critical self-focusing peak power is approximately 4 MW

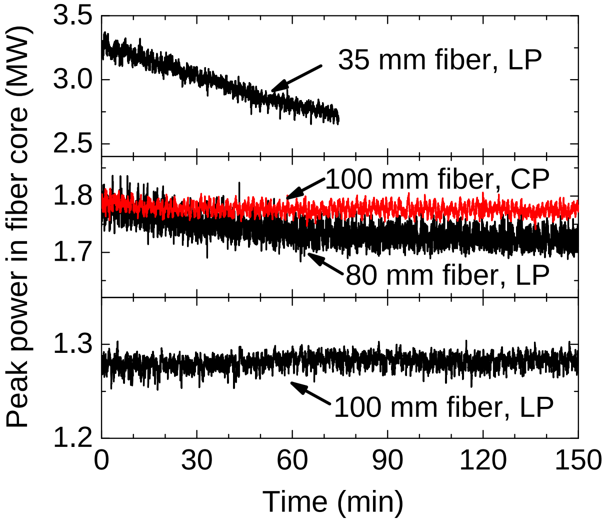

Figure 2.3: Long-term stability with different fiber lengths: 50 mm; 80 mm linear polarization (LP); 100 mm, LP and circular polarization (CP). Spectral broadening supports 66 fs.

for linear and 6 MW for circular polarization, with the latter value higher due to a lower effective electrical field strength [104]. Experimentally, with an LMA-35 fiber we have reached the critical self-focusing peak power both with linear and circular polarization (fiber was 35 mm long). The MDF of an LMA-35 fiber is 26 μm. To our knowledge, the critical self-focusing peak power was reached before in fibers of a significantly larger MFD: 60 μm [61, 62] and 75 μm [132]. Published numerical simulations have estimated that the peak power, close to the critical self-focusing limit, can be achieved only in LMA fibers with an MFD of more than 40 μm [104], whereas in fibers of smaller diameter, damage occurs due to other fundamental mechanisms occuring at lower values. We pressume, that we have reached the critical self-focusing peak power in an LMA-35 fiber due to low average power. At high average powers, this type of fiber became damaged at lower peak powers (see summary in Table 2.4).

We have not observed any abrupt fiber damage at critical self-focusing limit, but rather degradation of the output power and generation of additional spectral components with a visual clue of “red light” in the output of the fiber, as will be discussed in detail later. At a slightly lower level (3.6 MW) than the critical-self focusing peak power, the output pulse energy decayed with a significant rate of 8 nJ per minute (Fig. 2.2b). As a result, after 75 minutes the output dropped by 15 % from 3.8 μJ to 3.2 μJ. Unsurprisingly, the spectra narrowed with time, which can be seen from the increased value of the transform-limited pulse duration. For the long-term stability characterization, the input power reference, the output power and the spectra were simultaneously measured. Some fluctuations within a 2-minute period are visible as the result of a laser cooling system [111]. Such a quick degradation of the output was not induced by mechanical instabilities of the setup, because the coupling into the fiber was stable within days as monitored by the near-field imaging due to an integrated active beam stabilization system (Aligna, TEM Messtechnik). The measured beam pointing of the collimated input beam was < 0.04 % of root-mean-square (rms) versus the beam diameter at the position of the lens. The measurement was performed with a CCD camera using DataRay software. Any thermal drifts can be excluded in this setup, because the input average power of the laser was low, maximally only 250 mW.

Long-term stability measurements were conducted with lower pulse energies and longer fiber pieces for the same spectral bandwidth to find out the optimal conditions (Fig. 2.3). Reduction of the pulse energy for better stability results in reduced spectral bandwidth. Thus, we reduced the pulse energy and increased the fiber length correspondingly to maintain the bandwidth. The output stability was recorded both with 50 mm and 80 mm long fibers. The decay was almost negligible with a 80 mm long fiber: the output pulse energy reduced only by 2 % in the first 30 minutes and stayed almost steady thereafter, reducing however additionally by 5 % in the following 16 hours. Working with a 100 mm long fiber, no decay was observed both with linear and circular polarization. The output pulse energy with a 100 mm fiber and circular polarization was as high as with a 80 mm fiber and linear polarization.

The pulse-to-pulse stability within 10 ms was 1.1 % rms for input pulses and 1.2 % for the output with a 100 mm long fiber both with linear and circular polarizations. The pulse-to-pulse stability was additionally measured with a photo-diode and an oscilloscope.

We calculated the necessary GDD for the pulse compression by summing up the GDD by the chromatic dispersion (Eq. 1.16) and the SPM GDD (Eq. 1.15). The validity of the Eq. 1.15 was experimentally verified.

Compressed pulses were characterized by a second harmonic generation frequency resolved optical gating (SHG FROG) technique, which is a spectrally resolved autocorrelation [133]. Pulses were split into two variably delayed replicas and combined again by non-polarizing beamsplitter cubes (N-BK7 glass, 50 mm total thickness). The two pulse replicas were crossed in a BBO crystal. The nonlinear mixing was spectrally resolved as a function of the time delay between two beams. The GDD by chromatic dispersion has two contributions: 1900 fs^2 in a 100 mm fiber and 1620 fs^2 in two non-polarizing beamsplitter cubes (N-BK7 glass, 50 mm total thickness) mounted in the SHG FROG device. The average intensity inside the fiber core for 1.5 μJ pulses was $2.4 \times 10^{15} W/m^2$. The nonlinear refractive index of a silica-core fiber without dopants inside the core is $2.36 \cdot 10^{-20}$ m^2/W [134]. The SPM GDD was estimated as 6278 fs^2. The total calculated dispersion value reached 9798 fs^2. The shortest pulses were measured with 22 bounces on the chirped mirrors with -540 fs^2 GDD per reflection in the spectral range from 980 nm to 1060 nm. The experimentally found value of the introduced GDD for realizing the shortest pulses was 11880 fs^2, which deviates by 18 % from the calculated value in equations 1.15 and 1.16. This simple estimation can be used for evaluating the required compressor GDD, making the first compressor design steps significantly easier. For 1 ps input pulses, the SPM GDD made 64% of its total GDD.

In the next step, we experimentally found that the amount of the necessary GDD for

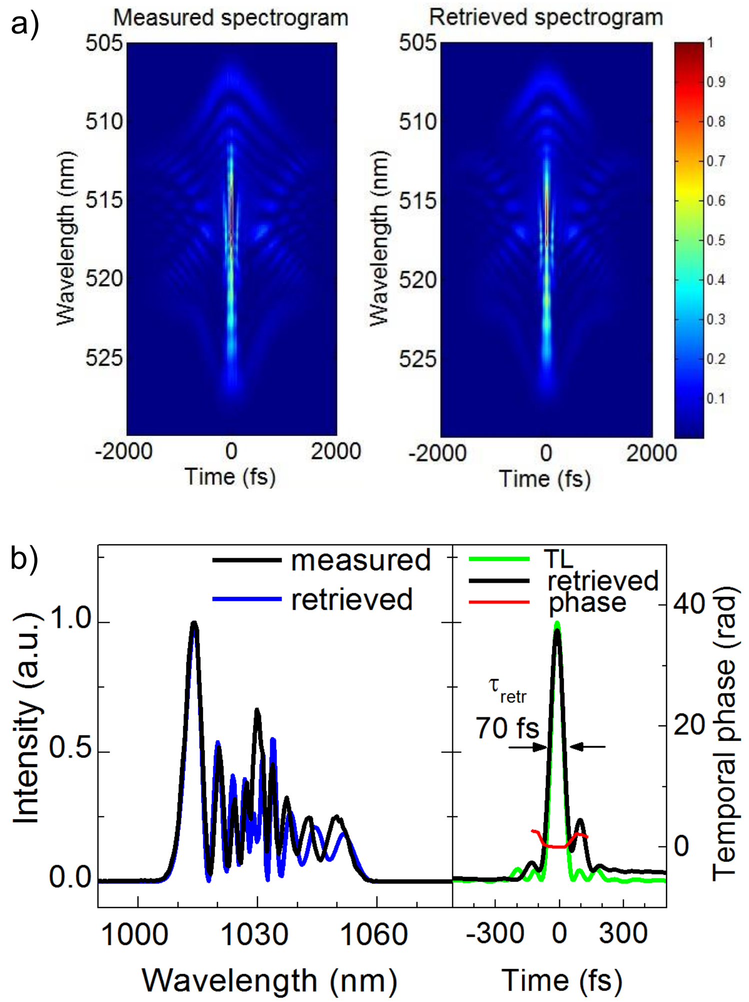

Figure 2.4: SHG FROG traces of the compressed pulses: a) Measured and retrieved spectrograms, grid size 256x256; b) Measured and retrieved spectra, transform limit (TL), retrieved temporal intensity and temporal phase of the shortest pulses.

linear and circular polarization was the same for a similar spectral broadening. Fig. 2.4a shows spectrograms of the measured and the retrieved SHG FROG of the shortest pulse. The reconstructed pulse has a duration of 70 fs (FWHM), whereas the transform-limited pulse duration calculated from the measured spectrum is equal to 66 fs (Fig. 2.4b). One can see, that the distances between the peaks in the red side are larger than in the blue side of the measured spectrum. The spectral broadening is larger on the blue side than on the red side due to self-steepening. Self-steepening results from the intensity dependence on the group velocity. As a result, the peak of a pulse moves slower than the wing [59]. Such a situation is possible for intense input pulses, since we are working with pulse energies close to the self-focusing limit. The main peak contains about 57 % of the pulse energy. The total pulse energy was 1.4 μJ after the compressor and some optics (5 silver mirrors, 2 AR-coated lenses of a telescope, and a thin-film-polarizer) in a linear s-polarization. The

Table 2.2: Summary of one-stage NPC at 50 kHz

Input duration	1.1 ps
Output duration (fs)	70
Compression factor	15.7
Input peak power (MW)	1.6
Fiber damage	Output degradation, if peak power > 2 MW, pulse energy in the fiber core: > 1.5 μJ linear pol. > 2.1 μJ circular pol.
Compressed peak power (MW)	20

total compressor efficiency was 67 %, since the reflection per bounce slightly exceeded 98 %.

The summary of the results of the first stage is given in Table 2.2. The peak power of the compressed pulses was higher than that of the initial pulses. This suggested that it should be possible to obtain additional compression by passing the pulses through a second compressor similar to [49].

2.1.2 Second stage

The two-stage NPC was first demonstrated in 1983. The final pulse duration of 90 fs was achieved with 12 nJ 6 ps input pulses with a total compression factor of 65 by using a 3 m long single mode polarization preserving optical fiber for the spectral broadening in the first stage and a 55 cm long fiber in the second stage [49]. For Yb amplifiers, the two-stage NPC was also reported. Two stages of hollow-core fibers were implemented to achieve 35 fs from 480 fs input pulses at a repetition rate of 50 kHz [68]. However, few-cycle (sub-10 fs) pulses are important for many applications in ultrafast science. An octave-approaching spectral broadening in a single-stage NPC with further compression down to sub-10-fs pulses is a well known technique used in many Ti:sapphire laser-based experiments. However, those input pulses are significantly shorter compared to 1 ps (see Table 1.1). In this subsection, we investigate the compression to sub-10-fs pulses in the two-stage NPC with 1 ps input pulses.

Spectra generated in the second piece of the LMA-35 fiber are shown in Fig. 2.5. The measurements were performed with different fiber lengths: 25 mm, 40 mm and 100 mm. Input pulses were transform-limited with a measured pulse duration of 70 fs, as described in subsection 2.1.1. The input polarization was linear. With a 25 mm long fiber, the shortest transform limit of a broadened spectrum was 16 fs with the corresponding pulse energy of 0.5 μJ in the fiber core. The further increase in the pulse energy resulted in a narrower spectra, as indicated by the increased transform-limited pulse duration in Fig. 2.5. The fiber became damaged at 0.7 μJ. The value of the critical self-focusing peak power corresponds to 0.3 μJ pulse energy. Practically, this value was higher because of

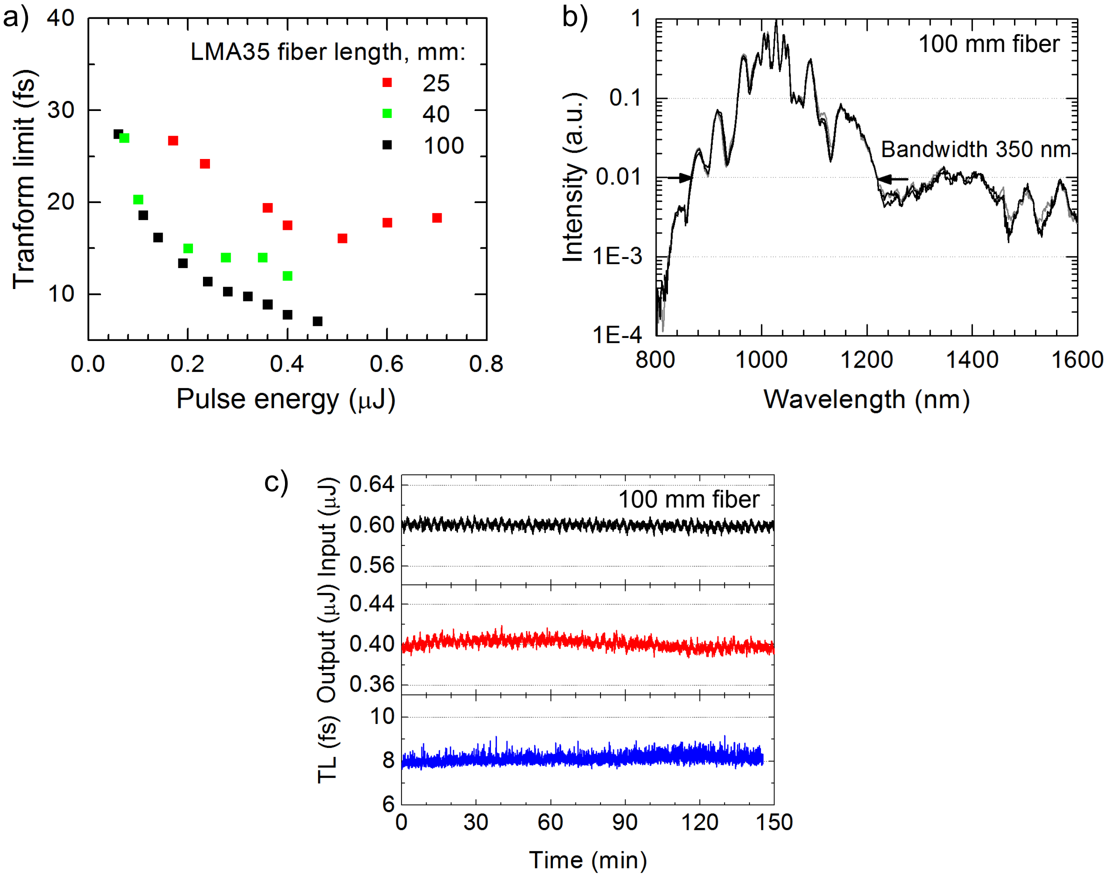

Figure 2.5: Two-stage NPC in LMA PCF: a) Transform-limited pulse duration versus pulse energy in the fiber core for different fiber lengths; b) Spectra after the second stage with a 100 mm long fiber and linear polarization at 0.4 μJ, 70 fs pulse energy in the fiber core (3 consequent measurements with a period of 1 s); c) Long-term stability of input, output and transform-limited pulse duration of the spectra. Fiber length 100 mm, linear polarization.

the chromatic dispersion in the fiber. With a 40 mm long fiber, the shortest transform limit was 12 fs with 0.4 μJ pulse energy in the fiber core. With a 100 mm long fiber, a spectral bandwidth supporting sub-10 fs pulses was reached. It is worth mentioning that the 100 mm long fiber had end-caps. As a result, the intensity was lower at the input facet of the fiber and it could withstand higher input pulse energies resulting in a broader spectrum. The spectral bandwidth extended over more than one octave (Fig. 2.5b). The spectra above 1600 nm was not measured, because of the limits of the spectrum analyser. The bandwidth of the output spectra was about 350 nm at 1 % level. Transform-limited pulse duration of the spectra was 8 fs. In the picture, three consequent spectra with a period of 1 s are shown, indicating a good short-term stability. Additional measurements of the pulse-to-pulse stability were performed with an oscilloscope and a photo-diode. The output pulse-to-pulse stability, within 10 ms, was 1.9 % rms, whereas the input pulse-

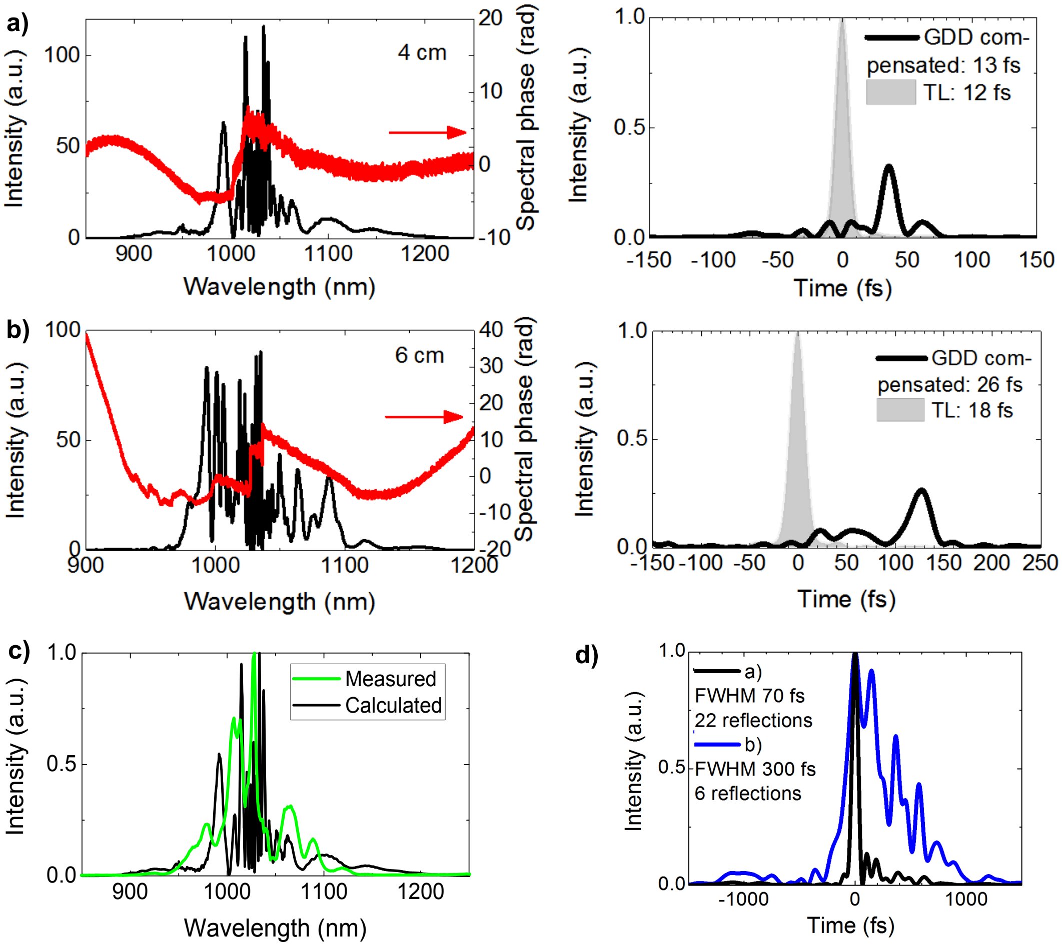

Figure 2.6: a) Calculated spectrum and spectral phase after the second NPC stage with transform-limited input pulses (left hand side); Temporal intensity of transform-limited and compressed by GDD compensation pulses (right hand side); b) Same as (a), but with chirped input pulses; c) Comparison of the measured and the calculated spectra with a 40 mm long fiber and transform-limited 0.4 μJ input pulses; d) Input temporal profiles used for the simulations: Black curve corresponds to the optimal 22 reflections on the chirped mirrors (used in simulations (a), blue curve – to 6 reflections (used in simulations (b).

to-pulse stability was 1.2 % rms. The long-term stability of the corresponding spectra is shown in Fig. 2.5c. The output and the transform limit of the measured spectra indicates an excellent long-term stability for hours (Fig. 2.5c).

The results of the theoretical simulations of the second stage with transform-limited and chirped input pulses are shown in Fig. 2.6. The numerical simulations were performed by solving a nonlinear Schrödinger equation by the split-step Fourier method, as described in [59]. The calculated spectrum coincided well with the measured spectrum and its transform-limit of 12 fs with the 40 mm fiber and a pulse duration of 0.4 μJ (Fig. 2.6c). Fine oscillations were not resolved in the measurement, because the spectral resolution of the spectrometer was 1.7 nm, while the spectral resolution of the simulations was 0.3 nm. The calculations indicate, that the spectral phase is very complex and pulses are hardly compressible (Fig. 2.6a). On the right side, a transform-limited pulse is depicted if the chirp of the pulse can be fully compensated. Similarly, a partially compressed pulse is shown only if the quadratic term of the spectral phase is compensated with the compressor GDD. As a result, the pulse energy in a main peak was significantly lower (< 50 %) compared to its transform limit.

The results of the theoretical simulations with chirped input pulses are shown in Fig. 2.6b. The advantage of chirped-pulse approach is the higher pulse energy in the fiber core compared to transform-limited input pulses. This approach is widely used for OPCPA. The input pulses after the first stage was chirped up to 300 fs. The obtained spectra in a 6 cm long fiber with 1 μJ pulses supported 18 fs. Pulses can be compressed only to 26 fs, only if the quadratic term of the spectral phase is compensated with the compressor GDD. The pulse energy in a main peak was low.

In Fig. 2.6d the temporal pulse intensity of the compressed and partially compressed pulses are shown, corresponding to 22 and 6 reflections on the chirped mirrors, respectively. For a non-Gaussian pulse, the instantaneous frequency peaks multiple times (see Fig. 1.2), resulting in a complex spectral phase, which is hard to compensate. The situation is similar both with the compressed and partially compressed input pulses after the first NPC stage (Fig. 2.6). An alternative and promising approach for achieving an octave-spanning spectrum and few-cycle pulses with 1 ps input pulses is WLG in crystals with compressed pulses out of the first NPC stage.

2.2 Experiments at 11 MHz repetition rate

2.2.1 First stage

The experimental setup is shown in Fig. 2.7a. The experiments were performed with an Yb:YAG mode-locked oscillator emitting 1 ps pulses with an average power of 52 W at a repetition rate of 11 MHz [120].

An optical isolator (I), designed for the maximal average power of 100 W (JENOPTIK FS-1-P100-1030), was used to protect the oscillator from back-reflections. The mode-locking of the oscillator was totally disturbed without the isolator due to the Fresnel

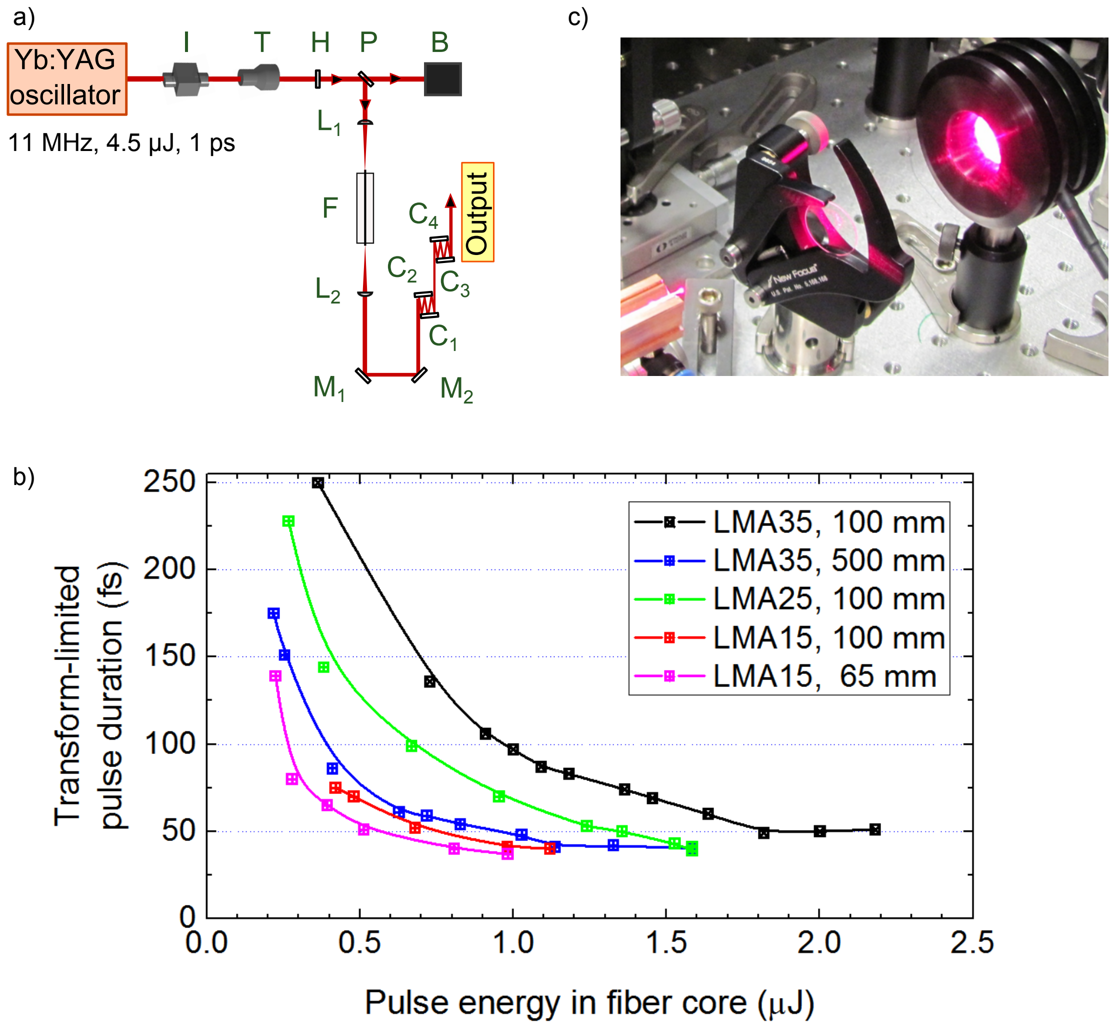

Figure 2.7: a) Nonlinear pulse compression setup at 11 MHz repetition rate. I – isolator; T – variable magnification telescope; H – half-wave plate; P – thin film polarizer; B – beam block; L_{1-2} – lenses; F – fiber LMA-25 and LMA-35 (NKT Photonics); M_{1-2} – silver mirrors; C_{1-4} – chirped mirrors, the same as in 50 kHz experiment, see Fig 2.1a; b) Transform-limited pulse duration versus pulse energy in the fiber core for different fibers and fiber lengths; c) "Red-light" observation in a 100 mm LMA-25 fiber at 1.58 μJ pulse energy in the fiber core.

reflections on the fiber end-facet. A telescope (T) with a variable magnification was used to optimize the coupling. For the attenuation of the input, a half-wave plate (H) and a thin film polarizer (P) were used. The rest of the beam was blocked in a water-cooled beam block (B). The fiber was freely lying in a water-cooled V-groove, which was fixed on a XYZ translation stage (Thorlabs NanoMax). Pulses were compressed with a chirped mirror compressor with an average GDD value of -540 fs^2/reflection in the spectral range from 980 nm to 1060 nm. The total compressor dispersion was between 6480 fs^2 and 12960 fs^2 (12 to 24 reflections, respectively) depending on the intensity in the fiber core.

Table 2.3: Damage threshold of different LMA PCF fibers at 11 MHz repetition rate

Fiber	Transform-limited pulse duration, fs	Damage peak irradiance, 10^{11} W/cm^2	Damage pulse energy, μJ
LMA-15	37	9.2	1.2
LMA-25	41	4.3	1.6
LMA-35	51	3.9	2.2

We studied spectral broadening in fibers with different mode field diameters of 13 μm (LMA-15 [135]), 21 μm (LMA-25 [136]) and 26 μm (LMA-35 [130]) (Fig 2.7b). The broadest spectrum supporting 37 fs was achieved with an LMA-15 fiber at 1 μJ pulse energy in the fiber core with a 65 mm long piece. A smaller core fiber, LMA-15, tolerated higher peak irradiance than LMA-25 and LMA-35 (Table 2.3). This relation can not be explained by [104] and needs to be further investigated. However, the smaller core fibers exhibited only slightly broader spectra, because SPM spectrum saturates (quicker for an LMA-15 than for an LMA-25 fiber). The broadest spectra with a 100 mm LMA-25 fiber supported 41 fs pulse similar as with a 100 mm long LMA-15 fiber. The broadest spectra with a 100 mm LMA-35 fiber supported 51 fs pulses. However, with a 500 mm LMA-35 fiber a similar spectral broadening as with a LMA-15 fiber was obtained. However, the spectra quickly saturated at a spectral broadening supporting 40 fs pulses. The LMA-15 fiber got damaged at 1.2 μJ pulse energy in the fiber core, whereas the LMA-25 and the LMA-35 were damaged at pulse energies of 1.6 μJ and 2.2 μJ respectively. We conclude that, the broadening factor can not practically exceed 25 in a single NPC stage with 1 ps input pulses, which means that the shortest pulses obtained after ideal compression, can be 40 fs long.

The dependence of the transform-limited pulse duration versus the pulse energy was similar at 11 MHz and 50 kHz repetition rates for the same fiber and the same fiber length. This is expectable, since the nonlinear effects depend on the laser intensity, not on the average power. However, the main difference observed comparing the NPC at kHz and MHz repetition rates was the damage threshold. The damage was abrupt at 11 MHz repetition rate, when a certain energy was coupled into the fiber. There were three differences at kHz compared to MHz repetition rate: Firstly, the fiber did not get damaged when the same pulse energies were achieved (see 2.6). Secondly, the increase in

Table 2.4: Damage threshold of LMA-35 fiber at different repetition rates

Rep. rate	Pulse duration, ps	Damage peak power, MW	Reference
50 kHz	1.1	4 MW; output degradation, if peak power > 2 MW	
11 MHz	1.0	2.0	
20 MHz	0.6	1.7	[116]
38 MHz	0.3	2.5	[70]
50 MHz	0.6	0.8 (SHG)	Chapter 4

the transmission losses through the scattering into the higher order modes was observed prior to the damage. That is why, the fiber did not get abruptly damaged at all, because of this self-regulation of the intensity in the fiber core. Thirdly, the output power degradation was measured significantly prior to the damage threshold. Unfortunately, the long-term stability was not determined at 11 MHz repetition rate, because of the thermal-drifts at high average power and unstabilized beam pointing of the laser output. The damage threshold of the LMA-35 fiber at different repetition rates are summarized in Table 2.4. The damage of the LMA-35 fiber was reported in the literature working with the Yb:YAG Innoslab amplifier at 20 MHz ([116]) and the Yb:YAG oscillator at 38 MHz repetition rate ([70]). The fiber length was comparable: 100 mm at repetition rates of 50 kHz and 11 MHz and 80 mm at repetition rates of 20 MHz and 38 MHz. The input pulse duration was however different: 680 fs and 250 fs respectively. The damage threshold was about 2 MW peak power at MHz repetition rates, whereas at kHz repetition rates, higher peak powers reaching 4 MW were achieved.

2.2.2 Second stage

The spectra supporting sub-10 fs can be obtained in two fiber NPC stages, however it can not be compressed to the transform-limit, because of a complex spectral phase, as discussed in 2.1.2. If experiments require only a broadband spectrum, this can be easily obtained from two stages in a single fiber.

A setup with two NPC stages in a single fiber is shown in Fig. 2.8a. The setup is similar to the setup shown in Fig. 2.7a, however a quarter-wave plate (Q) is placed before the coupling lens (L_1). The polarization was circular at the input of the fiber. The GDD of the mirrors was almost the same for s- and p-polarizations. After the mirror compressor, a high-reflective mirror at 0° angle of incidence was placed sending the beam back into the fiber. After the second path in the fiber, the polarization state was changed to p by a quarter-wave plate and separated from the input by a thin-film polarizer. The output spectrum is shown in Fig. 2.8b. Its transform-limited pulse duration was 7 fs. The spectrum was obtained using an 85 mm piece of the LMA-25 fiber. The total compressor GDD was 6480 fs^2 realized with 12 reflections on chirped mirrors. The output was 4 W (0.4 μJ). The total efficiency was 22 %, whereas the efficiency of the first stage was 67 %

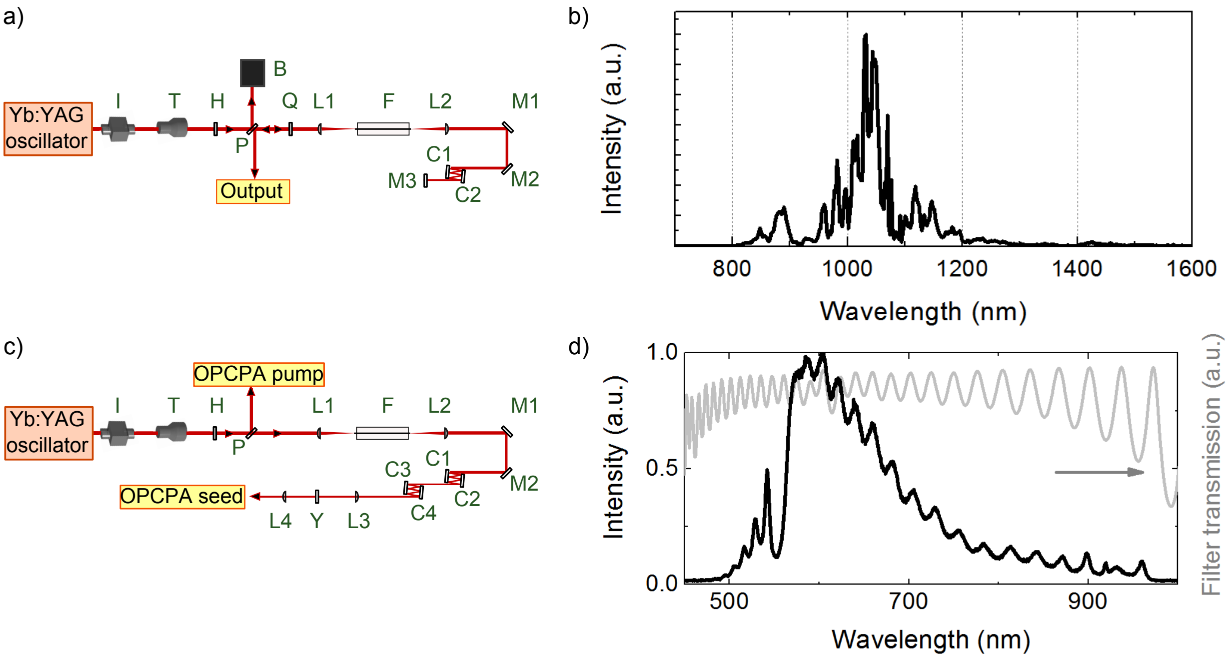

Figure 2.8: a) Two nonlinear pulse compression stages. Additionally to Fig. 2.7a: Q – quarter-wave plate; F – fiber LMA-25, length 85 mm; total compressor dispersion 6480 fs^2, 12 reflections on chirped mirrors; b) Spectrum after the second stage, transform-limit: 7 fs, pulse energy: 0.4 μJ; c) Setup of nonlinear pulse compression combined with WLG in bulk. L_{3-4} – achromatic lenses; Y – 4 mm thick YAG crystal; d) Spectrum after the crystal.

and of the second – 33 %. Both lenses used in the setup were achromatic.

The setup with the single NPC stage and WLG in a crystal is shown in Fig. 2.8c. A thin-film polarizer (P) was used in a transmission instead of the reflection one in Fig. 2.7a, because maximally 13 % of the laser output was coupled into the fiber to leave enough power for the OPCPA pump. That is why, the LMA-15 fiber with a length of 65 mm was used for the NPC stage. The output of the fiber was 4.8 W. The transform-limit of the spectrum was 56 fs. The pulses were compressed down to 70 fs. The supercontinuum measurements were performed by focusing the beam of 4 W average power into a 4 mm YAG crystal. The measured spectrum is shown in Fig. 2.8d. The output power after the filter separating the continuum from the fundamental was 50 mW (the pulse energy – 4.5 nJ). The transmission of the filter is depicted by a grey curve in Fig. 2.8d. The results of an extended study of the supercontinuum generation in different crystals, also the application of the similar broadband seed to seed an OPCPA is given in [137].

2.3 Experiments at 3 kHz repetition rate

The experiments at 3 kHz repetition rate were performed with LMA-100 fiber. The cross-section of the fiber is shown in Fig. 2.9a in comparison with the cross-section of the

LMA-35 fiber (b). Both figures are in scale with each other. The flat-to-flat diameter of the core of the LMA-100 fiber is about 100 μm, whereas of the LMA-35 – 35 μm. The outer diameter of the LMA-35 fiber is 335 μm [130] partly visible in the picture (Fig. 2.9a). The outer diameter of the LMA-100 fiber is 2 mm. It is a rod-type fiber [100]. The larger outer diameter improves the heat dissipation capabilities of the fiber [138] and reduces the propagation losses of weakly guided mode, because the fiber cannot be bent. It is visible from the picture, that the size of the holes (black round areas) and the distance between them are different for the LMA-100 and the LMA-35 fibers. This is expectable, because the hole diameter-to-pitch ratio is an important parameter for realizing large single-transverse mode waveguides and should be optimized for different core dimensions [139, 140].

We have measured, that the mode field diameter of the fiber is 85 μm. For this measurement we coupled the beam with different lenses into the fiber until the coupling was optimized. The focus size was measured with a CCD camera (DataRay WinCamD-UCD15). The intensity in the LMA-100 fiber is > 10 times lower than the intensity in the LMA-35 fiber at the same level of the coupled energy. The passive LMA-100 fiber was a prototype of the Yb-doped LMA-100 active fiber from NKT Photonics. Only Yb-doped LMA-100 fibers are commercially available for high power Yb-amplifier applications. In addition, commercial Yb-doped LMA-100 fibers have end-caps, which is a big advantage, since the cleaving of these rod-type fibers is complicated and is commonly irreproducible. A high power Yb fiber amplifier and NPC in the same fiber was published using the Yb-doped LMA-100 [132]. The pulse duration of 65 fs and the final pulse energy of 3.2 μJ were demonstrated.

The setup of the experiment is shown in Fig 2.9c. An Yb:YAG thin-disk regenerative amplifier emitting 25 mJ energy pulses at 3 kHz repetition rate with a pulse duration of 1.6 ps [81] was used as the input. We used 1 % of the mJ-level amplifier's output, the rest was used for other experiments [141, 42].

We performed the measurements with two different fiber lengths: 75 mm and 150 mm, and linear polarization of the laser beam. The maximal coupled pulse energy with linear polarization was kept at 7 μJ. The spectra at this level are shown in Fig. 2.9e and 2.9f. The transform-limited pulse duration was 85 fs and 60 fs respectively. Saturation of the spectral broadening was already achieved with the 150 mm fiber. The transform-limited pulse duration was 60 fs both with 6 μJ and 7 μJ coupled pulse energy. Also, the transform-limited pulse duration distinguished less than two times, even if the fiber length was two times different. This indicates that the shortest transform-limited pulse duration is 60 fs, which can be obtained with LMA-100 and 1.6 ps input pulses. The peak power was already 4 MW at this pulse energy. The peak power as high as 4 MW and transform-limited pulse duration of 60 fs were also achieved with 1 ps input pulses in [132]. Long-term stability was not measured, because the measurements require a high degree of beam-pointing stability. The measured beam pointing in the focus of lens L1 of the focus was 10 % rms over the focus diameter. The measurements were performed after a laser warming-up with a CCD camera and DataRay software. The beam pointing is significantly larger compared with the laser system at 50 kHz, because the amplifier output was not stabilized by a beam stabilization system.

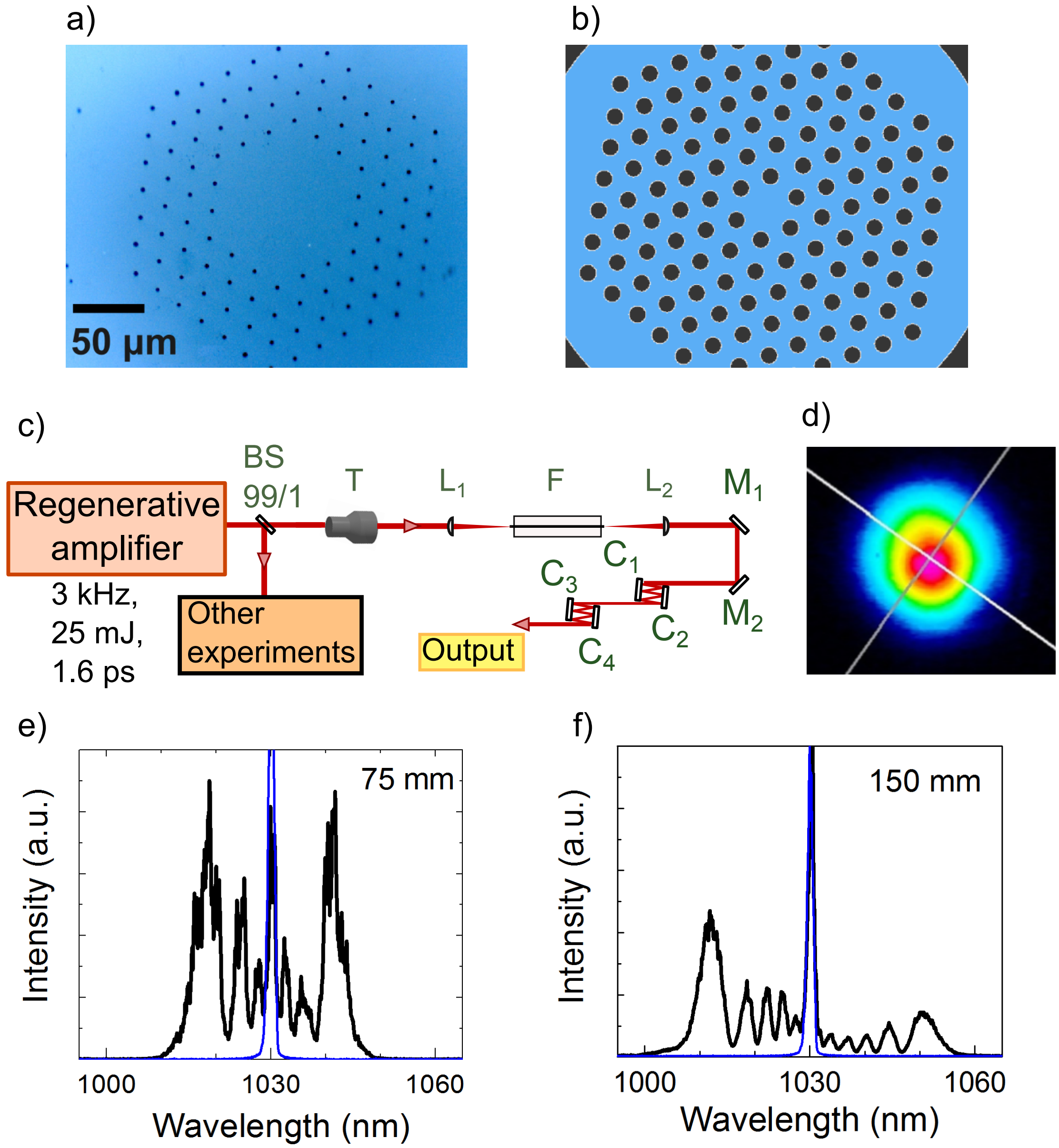

Figure 2.9: Cross-section of LMA-100 (a) and LMA-35 fibers (b). Both fibers are depicted in the same scale; c) Setup of nonlinear pulse compression experiment at 3 kHz repetition rate. Additionally to Fig. 2.7a: BS – beam splitter; d) Coupled-mode of LMA-100 fiber in far-field; e) and f) Input (blue) and output (black) spectra with 75 mm fiber and 150 mm fiber, respectively. The coupled pulse energy is 7 μJ (4 MW peak power) in both cases. A linear laser polarization. Transform-limited pulse duration: 85 fs and 60 fs, input pulse energy: 9 μJ and 10 μJ, respectively.

In addition, WLG was observed in both fibers at 9 μJ pulse energy. This corresponds to 5.5 MW peak power. The output of the white light was highly unstable. After the WLG, the coupling efficiency was lower and the mode shape degraded. The efficiency and the mode could not be optimized indicating the permanent changes of the waveguide after WLG.

2.4 Experiments at 20 MHz repetition rate

The NPC experiments with the LMA-100 fiber were performed both at 3 kHz and at 20 MHz repetition rates. The setup at 20 MHz repetition rate is depicted in Fig. 2.10a. An Innoslab amplifier providing 680 fs pulses with the output power of 600 W was used as the input. The beam was attenuated by a half-wave plate (H) and a thin-film-polarizer (TFP). The rest of the power was blocked by a water-cooled beam block (B). Coupling into the fiber was optimized with a variable magnification telescope (T). A quarter-wave plate (Q_1) mounted in a motorized rotation holder was placed before the coupling lens (L_1), so that the polarization of the laser beam was easily changed from linear to circular. In case of circular polarization of the input, the output polarization of the laser beam was transformed back by another quarter-wave plate (Q_2) after a lens (L_2). A spatial filter (S) was placed at the image position of the lens L_2 to clean the output radiation due to cladding modes. The beam was collimated then by another fused silica plano-convex lens (L_3) and sent to a chirped mirror compressor composed of the mirrors C_{1-4}, described in section 2.1.

Optical components made of fused silica glass were chosen for the experiments. As a result of the low thermal-expansion coefficient of the material, thermal distortions of the beam were kept low. This choice also played a role in the relatively short warm-up time of the system.

In the setup, both the input and the output facets of the fiber were imaged on CCD cameras (CCD_1 and CCD_2) to simplify the coupling. A part of the incident light (4 % due Fresnel reflection) is always reflected from the input facet of the fiber. This reflection was used to image the beam position of the input facet of the fiber. Since the beam transmitted twice the quarter-wave plate (Q_1), its polarization was altered from p to s. A thin film polarizer (P_2) separated the backward propagating Fresnel reflection from the input beam. The front-surface of the fiber was imaged by the lens (L_4) on the CCD camera. A part of the output of the fiber was reflected from an uncoated fused silica wedge (W). For the coupling optimization the CCD camera (CCD_2) was placed at the image position of a lens (L_2) to observe the mode in the near-field. A spatial filter (S) was used to clean the radiation of the fundamental mode from the radiation of cladding modes. In addition, it helped to estimate the coupling efficiency equal to 77 % into the fiber core.

A special fiber holder was made from fused silica glass. Its design relied on the assumption, that the fiber heats up mainly because of its metal holder, which absorbs scattered light from the fiber's cladding. Since the fiber itself is made from fused silica, which has a low absorption, it should not be heated up by light. The ends of the fiber were lying on

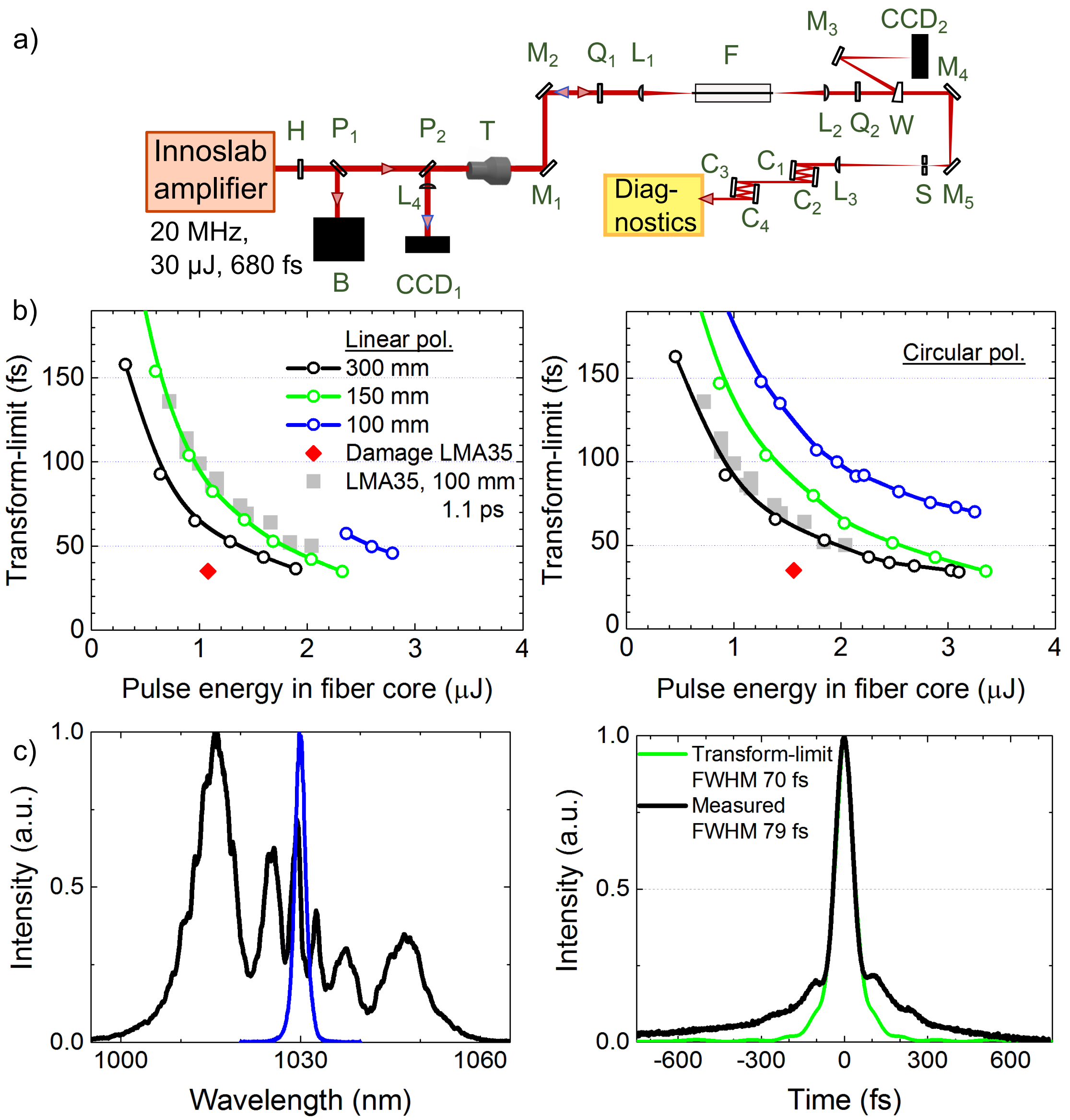

Figure 2.10: a) Nonlinear pulse compression setup at 20 MHz repetition rate. CCD$_{1-2}$ – CCD cameras; W – wedge; S – spatial filter (rest abbreviations are the same as in Fig. 2.8a); b) Transform-limited pulse duration for different fiber lengths with linear and circular polarizations. For comparison: Damage threshold of LMA-35 (red diamonds); LMA-35 with 1.1 ps input pulses at 50 kHz repetition rate, linear polarization (grey squares); c) Measured spectra, autocorrelation and transform-limited pulse intensity with LMA-100 fiber. Fiber length 120 mm, 47 W output power, circular polarization in the fiber.

the V-groove holders made from fused silica, whereas its central part was lying freely in air. The coupling lens (L_1) was fixed on the XYZ translation stage instead of the fiber's holder.

In Fig. 2.10b the transform-limited pulse durations of the measured spectra are plotted versus the pulse energy in the fiber core. The measurements were performed with different fiber lengths: 100 mm, 150 mm and 300 mm. Red diamonds show the damage threshold of LMA-35 fiber at 20 MHz repetition rate and 680 fs input pulses for linear and circular polarization [116]. Grey squares depict the measurements with the 100 mm LMA-35 fiber and the pulse duration of 1.1 ps at 50 kHz repetition rate (see section 2.1) for the comparison. The shortest transform-limited pulse duration was 35 fs. A similar spectral broadening was achieved with 150 mm and 300 mm fiber, indicating the saturation of the spectral broadening. With a linear polarization, the fiber became damaged on average at 2.3 μJ pulse energy in the fiber core. The damage threshold values represent slightly different pieces of fibers used. Similarly, the quality of the cleave might play a role. Compared to LMA-35 fiber with similar input pulses (red diamonds), the same transform limited pulse duration was achieved with the LMA-100 fiber, however twice as high pulse energies were coupled before the fiber damage. The output pulse energies were similar compared to LMA-35 with 1.1 ps input pulses at 50 kHz repetition rate. The fiber got damaged at the peak power close to the critical self-focusing peak power. The fiber got damaged at 3.2 MW peak power for linear and 4.4 MW for circular polarization.

An autocorrelator (Pulse-Check, APE) was used to characterize compressed pulses. We compressed pulses with a chirped mirror compressor. Its mirrors had -540 fs^2 group delay dispersion (GDD) per reflection in the spectral range from 980 nm to 1060 nm. Fig. 2.10c shows the measured autocorrelation trace in comparison to the transform-limited pulse duration (right-hand side) and the measured spectra (left-hand side), where both the input and the output spectra are shown. The reconstructed pulse duration was 79 fs (FWHM), whereas the transform-limited pulse duration calculated from the measured spectrum equals to 70 fs. The light was circularly polarized in the 120 mm long fiber. The output power reached 47 W. Shorter pulses can be achieved with the longer piece of fiber, however a longer piece of fiber was not available for the pulse duration measurements.

The damage of the fiber occurred within about 10 minutes of the irradiation. A quasi-periodic destruction and a crack in the fiber core were visible with the help of an optical microscope (Fig. 2.11a). The observed damages were similar to the periodic damages induced by the fiber fuse effect (Fig. 2.11b [143]). The fuse effect was observed at low continuous-wave powers, when a fiber end-facet was contacted with a high absorbing material ([143, 142]). A quasi-periodic damage pattern can also be generated by thermal heating to 700 – 1000 °C in the absence of laser radiation [144]. The investigation of the thermal damage suggests an exothermic chemical reaction that ignites near 1000°C to increase the local temperature till 1700°C for the "bubble" formation. In our experiment, micro fused-silica particles, which remained on the surface after a cleaving procedure might have induced the fuse effect. In addition, the fiber was only air-cooled, thus high temperatures could be reached within a short time. A special preparation of the fiber ends with the end-caps for a good surface quality and proper cooling may help avoid the fuse induced

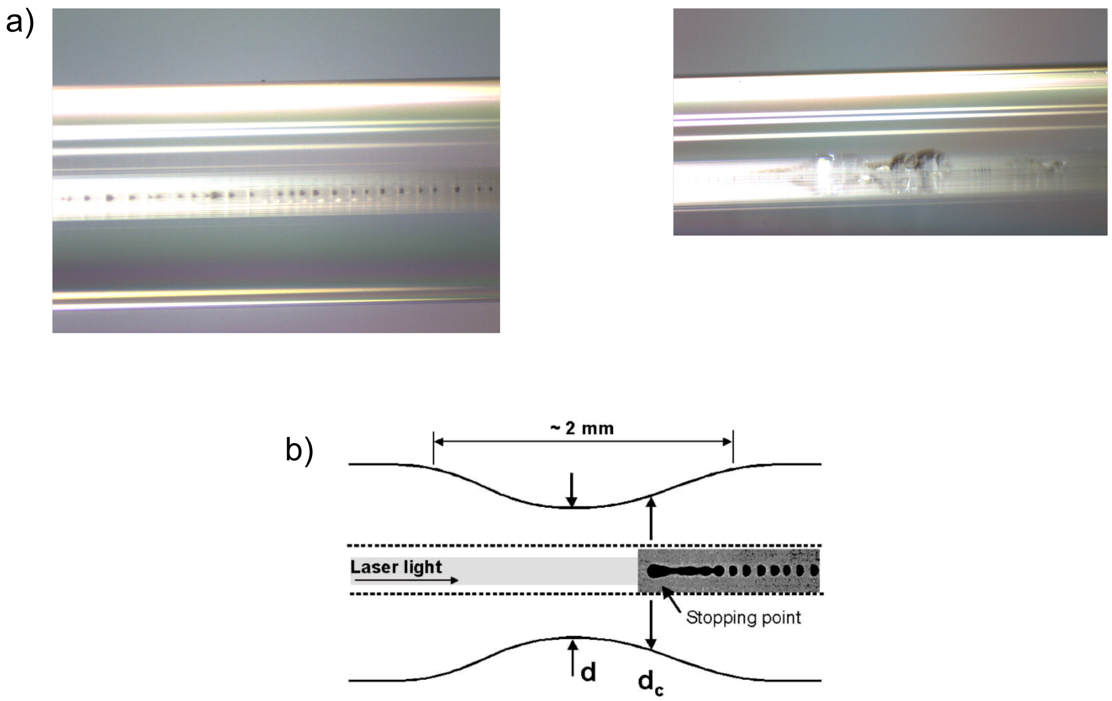

Figure 2.11: a) LMA-100 fiber damages at 20 MHz repetition rate; b) Fiber core destruction by the fuse-effect [142].

damage when operating at high average powers.

2.5 Polarization extinction ratio

The polarization extinction ratio (PER) of the broadened spectra is commonly lower than of the input, because SPM also results in nonlinear polarization rotation. Additionally, the total impact of several nonlinear processes occurring during the pulse propagation, play a role [59, 71]. The PER is an important parameter, because a low PER value leads to energy loss in an experiment containing polarization-sensitive optical elements. Usually, lasers provide PER on the level of more than 20 dB whereas the fiber output suffers from its decrease by to 10 dB [132].

The power was measured separately in p and s polarization states using a polarizer for the estimation of the PER . The value of the PER was calculated from the ratio of the power in the input polarization state and the power in the other polarization state. The PER measurements versus pulse energy in the fiber core and transform-limited pulse duration of the spectra are shown in Fig. 2.12 for different fibers and lasers: a) LMA-35 fiber, 100 mm length, 1.1 ps input pulses at 50 kHz repetition rate; b) LMA-100 fiber, 150 mm length, 1.6 ps input pulses at 3 kHz repetition rate. Both laser beams were linear polarized. At 50 kHz repetition rate, the PER of the input beam was 31 dB, whereas the output beam continuously degraded with energy, down to 12 dB, when the “red-light” generation was

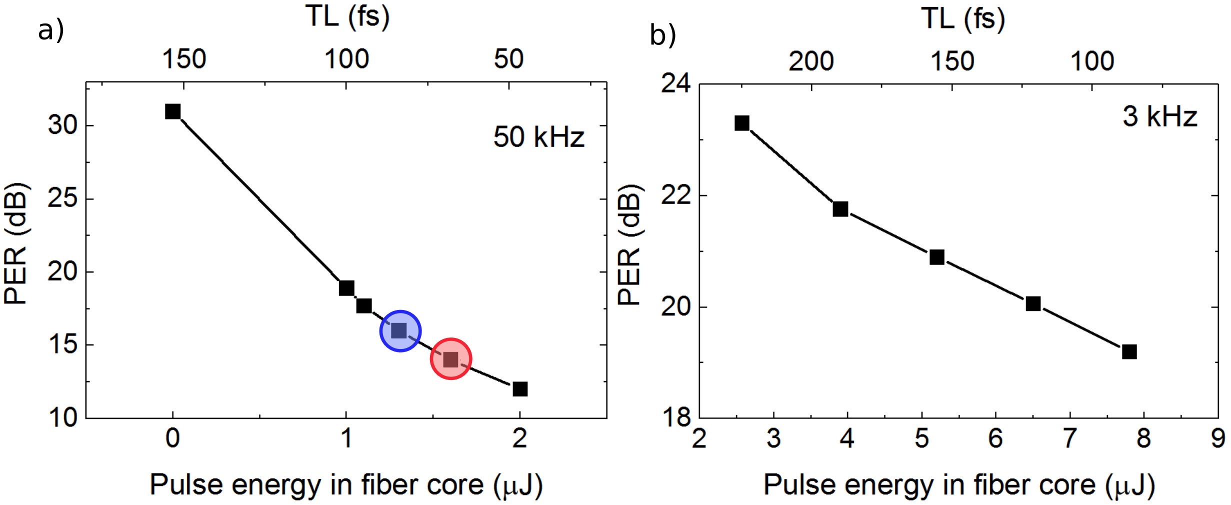

Figure 2.12: Polarization extinction ratio (PER) versus pulse energy in the fiber core and transform-limited pulse durations corresponding to the spectra: a) LMA-35 fiber, 100 mm length, 1.1 ps input pulses at 50 kHz repetition rate; b) LMA-100 fiber, 150 mm length, 1.6 ps input pulses at 3 kHz repetition rate. Linear polarization.

observed with a 100 mm fiber. No significant spectral difference in s and p polarization was measured. For the experimental conditions marked by a blue circle, the PER was improved by 3 dB with a quarter wave plate rotated by 10 degrees from its initial position. A half wave plate additionally added a slight improvement of 0.6 dB. For the experimental conditions at higher output energy (marked by a red cycle), the PER was also slightly improved (2 dB) by a quarter wave plate rotated by 13 degrees. No improvement by a half wave plate was detected. The zero-order retardation plates supported the bandwidth of the output. These additional measurements let us to conclude, that depolarization occured in the fiber. No difference in the PER value was measured achieving the same spectral bandwidth with linear and circular polarization in the fiber.

The tendency was the same with the LMA-100 fiber and input pulses at 3 kHz repetition rate. The PER degrades with the increased pulse in the fiber core, because stronger nonlinearities are accumulated (Fig. 2.12b). In both cases, the PER is still good enough so that the beam can be used further without significant losses in polarization-sensitive optics.

2.6 Four-wave-mixing

“Red-light” output was observed at 3 kHz, 50 kHz and 11 MHz repetition rates with 1.1 ps and 1.6 ps input pulses in LMA-35 and LMA-25 fibers. Its investigation was performed at 50 kHz repetition rate. Spectral measurements indicate that not only light in visible, but also additional spectral components in infrared were generated (Fig. 2.13a). Following [145], degenerate four-wave-mixing (DFWM) in the fiber could be the reason, because

LMA-35 can provide phase matching for signal and idler wavelengths with more than two octaves of separation in the spectrum, since chromatic dispersion of the fiber with such a large core almost equals dispersion of bulk [59]. Additionally, a short fiber length and long input pulses are advantageous for a good overlap of the modes of the interacting waves.

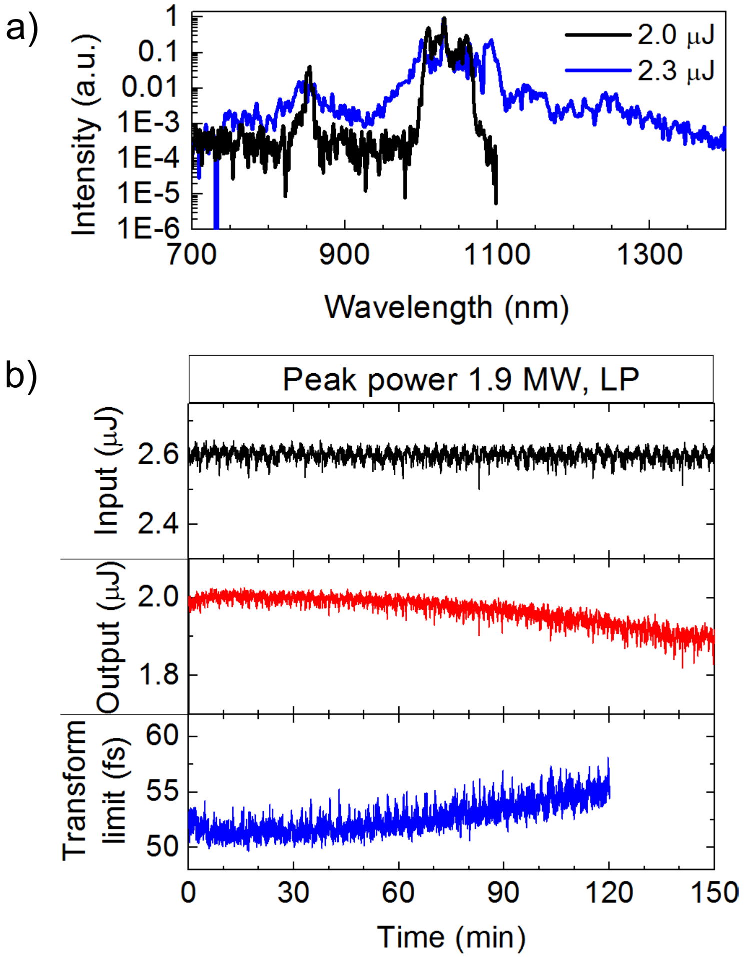

Figure 2.13: a) Spectra of SPM and FWM at 2.0 μJ and at 2.3 μJ output pulse energy; b) Long-term stability of input, output and transform-limit of the spectra. The fiber length 100 mm.

A clear indication of degenerated four-wave mixing (DFWM) are the peaks at 854 nm and 1251 nm (Fig. 2.13a, blue line), which can be explained by $1015nm + 1015nm \rightarrow 854nm + 1251nm$ process. With a 35 mm piece of fiber “red-light” was observed at 4.1 MW peak power for linear and at 5.8 MW peak power for circular polarization, whereas with a 100 mm fiber – at 1.9 MW for linear polarization. This process is hard to quantify, because the generation is not stable in the observed “red-light” output, spectra, and the mode. The generated mode turned out to be less symmetric in the near-field image. Also, part of the power from the core leaked into the cladding producing a complicated diffraction pattern.

After about 30 minutes after its appearance, the “red-light” disappears. The long-term stability measurements indicate total output degradation preventing many applications (Fig. 2.13b). The measurements shown in Fig.2.13 were performed with bare fibers. However, we also tried a 100 mm fiber with end-caps. For the fiber with end-caps, “red-light” generation was observed at the same threshold indicating that the process happens in the fiber but not on its facets. Also, the long-term stability was not improved by using a 100 mm long fiber with the end-caps.

2.7 Summary and conclusions

Nonlinear pulse compression experiments with the spectral broadening in different large-mode-area photonic-crystal-fibers (LMA-15, LMA-25, LMA-35 and LMA-100) were performed with Yb:YAG laser systems (pulse duration: 1.6 ps, 1.1 ps, 1.0 ps, and 680 fs) operating at different repetition rates: 3 kHz, 50 kHz, 11 MHz, and 20 MHz, respectively. Different properties of the NPC systems were investigated in detail, such as the maximal compression factor, the polarization extinction ratio, the optimal compressor GDD, the long-term stability and the damage threshold.

Spectral broadening by SPM saturates with intensity, because the intensity of electromagnetic radiation decreases during propagation due to chromatic dispersion in the medium. The maximal compression factor (the ratio between input pulse duration and the transform limit of the broadest spectrum) was investigated experimentally using different fibers and laser input pulse durations. With 1 ps input pulses the shortest transform-limited pulse was approximately 40 fs using LMA-15 and LMA-25 fibers, with a compression factor of **25**. Experiments with LMA-100 fiber were performed with two different input pulse durations: 1.6 ps and 680 fs. For 1.6 ps input pulses the transform-limited pulse duration of the broadened spectra was 60 fs, which indicates the largest possible compression factor is approximately **27**. For 680 fs input pulses, the duration of the shortest transform-limited pulse was 35 fs, with a compression factor of **19**.

Input pulses of 1.1 ps were compressed to 70 fs (compression factor of **16**) with a chirped mirror compressor achieving an average GDD value of -540 fs^2/reflection and total GDD of 11880 fs^2 in the spectral range of 980 nm to 1060 nm. A compromise in the compressed pulse duration was made taking into account the long-term stability and the pulse energy. Input pulses of 680 fs were compressed close to the transform limit of 77 fs (compression factor of **9**) with a chirped mirror compressor composed of the same mirrors. A compromise here was made taking into account pulse energy.

The required compressor GDD was theoretically estimated and verified experimentally, with agreement to within 18 %. In the case of long input pulses ($\approx$ 1 ps), the largest contribution to the GDD is of SPM, which corresponds to 64 % of total compression needed. This can be explained by the quadratic dependence of the SPM GDD on the input pulse duration (Eq. 1.15).

The polarization extinction ratio (PER) of the spectral broadened output was lower than that of the input, because SPM results in a nonlinear polarization rotation [59, 71]. The PER was only slightly improved by the addition of a quarter- and a half-wave plate, leading us to conclude that depolarization occured in the fiber.

Experiments were performed with linearly and circularly polarized input. It was found experimentally that the amount of GDD compensation needed was the same for both linear and circular polarization inputs to the fiber. Additionally, the output PER value was similar using both linear and circular polarization as the fiber input. This is particular interesting as the critical self-focusing limit is higher for circularly polarized fiber inputs. The achieved PER value (14 dB) in the output beam is sufficient to avoid significant losses at polarization-sensitive optics.

The main difference observed between NPC at kHz and MHz repetition rates was the damage threshold. Experimentally, we reached the critical self-focusing peak power for both linear and circular polarization in an LMA-35 fiber at low (50 kHz) repetition rate. Owing to the ultra-stable beam pointing of the 50 kHz laser system, the long-term stability was measured for up to 8 hours. The damage at low average power was not well defined, instead output pulse energy degradation and scattering into higher order modes (close to the critical self-focusing) were observed. Additionally, no damage was observed on input and output facets or inside the fiber after this. This indicates that the output power degradation happened due to a change of the refractive index of the fiber material. The output power degradation observed in our experiments was similar to the Type I damage of a dielectric material, it is associated with a permanent change of refractive index without structural damage due to generated electron-hole plasma produced by multiphoton band-to-band transitions [146]. The observed degradation of the output is also reminiscent of other laser systems based on the Kerr-effect, such as Kerr-lens mode locked oscillators. These observations indicate that when the Kerr-effect is implemented in a laser system (such as Kerr-lens mode locking, self-phase modulation), the structure of the medium is altered by light, reducing the performance of the system with time.

The damage threshold of an LMA-35 fiber for linear polarization was about 2 MW peak power at MHz repetition rate with 1 ps pulses.

"Red-light" output was observed at 3 kHz, 50 kHz and 11 MHz repetition rates with 1.1 ps and 1.6 ps input pulses in the LMA-35 and LMA-25 fibers. Spectral measurements indicated that not only light in the visible range was generated, but also additional spectral components in the infrared range. This is a clear indication of degenerate four-wave mixing (DFWM), were the peaks at 854 nm and 1251 nm, which can be explained by $1015nm + 1015nm \rightarrow 854nm + 1251nm$ parametric process. The generation was unstable in the output power, spectra, and the mode, because the threshold of DFWM was close to the critical self-focusing peak power. Long-term stability measurements indicated a total output degradation preventing many applications, and was not improved by using a fiber with the end-caps.

A clear advantage of LMA-100 over LMA-35 fibers was indicated for MHz repetition rate. With 680 fs input pulses, comparable transform limited pulse durations were achieved, however pulses of double the energy could be coupled into the LMA-100 fiber without damage. The damage threshold of the fiber was reached close to the critical self-focusing peak power. The LMA-100 fiber was damaged at 3.2 MW peak power for linear and 4.4 MW for circular polarization at 20 MHz repetition rate. A special fused silica glass fiber holder was designed to avoid heating of the fiber due to absorption of scattered light from the fibre's cladding, as would be assumed to happen for a metal holder. Since the fiber itself is made from the fused silica, which has a low absorption, it should not be heated by light, however, the observed fuse-effect indicated the opposite. The fuse-effect can be observed when a fiber is heated to 700 - 1000 °C with or without laser radiation [143, 144, 142]. Due to impurities in the fiber, exothermic chemical reaction can ignite near 1000°C increasing the temperature to 1700°C resulting in "bubble" formation. The fuse-effect might be avoided by the end-caps (the heating-up of the surface can be avoided by a better quality of a surface: a polished surface of an end-cap is better than a cleaved facet) and proper cooling of the fiber. In addition, the observation of the fuse-effect indicated that the purity of a fused silica used in a production of LMA PCF fibers may not be high enough for a higher damage threshold at MHz repetition rate.

The investigation of a double-stage NPC with 1 ps input pulses was also performed. Due to the critical self-focusing peak power, only a fraction of the first NPC stage output (30 %) could be used. To utilize the whole laser power, a combination of NPC with chirped pulses was considered. We found that pulses were hardly compressible. For a Gausian pulse, instantaneous frequency has a single maximum and a single minimum. For a non-Gaussian pulse, the same spectral components are generated, but with a different time dependency, meaning that the instantaneous frequency peaks multiple times (Fig. 1.2). This results in a complex spectral phase, which is hard to compensate. A similar situation was predicted by simulations of transform-limited input pulses, because pulses become chirped when propagating in the second piece of the fiber (Fig. 2.6a). An alternative approach for achieving an octave-spanning spectrum and few-cycle pulses with 1 ps input pulses could be white light generation in crystals with compressed pulses out of the first NPC stage.

Chapter 3

High power 100 kHz repetition rate laser

In this chapter, a design and a realization of a high power laser is described based on Yb:glass and Yb:YAG amplifiers. The aim of the project was to develop a pump for a broadband OPCPA supporting few cycle CEP-stable pulses of a central wavelength of 2 μm and a repetition rate of 100 kHz. The spectral range and the repetition rate of the OPCPA is interesting for different applications, such as investigations of MED and OHG generation. Higher photon energies reaching a water window between 4.4 - 2.3 nm can be achieved by an OHG driven by laser pulses in mid-infrared compared to visible and near-infrared spectral ranges, because the cut-off of an OHG depends on the wavelength of the fundamental radiation. Investigations on DNA and other bio-molecules can be performed using such a table-top coherent X-ray source. For some applications, a pulse repetition rate of 100 kHz is optimal, because it should be low enough compared to the speed of acquisition electronics used in experiments like COLTRIMS.

3.1 Innoslab booster requirements

The laser source consists of different types of high power Yb amplifiers. The design of the Innoslab amplifier, described in Chapter 1, is optimized for the maximal average power of 600 W independent of a pulse repetition rate.

The seed of the Innoslab amplifier should meet several requirements to obtain the target parameters of 6 mJ at 100 kHz (600 W):

(i) Average input power 5 W;

(ii) Spectral bandwidth 1.5 - 3 nm;

(iii) Central wavelength 1030 nm;

(iv) Tolerable beam quality factor: $M^2 < 1.2$; Optimal: $M^2 < 1.1$;

(v) Beam pointing $< 1/10$ beam diameter for the frequency of > 0.1 Hz; beam pointing uncritical for the < 0.1 Hz frequencies.

(vi) Long-term stability of a beam diameter and a beam divergence (< 10 %).

(vii) Stretched pulse duration ≥ 500 ps for < 2 nm spectral bandwidth.

(viii) Interlocks monitoring power and the bandwidth of the oscillator and the seed.

3.2 Ti:Sapphire front-end

The layout of the high power Ti:Sapphire front-end OPCPA is shown in Fig. 3.1. The output of the Ti:Sapphire oscillator is split into two parts. One part is used to seed the pump laser of the OPCPA. The pump consists of a chain of Yb:glass and Yb:YAG amplifiers. The other part is used to seed the OPCPA. Pulses are stretched in bulk to prepare for the first OPCPA stages. The pulses are then compressed by a chirped mirror compressor and are used for DFG, stretched again and amplified further in mid-infrared OPCPA stages with the following compression. The target parameters of the OPCPA output are: 100 kHz, 200 μJ, < 10 fs at 2 μm central wavelength. The realization of the OPCPA is in the scope of the PhD work of Harald Fuest and is described in his thesis.

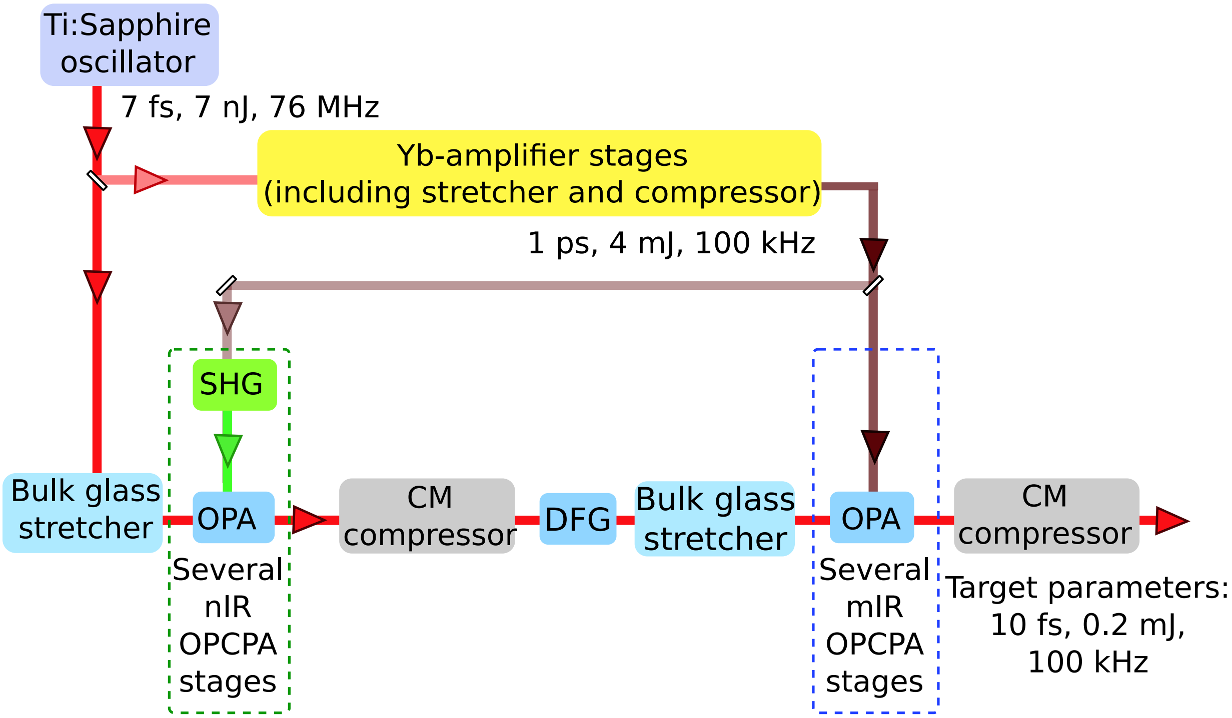

Figure 3.1: Setup of Ti:Sapphire front-end OPCPA system.

As a master oscillator the Ti:sapphire laser (FEMTOSOURCE Rainbow, Femtolasers GmbH) was used, delivering 575 mW of average power in <7 fs pulses at a repetition rate of 77 MHz [96]. The setup of the CPA pump chain is shown in Fig. 3.2. It consists of:

- Ti:Sapphire oscillator;
- Soliton self-frequency shifter (SSFS) in a highly nonlinear photonic crystal fiber;
- Fiber pre-amplifier;
- Stretcher;
- 50 dB gain amplifier (regenerative or fiber amplifier);
- Innoslab;
- Compressor.

The average power of the Ti:Sapphire oscillator was 143 μW (1.8 pJ pulse energy) at a central wavelength of 1030 nm and a FWHM bandwidth of 4 nm. The mode of the laser is shown in Fig. 3.3a. The mode of the laser at 1030 nm central wavelength and 4 nm FWHM spectral bandwidth is shown in Fig. 3.3b. The power was measured with a germanium photo diode filtering the output with a laser line filter. The output was unfortunately too low to avoid the amplified spontaneous emission in the fiber pre-amplifier significantly reducing the temporal contrast of amplified pulses [149]. In addition, the mode profile of the Ti:Sapphire oscillator at 1030 nm central wavelength resulted in a low coupling efficiency in the fiber pre-amplifier.

An SSFS was employed in a highly nonlinear photonic crystal fiber (HNLF) to obtain a higher pulse energy and a better mode profile to seed the pump laser. The schematic representation of the setup is shown in Fig. 3.4a. Part of the oscillator output (31 mW, 0.4 nJ, 5 % of the total output) was focused by an aspheric lens (focal length 7.5 mm) into a 1.6 μm core diameter 25 cm long HNLF (NKT Photonics, NL-PM-750 PCF). The output beam was collimated by another aspheric lens (focal length 7.5 mm). For the power measurements, the output of the HNLF was filtered by a longpass filter (F_1) with a cut-off wavelength at 950 nm and additionally by a laser line filter (F_2) with a bandwidth of 4 nm at FWHM. The spectrum of the Ti:Sapphire oscillator (orange) and a spectrum after the HNLF (blue) are shown in a logarithmic scale in Fig. 3.4b. The spectra were measured with an Ocean Optics spectrometer HR4000CG-UV-NIR. Under optimum conditions the coupling efficiency into the fiber was 30 %. The central wavelength of the red-shifted spectrum was fine tuned to match 1030 nm by carefully adjusting the input pulse energy. The peak of the soliton became shifted further in the infrared and the peak of the soliton decreased with the higher input pulse energy. As a result, it was not possible to generate higher spectral power density at 1030 nm. The soliton contained 3 mW in 38 nm FWHM bandwidth, as it was measured with the longpass filter F_1. Using the laser line filter F_2, 0.3 mW was measured in the 4 nm bandwidth FWHM centered at 1030 nm. The resulted

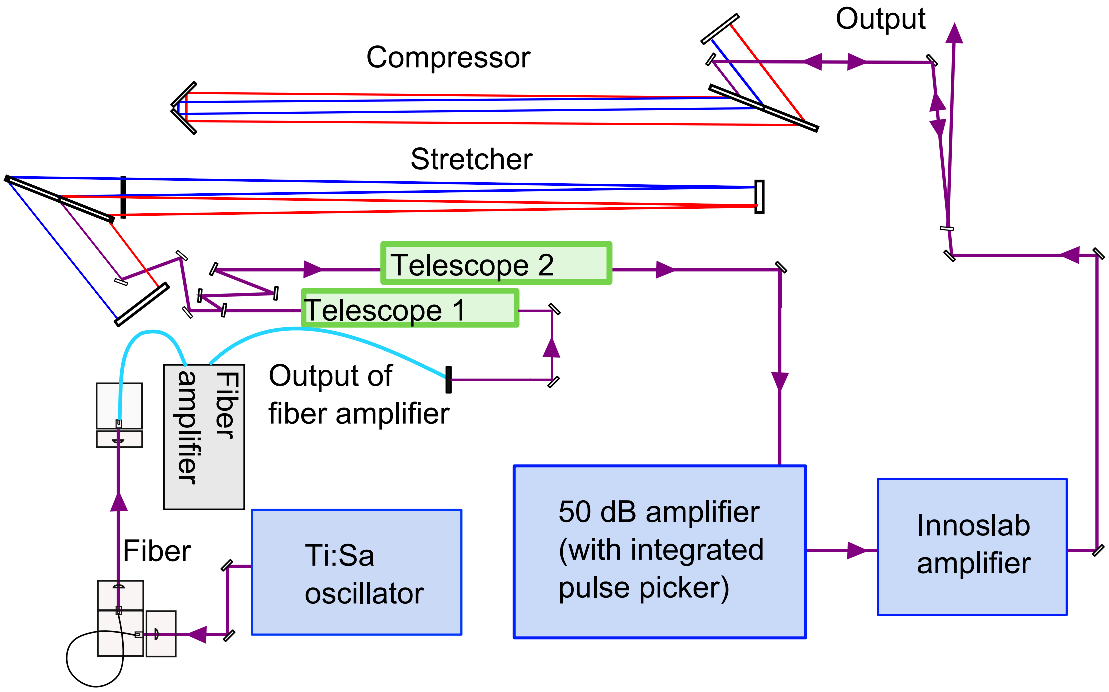

Figure 3.2: Setup of OPCPA pump laser.

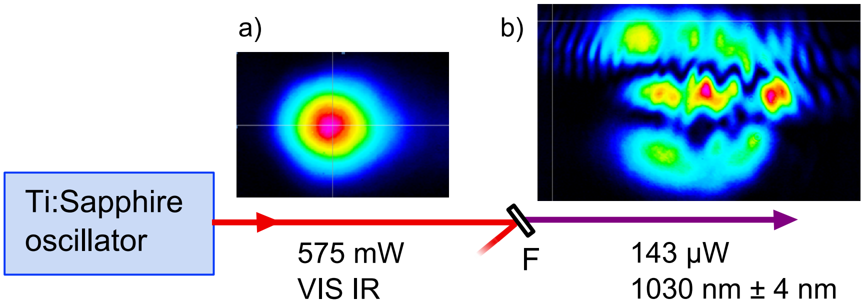

Figure 3.3: The mode of Ti:sapphire oscillator in visible (a) and in infrared at central wavelength of 1030 nm and 4 nm bandwidth (b).

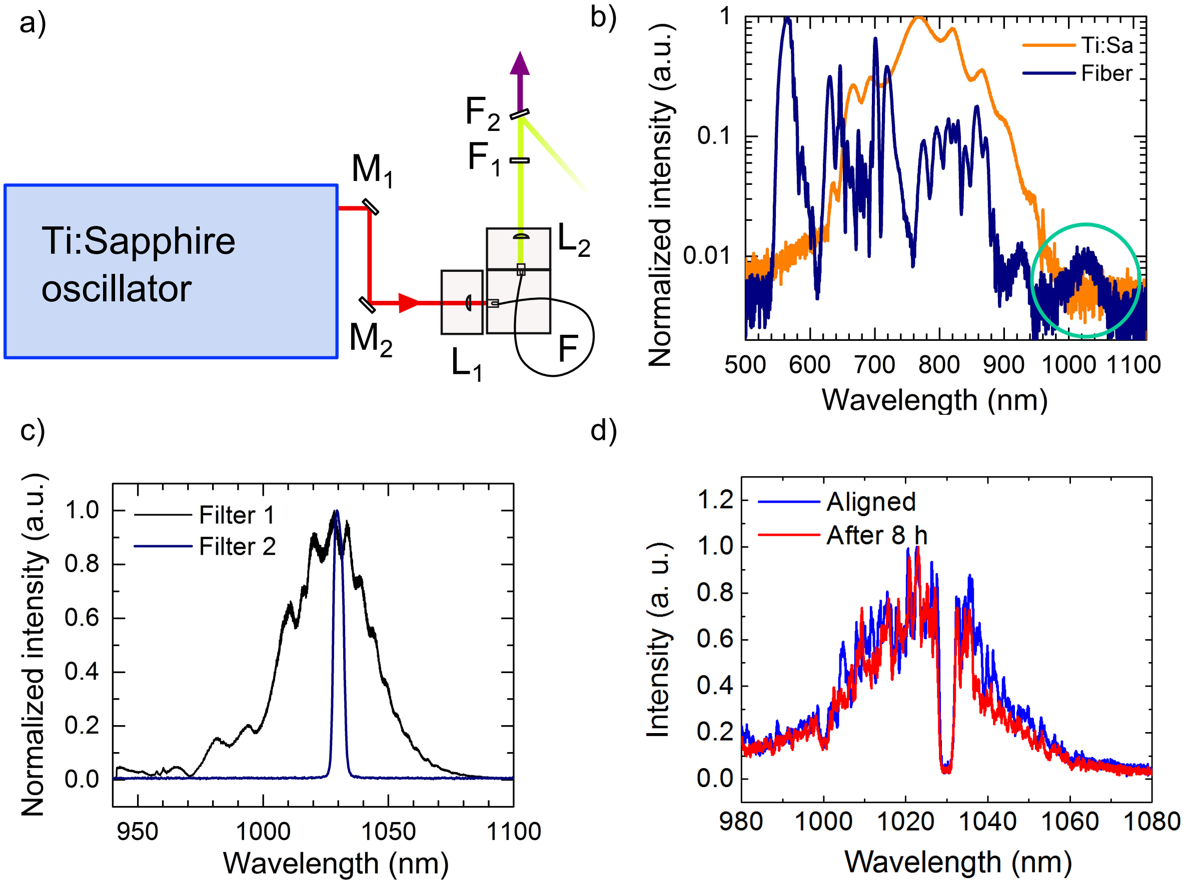

Figure 3.4: a) Seed generation for the OPA pump by soliton self-frequency shifting. M_{1-2} – silver mirrors, L_1 – achromatic coupling lens, focal length 7.5 mm; F – highly nonlinear polarization maintaining PCF, core diameter 1.6 μm, 25 cm length, FC-PC connectors at both ends, NKT Photonics, NL-PM-750; L_2 – achromatic collimating lens, focal length 8.0 mm; F_1 - longpass filter, cut-off wavelength at 950 nm; F_2 – laser line filter, bandwidth 4 nm FWHM; b) Ti:sapphire spectrum (orange) in comparison with a spectrum after the highly-nonlinear fiber (blue) in a logarithmic scale; c) Soliton spectra measured after filters F_1 and F_2; d) Monitoring of coupling stability by measuring the reflected spectra after filter F_2.

output power was 2 times higher than the power directly available from the Ti:Sapphire oscillator. The power was measured using a Germanium photo diode. Additionally, the mode profile was excellent, as one can expect from the fiber output. The soliton spectra after the filters are shown in Fig. 3.4c. The spectra were measured with a high resolution IR spectrometer Ocean Optics HR4000. The fiber and the collimating lens were mounted on a 3-axis translation stage (Thorlabs ManoMax). The coupling lens was fixed on an extension platform (Thorlabs AMA007/M) making the setup very compact and easy to align. No active stabilization was used, because as shown in Fig. 3.4d, the coupling was perfectly stable over a period of 8 hours. The reflected light from the F_2 filter was used to monitor the long-term stability of the soliton. A slight alignment was only required if the oscillator was switched off and on.

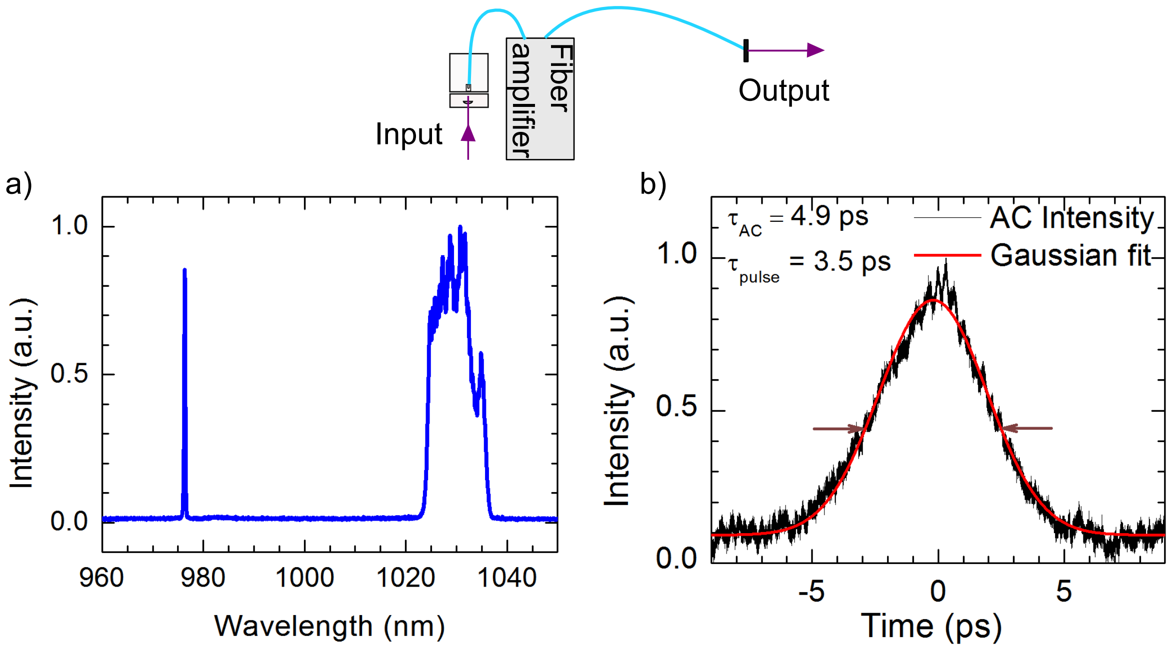

Figure 3.5: a) Output spectrum of the fiber amplifier, total average power 100 mW; b) Autocorrelation of the output of the fiber amplifier, autocorrelation pulse duration 4.9 ps, pulse duration 3.5 ps.

The output of the HNLF was amplified in the fiber pre-amplifier. The pre-amplifier, designed in the Institute of Applied Physics, Jena, Germany, delivered 100 mW (1.3 nJ pulse energy) average power in a spectral bandwidth of 9 nm FHWM centered at 1030 nm. The gain of the pre-amplifier was 22 dB. The spectrum of the amplifier output is shown in Fig. 3.5a. The narrow peak is the rest of the pump at 976 nm. The autocorrelation of the output was measured with the Femtochrome autocorrelator FR-103PD (Fig. 3.5b). Pulses were temporally stretched to 3.5 ps FWHM due to the material dispersion in the fiber pre-amplifier. Pre-amplified pulses were stretched further in a grating stretcher to fulfill the requirements for the Innoslab amplifier ((vii)).

The result of the beam quality factor M^2 measurements of the Innoslab amplifier at the highest output power of 600 W is shown in Fig. 3.6. The measured M^2 values were $M_x^2 = 1.09$, $M_y^2 = 1.43$. The measurements were performed with a beam propagation analyzer (Spiricon M2-200-FW-SCOR). Different values of M^2 in two orthogonal directions are typical for the innoslab design, as described in section 1.3. The Innoslab also contains a water cooled isolator designed for high power applications (Amphos).

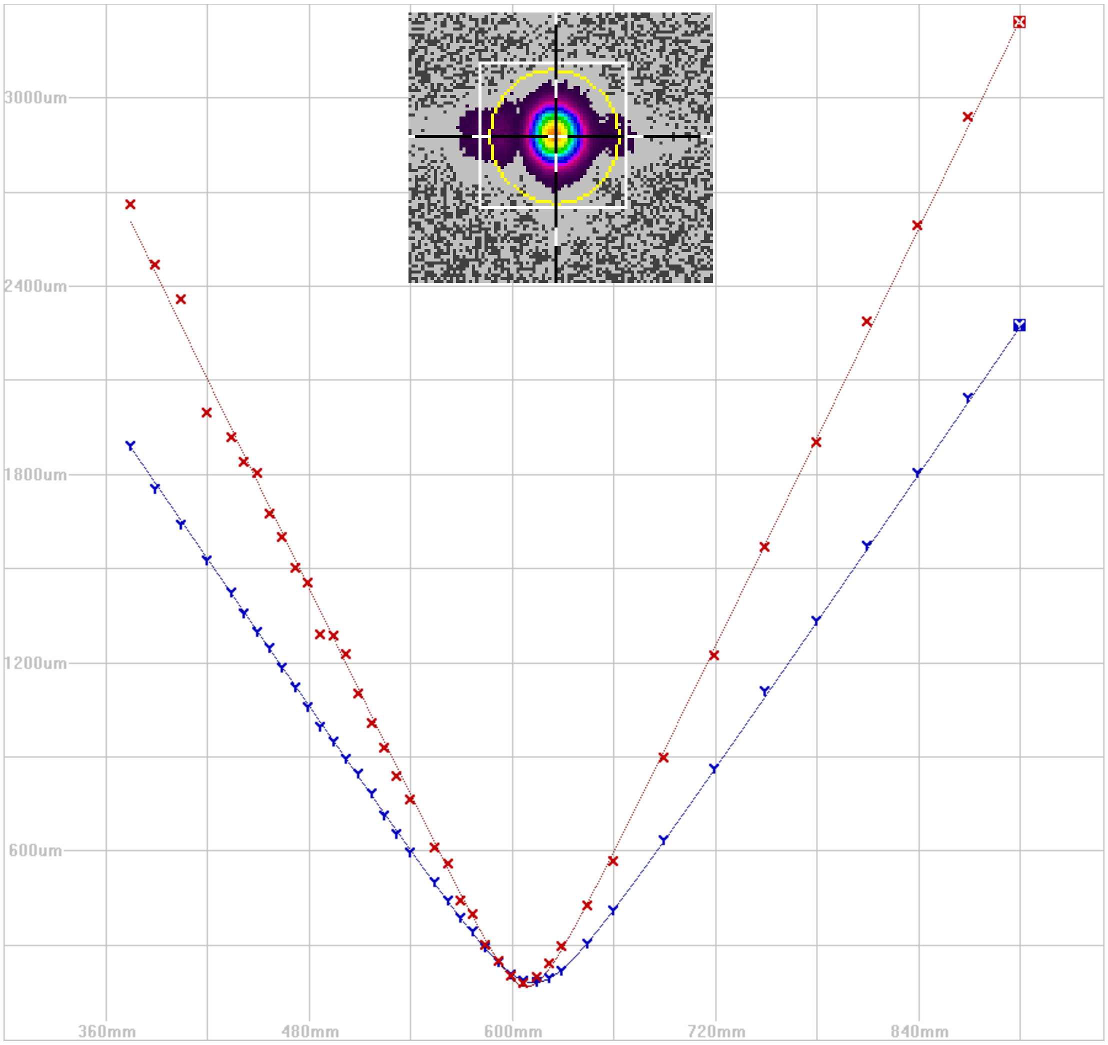

Figure 3.6: M^2 factor measurements of the Innoslab output at the highest output power of 600 W: $M_x^2 = 1.09$, $M_y^2 = 1.43$; Beam profile in the focus.

3.3 Chirped pulse amplification

3.3.1 Stretcher design and realization

A chirped pulse amplification (CPA) [151] is used to reduce the peak power in amplifiers. Otherwise, the output pulse energy is limited by the optical damage or pulse distortions due to nonlinearities in optical components. Prior to the amplification, pulses are temporally stretched with a dispersive delay line introducing different path lengths to different frequency components of pulses. Following the amplification, pulses are recompressed by another delay line introducing the opposite dispersion of the initial stretcher.

The designed stretcher is based on a conventional Martinez-type grating stretcher scheme [152]. Assuming a Gaussian spectrum of input pulses, a required GDD for stretching nearly transform limited pulses (FWHM pulse duration τ_0) to the desired FWHM pulse duration τ_{out} can be calculated by the equation [153]:

$$GDD = \frac{\tau_0}{4\ln 2}\sqrt{\tau_{out}^2 - \tau_0^2} \tag{3.1}$$

where

$$\tau_0 = \frac{2\ln 2}{\pi c}\frac{\lambda_0^2}{\Delta\lambda} \tag{3.2}$$

λ_0 is a central wavelength; $\Delta\lambda$ - spectral bandwidth; c - speed of light.

The length of the stretcher can be calculated by the equation [154]:

$$L_{stretcher} = -\frac{GDD \cdot c}{2\omega_0 D^2} + 4f \tag{3.3}$$

$$D = -\frac{2\pi c N}{\omega_0^2 cos\beta}$$

$$\beta = arcsin(sin\alpha - N\lambda_0)$$

where ω_0 is the angular frequency at the central wavelength, $\omega_0 = 2\pi c/\lambda_0$; D – angular dispersion; f – focal length of a lens, f = 1.2 m; N – line density (lines/mm) of a diffraction grating; β – first-order diffraction angle; α - angle of incidence on a diffraction grating.

The distance from the grating to the lens is an important parameter when building a stretcher. The adjustment of its precise value plays a role in the correct imaging and thus a good beam profile after the stretcher. It can be seen from the scheme in Fig. 3.7a, that the distance is equal to:

$$b = \frac{L_{stretcher} - 2f}{2} \tag{3.4}$$

Following the Innoslab seed requirements, we can estimate the GDD of the stretcher. Since the expected spectral bandwidth of the Innoslab is 1.5 nm [155] due to the gain

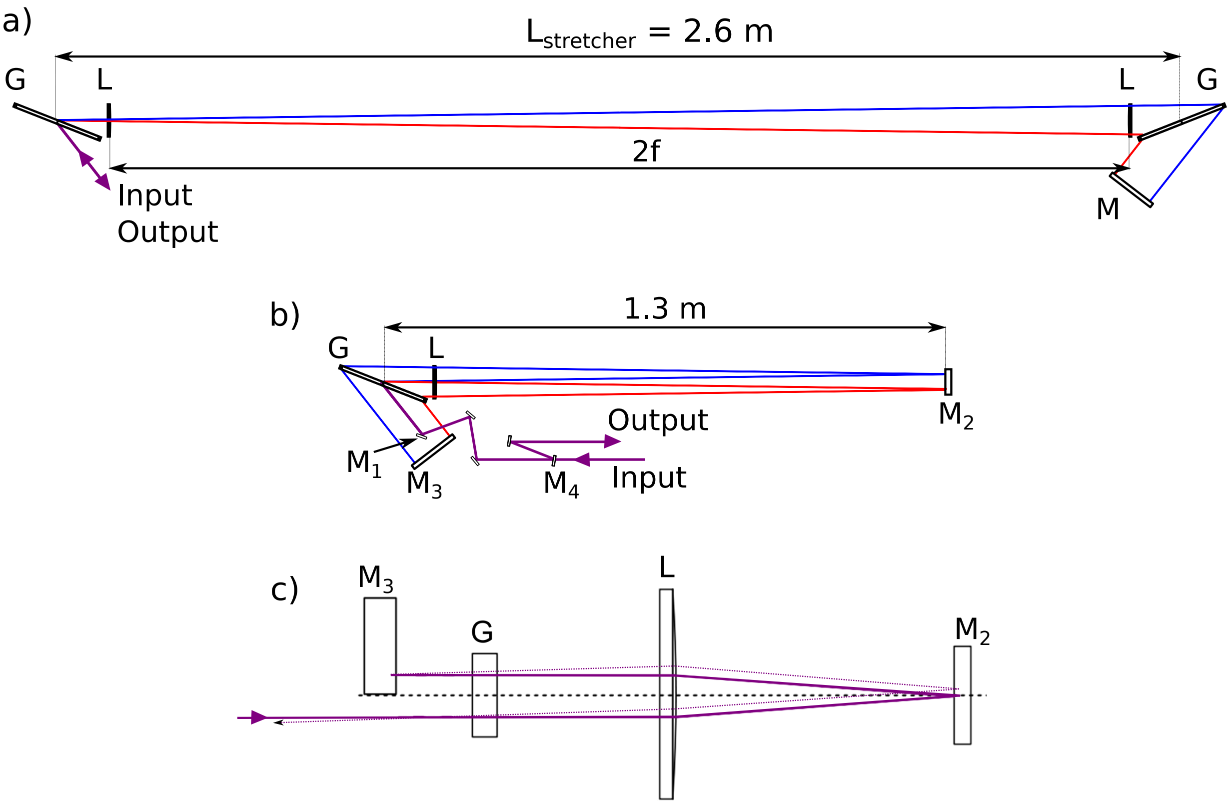

Figure 3.7: a) Stretcher design with two gratings (top-view). G – transmission refraction grating, 1740 lines/mm, CMN Optics, Jena IOF; L – plano-convex lens, focal length 1.2 mm; M – dielectric end-mirror, dimensions: 120 mm × 30 mm. Stretcher supports 6 nm bandwidth. Red and blue lines mark the longest and the shortest wavelengths of the supported spectral bandwidth. Size of optics and distances are in scale; b) Stretcher design with a single grating (top-view). M_{1-4} - dielectric mirrors. Size of optics and distances are in scale; c) Beam way in single-grating stretcher (side-view). Dashed line marks center of the optics (grating, lens and mirror M_4). Off-set of the input beam from the center of the grating and the lens: 7 mm. Only size of optics is in scale.

narrowing, the chirped pulse duration should be 500 ps per 1.5 nm bandwidth (vii). In order to stretch seed pulses from $\tau_0 = 1$ ps, as calculated assuming a FWHM of 1.5 nm, to the desired pulse duration of 500 ps, the GDD induced by the stretcher should be $+1.88 \times 10^8$ fs^2.

The design of the stretcher with two gratings is shown in Fig. 3.7a. The size of the optics and the distances between them are in scale. By putting a folding mirror (M_2) in the center, a simpler way of building the stretcher with a single grating can be achieved (Fig. 3.7b). The advantage of the stretcher with one grating is not only compactness, but also alignment. The grating-based stretcher and compressor pairs are very sensitive to the alignment. In a two-grating stretcher, the gratings have to be aligned precisely so that the lines of both gratings are parallel to each other. This issue is solved completely for one-grating stretcher and compressor, because angles of different wavelengths are imaged correctly on the same grating, if the positions M_2 and L are adjusted correctly.

An inch flat mirror (M_1) steered the incoming beam having a $1/e^2$ diameter of 2 mm to the grating (G). The grating diffracted the beam towards a 3-inch plano-convex lens (L) with a focal length of 1.2 m, AR-coated. The beam passed the lens with a slight (7 mm) offset from the center down. The side-view of the stretcher is depicted in Fig. 3.7c. Dashed line marks the center of the optics (gratings, lens and mirror M_4). The solid violet line shows an incoming beam and the dashed line - the reflected beam from the end-mirror M_2. The output beam was slightly lower than the input. As a result, it was possible to separated the output from the input by the mirror M_4, which was placed lower in order not to disturbed the input. Mirror M_2 is placed in the focus position of lens L. The stretcher was designed for angle of incidence of 59.5°, bearing in mind both the compactness and the efficiency. The stretcher supported a 6 nm spectral bandwidth limited by the dimensions of the optics. The red and the blue lines mark the longest and the shortest wavelengths of the supported spectral bandwidth.

We have used fused silica transmission gratings with 1740 lines/mm from CMN Optics, Jena IOF for the stretcher and the compressor. The photo of the grating is shown in Fig. 3.8a. The gratings are of high diffraction efficiency and uniformity (Fig. 3.8b and Fig. 3.8c). The highest efficiency at a 63° angle of incidence was 95.5 % (Fig. 3.8b). The gratings are manufactured from high-purity fused silica and exhibit a higher damage threshold and lifetime compared with metal diffraction gratings. Thermal distortions are also low because of the low thermal expansion coefficient of the material.

The pulse duration after the stretcher was measured with an ultrafast photo diode (ALPHALAS UPD-200-SP, specified rise time < 175 ps) together with a GHz oscilloscope (Agilent Technologies, InfiniiVision DSO-X 4104A, 1 GHz, sampling rate 5 GSa/s). We measured the response function of the diode and the oscilloscope by measuring 1 ps pulses of a fiber oscillator (Fig. 3.9b). The measured rise-time (204 ps) and fall-time (436 ps) indicates that the devices are suitable for the characterization of the stretched pulses with the pulse duration of 2 ns in 6 nm FWHM bandwidth (Fig. 3.9a). The spectra of the fiber pre-amplifier and the stretcher are shown in Fig. 3.9c. The stretcher efficiency was 50 %. The stretcher efficiency in 4 nm bandwidth was 62 %, which is expected from the efficiency of the grating, the lens and the mirrors. The reflection efficiency of the folding

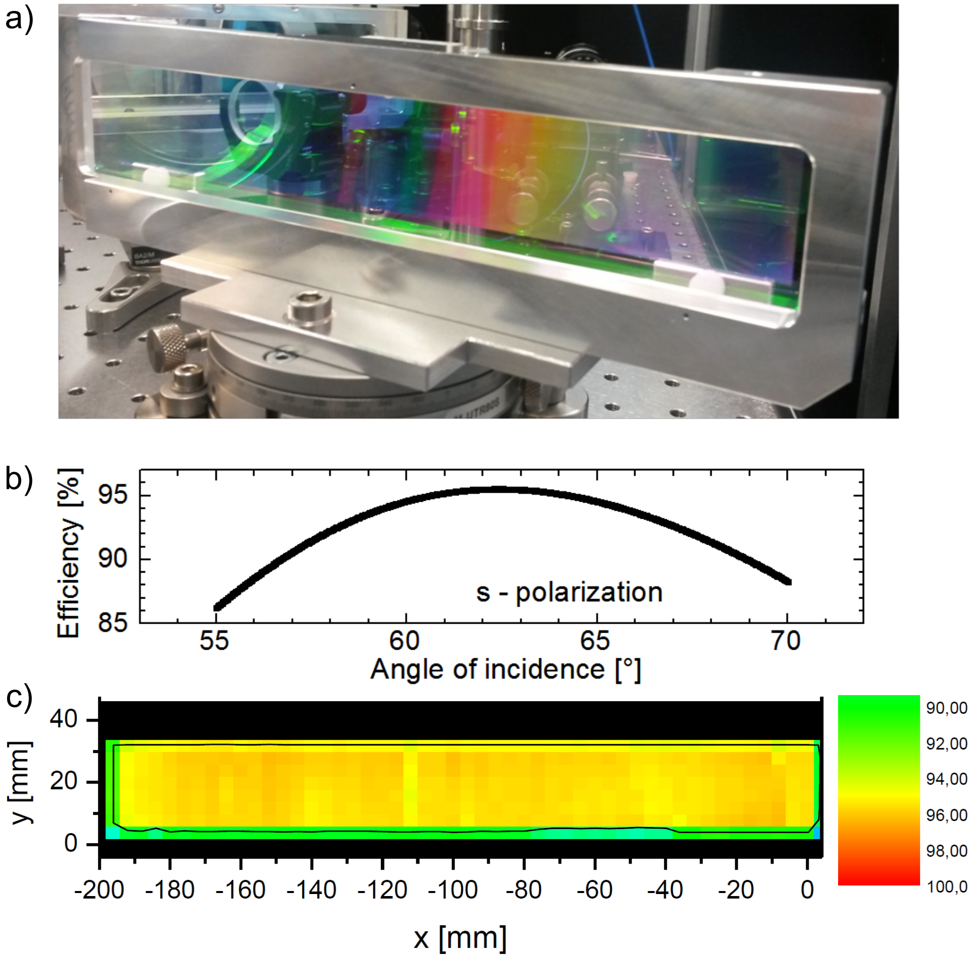

Figure 3.8: a) Photo of a transmission fused silica diffraction grating in a specially designed mount, grating dimensions: 205 mm × 30 mm; b) Theoretical diffraction efficiency versus the angle of incidence [150]; c) Measured efficiency along the surface of the grating at an incidence angle of 63° [150].

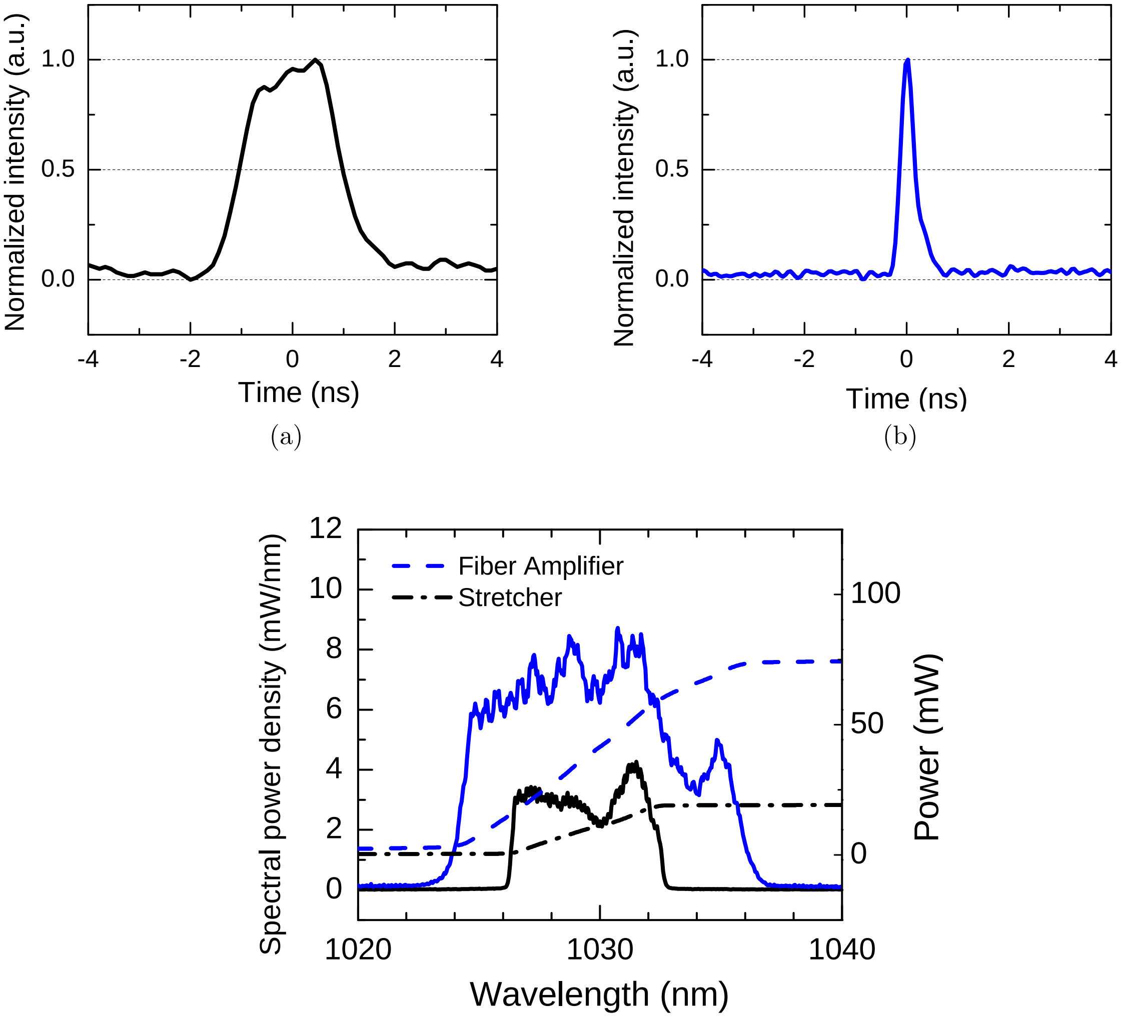

(a)

(b)

(c)

Figure 3.9: a) Pulse duration after stretcher, 2 nm FWHM for 6 nm spectral bandwidth FWHM; b) Photo-diode response function; c) Input (blue) and output (black) spectra of the stretcher. Spectral power density is calibrated to the output power.

mirror was only 98 %. The efficiency of anti-reflection coating of the lens also played a role, because the beam passed the lens surface 8 times. The output power was 33 mW (0.4 nJ pulse energy). In the following subsection, a design of the pulse compressor is presented to re-compress the amplified stretched pulses.

For the laser safety, interlocks were installed in the stretcher, as listed in the Innoslab requirements. The red and the blue spectral components, which did not fit on the folding mirror M_2 were focused onto two photo-diodes. The interlock signal was necessary for the safe operation of the Innoslab. The Innoslab amplifier could get damaged, if the mode-locking of the Ti:Sapphire is disturbed. In case of the abrupt loss of the seed signal, the Innoslab amplifier would start lasing even with a small feedback in the laser system [155].

3.3.2 Compressor design and realization

A Treacy-type parallel grating pair [156] can provide a dispersion matched with that of the Martinez-type stretcher. The length of the compressor can be calculated by the equation:

$$L_{compressor} = \frac{2\pi GDD(c \cdot cos\beta)^2}{X\lambda_0^3 N^2} \tag{3.5}$$

where X is the number of passes. The GDD is the same as that of the stretcher, not taking into account the GDD of the amplifiers.

The third order dispersion (TOD) of the compressor is $-3.5 \cdot 10^9$ fs^3, as calculated by the equation given in [154]. The TOD plays a role, if TOD $> \tau_0^3$ [157], which is the case for 1 ps pulses. However, a system of a Martinez-type grating stretcher and a Treacy-type compressor allows compensation of all orders of dispersion coefficients, since the optical path length of all spectral components is the same in the stretcher and the compressor [158]. However, even with the exact design, the material dispersion of the in-between laser amplifiers restricts the exact compensation of all orders of dispersion coefficients. In order to correct the residual TOD, a simultaneous tuning of both the grating separation as well as the angle of incidence is required for getting close to the transform-limited pulse duration after the compressor [159].

The design of the compressor with a calculated distance between the gratings ($L_{compressor}$ = 2.2 m) is shown in Fig. 3.10a. The design with the one grating is shown in Fig. 3.10b. In the compressor setup, the folding mirror is made up of two high-reflector mirrors mounted at 90° to each other. The compressor was designed for a 5 mm beam diameter keeping the intensity on the grating of 30 mJ/cm^2, which is well below the damage threshold of the gratings 1 J/cm^2 [150].

For pre-alignment, we sent stretched pulses directly into the compressor without the amplification in between. We have measured a compressor through-put efficiency of 77 % indicating, as expected, a 94 % efficiency of the grating per pass. The autocorrelation of the compressed pulse duration was measured with an autocorrelator (APE, PulseCheck). The autocorrelator detected a weak signal and measured about 600 fs pulse duration. The expected autocorrelation pulse duration is 550 fs from 400 fs transform limited pulses. The

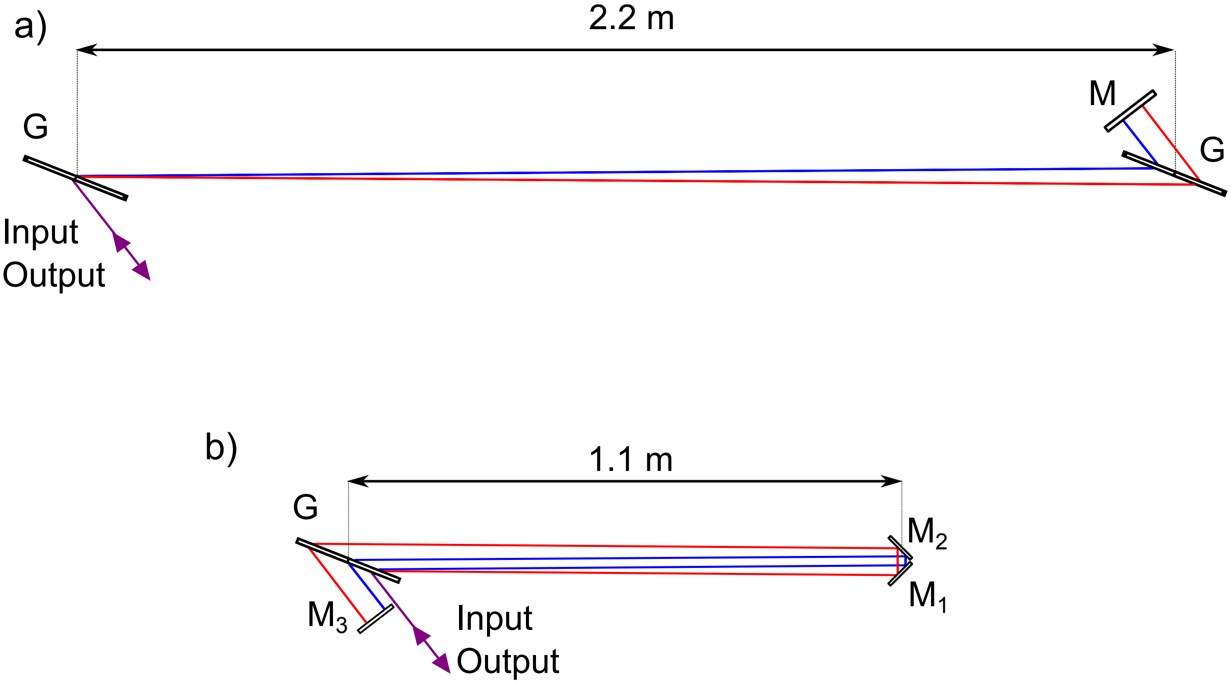

Figure 3.10: a) Compressor design with two gratings (top-view). G – transmission refraction grating, 1740 lines/mm, CMN Optics, Jena IOF; M – dielectric end-mirror, dimentions: 120 mm × 30 mm. Compressor supports 3 nm bandwidth. Red and the blue lines mark the longest and the shortest wavelengths of the supported spectral bandwidth. Size of optics and distances are in scale; b) Compressor design with a single grating (top-view). M_{1-3} – dielectric mirrors; M_{1-2} dimensions: 60 mm × 30 mm; M_3 dimensions: 80 mm × 30 mm. Size of optics and distances are in scale.

photo of the realization of the SSFS, the stretcher and the compressor is shown in Fig. 3.11.

Additionally, a 50 dB gain amplifier was necessary to reach the average power of 5 W required for the Innoslab seeding, as specified in (i). Both an Yb regenerative amplifier and a fiber amplifier were considered. In Fig. 3.12 the output power of the regenerative amplifier versus pump power for different seed input powers is shown. Even with the lowest power of 20 mW, required average power can be easily reached.

3.4 Yb front-end

The development of a broadband seed generation from a narrowband Yb amplifier led to a change of concept from a Ti:Sapphire front-end OPCPA to a Yb front-end OPCPA.

The pump laser system is significantly easier with a Yb master oscillator. The setup of the realized pump laser (in scale) is shown in Fig. 3.13. The Ti:Sapphire amplifier together with the setup of the soliton self-frequency shifting and the fiber pre-amplifier was replaced

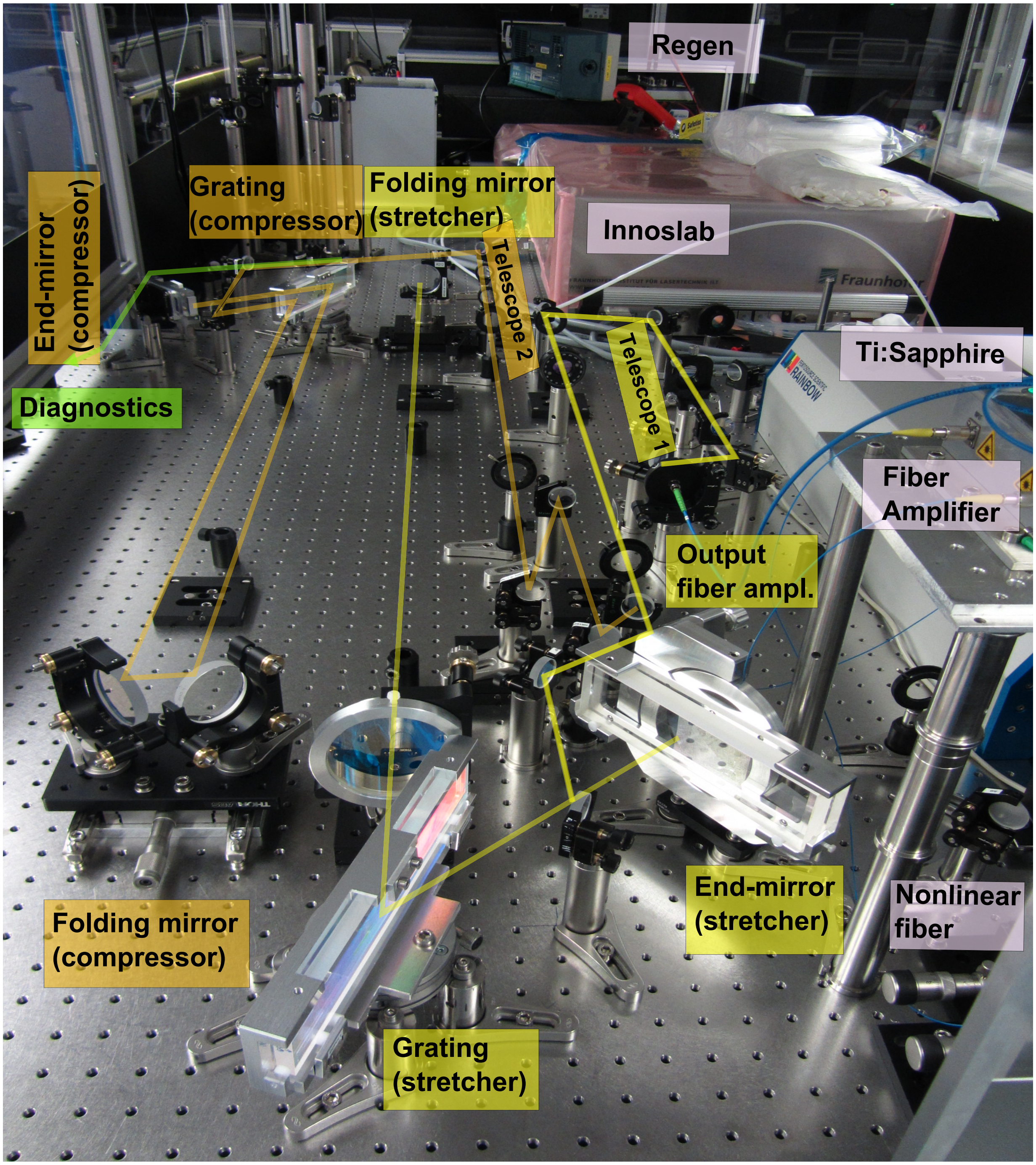

Figure 3.11: Photo of stretcher and compressor together with Ti:Sapphire oscillator, Innoslab and regenerative amplifiers.

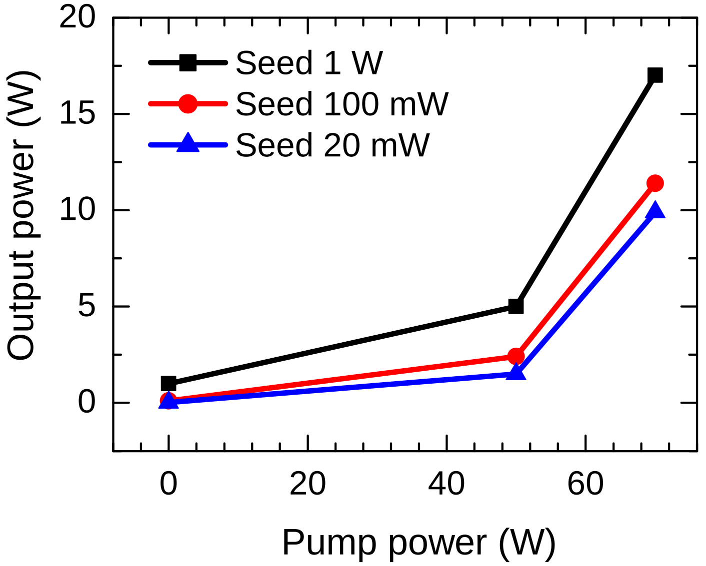

Figure 3.12: Regenerative amplifier output power versus pump power for different seed input powers.

by a fiber oscillator (Active fiber systems) emitting 1 ps pulses of an average power of 100 mW at 77 MHz repetition rate. The stretcher and the compressor were the same as in the Ti:Sapphire front-end setup, because a similar amount of the GDD was applied to stretch pulses for the Innoslab amplifier. After the stretcher (described in subsection 3.3.1), pulses were amplified in the fiber amplifier with an integrated pre-amplifier and a pulse picker (Active fiber systems). The average power after the fiber amplification was 10 W at a 100 kHz repetition rate. The output was used to seed the Innoslab amplifier. The output of the Innoslab amplifier was sent into the compressor described in details in subsection 3.3.2. The total output of the pump laser after the compressor was 4 mJ at a 100 kHz with a 1 ps pulse duration.

A scheme of the Yb front-end OPCPA is shown in Fig. 3.14. The configuration is similar to the one described in [91, 160]. A part of the output was separated to generate a broadband seed by white light generation. An SHG of the fundamental was used for the OPCPA pump. The amplified broadband spectrum was compressed with a chirped mirror compressor. The IR pulses were then generated in a DFG process, by mixing the visible pulses with the fundamental 1030 nm pulses. The mid-IR pulses were characterized by a novel discrete dispersion scanning technique by which the spectral phase was determined as described in [45]. By the discrete dispersion scanning technique the smoothness of the spectral phase was verified and the spectral phase was quantitatively defined for the design of the chirped mirror compressor.

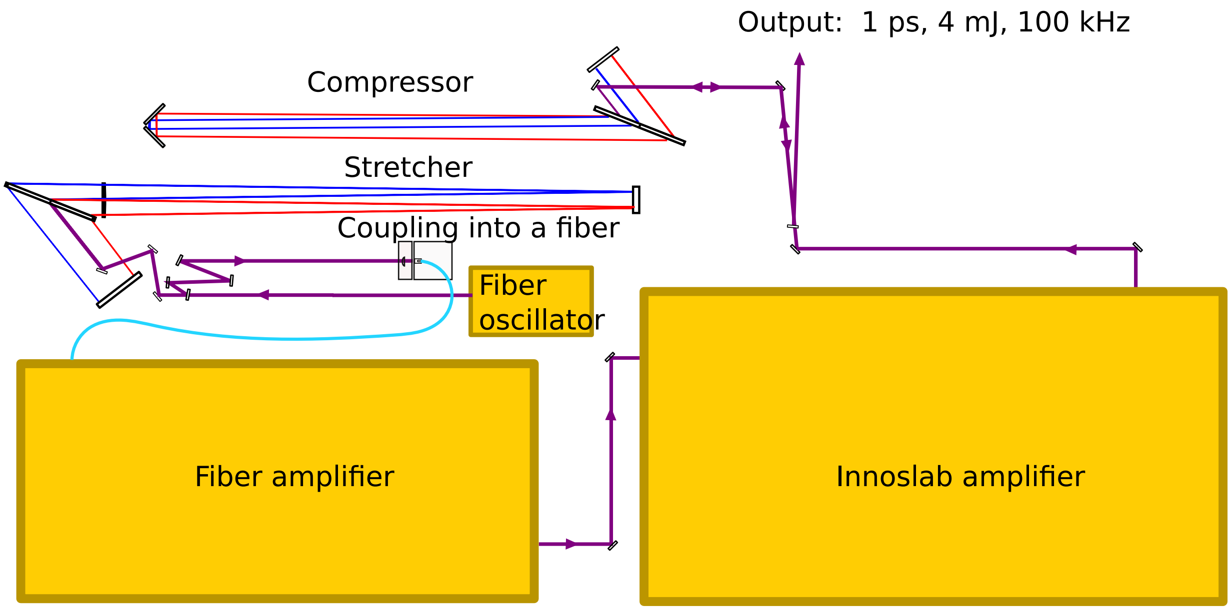

Figure 3.13: Setup of Yb front-end OPCPA pump laser.

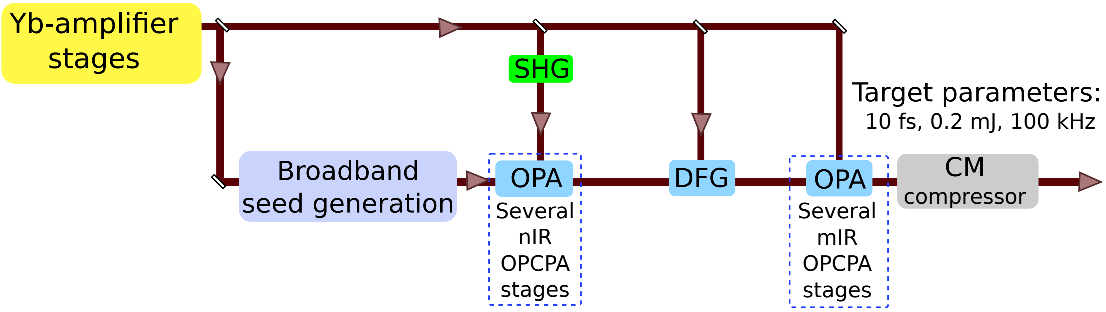

Figure 3.14: Setup of an Yb front-end OPCPA system.

The realization of the Yb front-end OPCPA lies within the scope of the PhD work of Harald Fuest and is described in detail in his thesis.

3.5 Summary and conclusions

The aim of the project discussed in this chapter was to develop a pump for a broadband OPCPA supporting few cycle CEP-stable pulses with a central wavelength of about 2 μm and a repetition rate of 100 kHz. The target parameters of the high power OPCPA pump laser were: 4 mJ pulse energy at 100 kHz repetition rate and 400 W average power. The laser source consisted of different types of high power Yb amplifiers: fiber and Innoslab. The seed for the Innoslab amplifier was required to several conditions regarding the average power, central wavelength, and pulse duration.

A Ti:sapphire laser was used as a master oscillator, however, the output power and the mode at 1030 nm and 4 nm FWHM bandwidth was insufficient for the direct seeding of the Yb fiber pre-amplifier. Soliton self-frequency shifting (SSFS) [86] was employed in a highly-nonlinear photonic-crystal-fiber (HNLF) to obtain higher pulse energy and a better mode profile to seed the pump chain using 5 % of the total Ti:Sapphire output. The output power within 4 nm bandwidth (FWHM) centered at 1030 nm was two times higher than the power directly available from the Ti:Sapphire oscillator. In addition, the mode profile was excellent, as one can expect from a fiber output. Coupling into the HNLF was perfectly stable within an explicit measured period of 8 hours without any active stabilization. The output of the HNLF was amplified in a fiber pre-amplifier characterized by 22 dB gain. The pre-amplified pulses were stretched then to 500 ps per 1.5 nm bandwidth in a grating stretcher to fulfill the requirements of the Innoslab amplifier. We have implemented a design of a stretcher and a compressor with a single grating, which was more compact than conventional two-grating stretchers and compressors. In addition, the alignment of the both components was significant easier, which simplified the whole setup of the pump laser. Amplification of 50 dB was necessary to reach the average power of 5 W required for the Innoslab seeding, a requirement that could be met by both a fiber and a regenerative amplifier.

Owing to the development of broadband seed generation from narrowband Yb amplifiers, the Ti:Sapphire front-end OPCPA was changed into an Yb front-end OPCPA. The advantage of an Yb front-end OPCPA is stable optical synchronization, meaning that no additional stabilization is required, and making an OPCPA system significantly simpler and easier to scale [89]. An output consisting of CEP-stable pulses at a central wavelength of about 2 μm was obtained by DFG between a broadband amplified seed and the rest of the narrowband fundamental at 1030 nm in a similar method to refs. [91, 160]. The resulting mid-IR pulses were characterized by the discrete dispersion scanning as described in [45].

Chapter 4

Extreme ultraviolet generation at 50 MHz repetition rate

In this chapter, the experiment of the harmonic generation at 50 MHz repetition is described. EUV radiation was generated by a frequency doubled (515 nm) high power (240 W) Yb:YAG Innoslab amplifier in a single-pass geometry, without the driving field enhancement in an enhancement cavity. We have used the second harmonic of the laser for the experiment, because the efficiency of the OHG depends on the wavelength of the driving field proportionally to $\lambda^{-6.5}$ [161, 162]. It has several advantages: the wavelength range of optical harmonics available from a single-pass geometry is not limited by the output coupling method. In addition, the same single-pass LHG setup works at different repetition rates without major modifications. Also, the CEP can be independently adjusted driving LHG with few-cycle pulses.

4.1 Setup and Results

A scheme of the experiment is shown in Fig. 4.1a. A passively mode-locked Yb:KGW oscillator (Amplitude Systèmes) was used to seed a Yb:YAG Innoslab amplifier. The oscillator delivered 300 fs pulses at a center wavelength of 1030 nm with an average power of 2 W at a 50 MHz repetition rate. The output of the Innoslab amplifier, with an average power of 500 W, was used to generate SHG delivering 600 fs pulses at a central wavelength of 515 nm with an average power of 250 W. The beam diameter was 2 mm at a $1/e^2$ intensity level. The pulse energy of the amplifier was 5 μJ. To reach a peak intensity of 10^{13} W/cm^2 level required for LHG, a beam was focused to a spot of 10 μm in diameter at a $1/e^2$ intensity level. In order to achieve the required focus size, we magnified the beam with a 1:3 telescope to a beam diameter of 6 mm ($1/e^2$ intensity level). The telescope lenses L_1 (focal length -168 mm) and L_2 (focal length +672 mm) are shown in Fig. 4.1. The lenses were made of fused silica glass because of its low thermal expansion coefficient. An attenuator made of a half-wave plate (HWP) and a thin-film-polarizer (Laser Components) was installed behind the telescope. The installation of an attenuator before the telescope

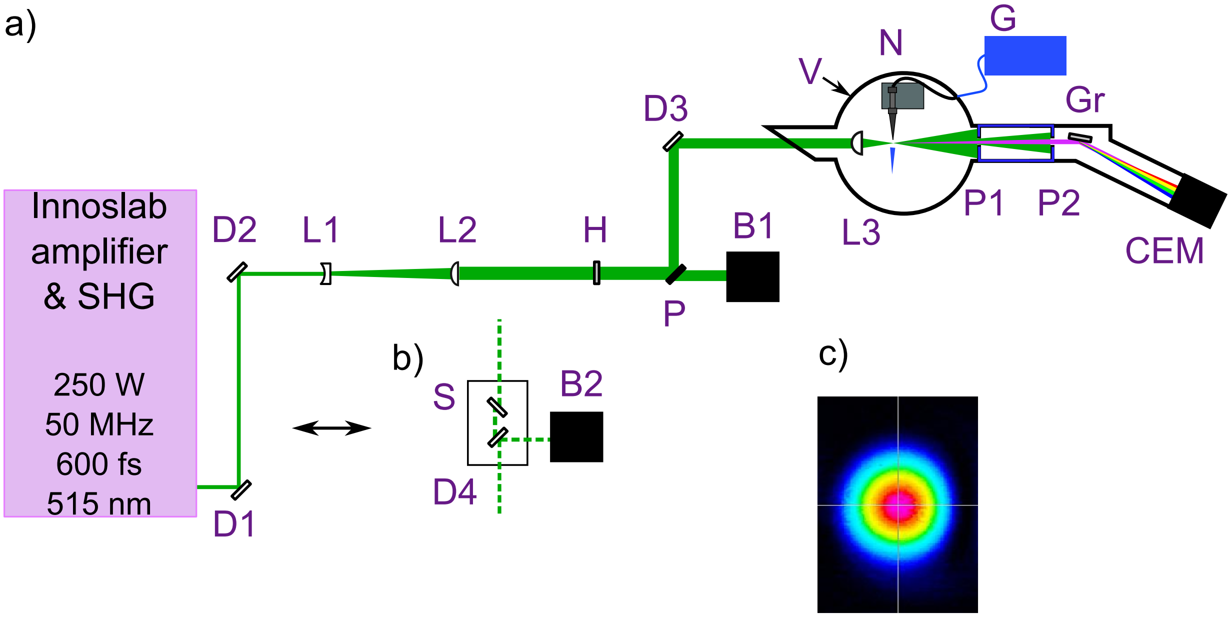

Figure 4.1: a) LHG setup. D_{1-4} – high reflective mirrors; L_{1-2} – telescope lenses; H – half-wave plate; P – thin film polarizer; B_{1-2} – beam blocks; L_3 – lens focusing into gas jet; N – nozzle; G – Xe gas supply; P_{1-2} – water-cooled pinholes blocking fundamental radiation; Gr – grating for EUV radiation; CEM – channel electron multiplier; b) Attenuator. S – fused silica substrate; c) Beam profile in focus.

failed, because of the degradation of the HWP due to high intensity of the laser beam. After removing the HWP from the setup and carrying out a visual inspection, a thin metal-like coating of the same size and the shape as the laser beam was observed. The coating was permanent and could not be removed by cleaning, as experienced in other experiments [163]. This degradation of the beam diameter of 2 mm at $1/e^2$ intensity level was observed only for the HWP, but not for dielectric mirrors and the telescope lenses. However, a similar degradation of an AR-coating was observed on a lens (focal length 30 mm, radius of curvature 13.6 mm, Laser Components), when attempting to focus a beam into a gas jet for the LHG experiment. The degradation was only on the one surface of the lens where the beam diameter was slightly smaller than 2 mm. A similar degradation of AR-coating was observed in an enhancement cavity in the visible [163]. One possible reason could be that residual organic compounds are dissociated by the intense laser radiation to form a carbon layer on the mirror surface. An established technique to restore the mirror reflectivity is a treatment with O_2 that chemically removes the carbon compounds [164, 165]. The degradation could be prevented completely by operating the enhancement cavity at 1.5 mbar of O_2 pressure. However, we observed the degradation not in a vacuum, but at normal air pressure. The pulse energy of the Innoslab laser was 4 times higher than the pulse energy circulating in the enhancement cavity [163]. The higher intensity of the laser beam compared with that in the enhancement cavity might be the main culprit. No degradation of optics was observed after the diameter of the beam was increased with the

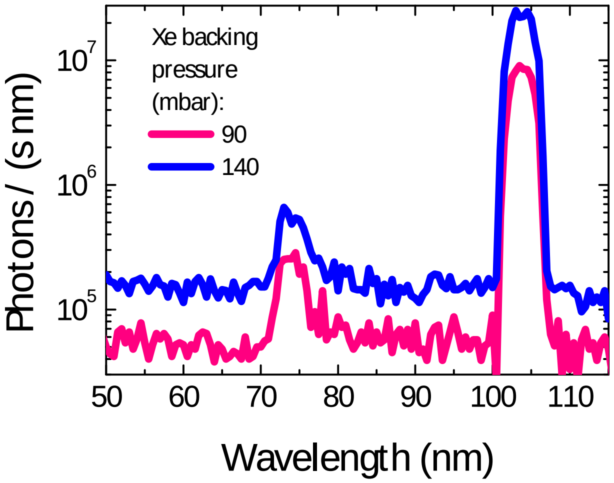

Figure 4.2: LHG spectra of 5^{th} and 7^{th} harmonic at different Xe gas backing pressures.

telescope to 6 mm.

The alignment of the beam through the setup was challending due to high average power. The position of the beam was slightly different at different output powers. An attenuator composed of a half-wave plate and a polarizer turned out to be a temporary solution, because of the mentioned degradation of the half-wave plate due to high average power. The half-wave plate turned to reflect increasingly higher amounts of the laser power. The pre-alignment was performed with an alignment laser at a center wavelength of 532 nm, so that the first elements of the setup (high-reflective mirrors and the beam blocks) could be placed. However, this alignment was not sensitive enough for the final alignment of the telescope. We have used a special attenuator composed of a high-reflective mirror (D_4) and a substrate of the same thickness (S) for the telescope alignment (Fig. 4.1b). The substrate corrected the change in the beam path, whereas the leakage after the mirror was used to align the optical system. Both components were fixed on a small breadboard. The attenuator was aligned precisely with the alignment laser. The alignment was reproducible after taking the breadboard in and out of the beam path.

We focused the beam with a plano-convex lens (radius of curvature 33.7 mm; focal length 73 mm) into a noble gas jet (Xe or Kr) inside a vacuum chamber. The beam profile in the focus is shown in Fig. 4.1c. The focus diameter was 10 μm. The measurement was performed with a CCD camera and 1:10 magnifying telescope (DataRay). The intensity in the focus was calculated as $2 \cdot 10^{13}$ W/cm^2. For the LHG experiment, the vacuum chamber was evacuated and a noble gas jet was produced in the vicinity of the focus by a glass nozzle (open diameter about 100 μm). The diameter of the nozzle was approximately the same as a Rayleigh length (150 μm) of the focus. The nozzle was placed on a motorized vacuum-compliant XYZ translation stage allowing a fine adjustment of the nozzle position. We also tried out a metal nozzle, but it heated up abruptly in the vicinity of the focus thus complicating the optimization of the alignment. Between the vacuum chamber and

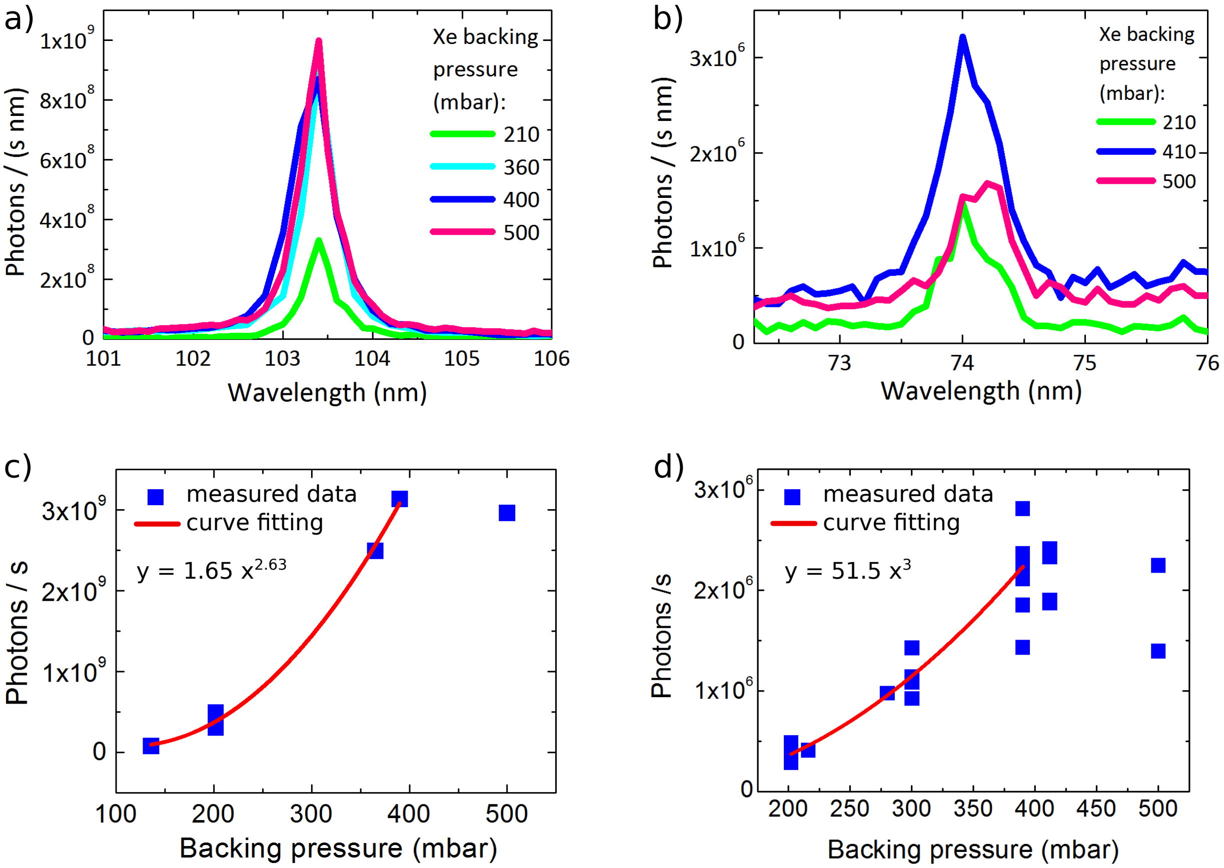

Figure 4.3: LHG spectra of 5^{th} (a) and 7^{th} (b) harmonic at different Xe gas backing pressures; Total flux versus backing pressure for 5^{th} (c) and 7^{th} (d) harmonic.

an EUV grating, two water-cooled pinholes of a diameter of 3 mm were mounted. The first pinhole was 210 mm away from the focus. Since the divergence of the harmonic radiation is smaller compared to the fundamental, the pinholes were used to reduce the power of the fundamental by a factor of 200. The pinholes were water-cooled due to high average power. The harmonic radiation propagated further into a differentially pumped grazing incidence EUV monochromator (McPherson 248/310) equipped with an EUV grating (133.6 grooves/mm) and a solar blind channel electron multiplier (channeltron). An adjustable micrometer slit in-front of the grating reduced the rest of the fundamental radiation to a minimum.

The resulting spectra of 5^{th} and 7^{th} harmonics are shown in Fig. 4.2 for two different Xe backing pressures (the pressure at the exhaust port). Photon number is calculated from the raw data taking into account divergence of the harmonics, pinholes, and the efficiency of the EUV detection. In the instrument data-sheet the efficiency was indicated as 10 % of the EUV grating and 10 % of the channeltron. The photon conversion efficiency was 10^{-13} and 10^{-14} for the 5^{th} and 7^{th} harmonic, respectively. We then optimized each of the harmonics separately and explored the flux dependence on the backing pressure

(Fig. 4.3). By altering the backing pressure, the number of emitters can be changed for the optimal phase matching conditions. The experimental result plotted on Fig. 4.3 was fitted using the function aP^b, where a and b were variable parameters, and P – backing pressure. The yield versus pressure of 5^{th} harmonic was fitted with parameters a = 1.65, b = 2.63 until the backing pressure of 390 mbar. The parameters of the fit of the 7^{th} harmonic were 51.5 and 3.00 respectively, until the backing pressure of 390 mbar. If the LHG process is perfectly phase matched, the harmonic emission should scale quadratically with the pressure [162, 166, 167]. When the backing pressure was greater than 390 mbar, the efficiency dropped, which might be due to ionization and reabsorption [162]. The quadratic dependence is well pronounced for the 5^{th} harmonic, however for the 7^{th} the dependence is almost linear, indicating that ionization and reabsorption play a significant role. In addition, the estimated value of the Keldysh parameter, $\gamma = 3.5$, supports the idea of the dominance of ionization.

In Table 4.1 a summary of the experimental results and their comparison with the LHG in the enhancement cavity of a similar central wavelength are given. We did not detect the 9^{th} harmonic, which might be due to the strong background induced by the ionization.

Table 4.1: Summary of LHG experiment and comparison with literature

Parameter	Enhancement cavity [163]	High power laser
Central wavelength (nm)	520	515
Repetition rate (MHz)	128	50
Power (W)	161	250
Peak power (MW)	7	7
Pulse duration (fs)	166	700
Fifth harmonic		
Power	4 μW	5 nW
Efficiency	10^{-8}	10^{-11}
Seventh harmonic		
Power	150 nW	20 pW
Efficiency	10^{-10}	10^{-14}
Ninth harmonic		
Power	5 nW	-
Efficiency	10^{-11}	-

4.2 Discussion

The 5^{th} harmonic coincides with the ionization potential of Xenon at 103 nm. However, the detection of the 7^{th} harmonic assures the observation of the 5^{th} harmonic rather than the line of a Xenon ionization. In addition, following [1], the observation of this line was impossible due to the strong ionization of such long input pulses.

The low efficiency of the process is not surprising, because the pulse duration of 600 fs was unfavorably long for LHG due to the ionization of the medium [19]. The Keldysh parameter γ was 3.5, indicating that the intensity of the driving field was too low. For efficient harmonic generation, the Keldysh parameter should be smaller than 1 [168]. The value of the Keldysh parameter also indicates that the multi-photon ionization was dominat over the tunnel ionization, which is the first step in the high harmonic generation process [169].

However, the experiment shows, that a state-of-the-art high-energy amplifier system without chirped pulse amplification can be utilized for the generation of extreme ultraviolet. The photon flux is rather low primarily due to long pulses of the driving field.

The experiment of an NPC with a solid core PCF (LMA-35) was unsuccessful, because the fiber got damaged at the average input power of 25 W (500 nJ pulse energy, 0.8 MW peak power). We used LMA-35 fibers with the end-caps lying in a water-cooled V-groove made from copper. With shorter input pulses (for example using gas filled kagomé fibers for the spectral broadening) direct high harmonic generation might become an alternative to high harmonic generation within an enhancement cavity, significantly simplifying the overall setup.

4.3 Summary and conclusions

In conclusion, harmonic-generation up to the 7^{th} order (74 nm) was observed using Xenon gas. To the best of our knowledge, this is the highest repetition rate for harmonics generation a in single-pass geometry. The estimated average power was 20 pW at 74 nm (17 eV) and 5 nW at 103 nm (12 eV). In Krypton gas the 5^{th} harmonic was detected, the estimated average power was 2 nW, and the photon conversion efficiency was 10^{-13} and 10^{-14} for the 5^{th} and 7^{th} harmonics, respectively.

In addition, the flux dependence on the backing pressure was explored. A pronounced quadratic dependence was observed for the 5^{th} harmonic, however, for the 7^{th} harmonic, the dependence was not quadratic, indicating a weak phase-matching. Furthermore, the estimated value of the Keldysh parameter, $\gamma = 3.5$, evidenced the dominance of the strong multi-photon ionization, which would significantly reduce the efficiency of the LHG. We could not detect the 9^{th} harmonic, which may be due to the strong background induced by the ionization.

The generated powers in extreme ultraviolet were not comparable to those produced by the cavity-assisted LHG. Nevertheless, the efficiency of single-pass LHG can be improved by using shorter driving pulses and specially designed gas targets together with quasi-phase-matching techniques [117, 118].

Chapter 5

Data Archiving

The experimental raw data, evaluation files, and original figures can be found on the Data Archive Server of the Laboratory for Attosecond Physics at the Max Planck Institute of Quantum Optics:
`/afs/rzg/mpq/lap/`
The list below contains paths to all the relevant files given with respect to the root folder of the thesis.

Figure 2.1
c) Fiber cross-section. d) Near-field image of the fiber end-facet. e) Mode in far-field.

▶ images	`chapter2_figures/50kHz/setup/microscope image LMA35.jpeg`
	`chapter2_figures/50kHz/setup/near field_after6days.bmp`
	`chapter2_figures/50kHz/setup/near field.bmp`

▶ Inkscape file	`chapter2_figures/50kHz/setup/setup.svg`
▶ plot	`chapter2_figures/50kHz/setup.pdf`

Figure 2.2
a) Transform-limited pulse duration of spectra with linear (LP) and circular (CP) polarization; b) Long-term stability of input, output, and transform-limited pulse duration of spectra. Peak power 3.6 MW; Fiber length 35 mm; LP.

▶ raw data	`chapter2_figures/50kHz/data/35mm_spectra raw` `chapter2_figures/50kHz/data/35mm_long-term-stability raw`
▶ LabVIEW	`chapter2_figures/50kHz/data/transform limit analysis`
▶ Origin file	`chapter2_figures/50kHz/data/fig3p2a.opj` `chapter2_figures/50kHz/data/fig3p2b.opj`
▶ plot	`chapter2_figures/50kHz/fiber35mm.pdf`

Figure 2.3
Long-term stability with different fiber lengths: 50 mm; 80 mm linear polarization (LP); 100 mm, LP and circular polarization (CP). Spectral broadening supports 66 fs.

▶ raw data `chapter2_figures/50kHz/data/fig3p3.opj`
▶ Origin file `chapter2_figures/50kHz/data/fig3p3.opj`
▶ plot `chapter2_figures/50kHz/fiber_length.pdf`

Figure 2.4

SHG FROG traces of compressed pulses: a) Measured and retrieved spectrograms, grid size 256x256; b) Measured and retrieved spectra, transform limit (TL), retrieved temporal intensity and temporal phase of shortest pulses.

▶ raw data `chapter2_figures/50kHz/data/frog`
▶ Origin file `chapter2_figures/50kHz/data/fig3p4.opj`
▶ plot `chapter2_figures/50kHz/frog.pdf`

Figure 2.5

Two-stage NPC in LMA PCF: a) Transform-limited pulse duration versus pulse energy in the fiber core for different fiber lengths; b) Spectra after the second stage with a 100 mm fiber and linear polarization at 0.4 μJ pulse energy in the fiber core (3 consequent measurements with a period of 1 s); c) Long-term stability of input, output and transform-limited pulse duration of spectra. Fiber length 100 mm, linear polarization.

▶ raw data `chapter2_figures/50kHz/2stage/different fiber lengths raw`
▶ Origin file `chapter2_figures/50kHz/2stage/different fiber lengths.opj`
`chapter2_figures/50kHz/2stage/spectra.opj`
`chapter2_figures/50kHz/2stage/stability.opj`
▶ plot `chapter2_figures/50kHz/2stage/spectra_stability.pdf`

Figure 2.6

a) Calculated spectrum and spectral phase after the second NPC stage with transform-limited input pulses (left hand side); Temporal intensity of transform-limited and compressed only by GDD compensation pulses (right hand side); b) Same as (a), but with chirped input pulses; c) Input temporal profiles used for the simulations: Black curve corresponds to the optimal 22 reflections on the chirped mirrors (used in simulations (a), blue curve – to 6 reflections (used in simulations (b).

▶ Origin file `chapter2_figures/50kHz/2stage/simulation results.opj`
`chapter2_figures/50kHz/2stage/temporal.opj`
▶ plot `chapter2_figures/50kHz/2stage/2stage.pdf`

Figure 2.7

b) Transform-limited pulse duration versus pulse energy in the fiber core for different fibers and fiber lengths.

▶ Origin file `chapter2_figures/11MHz/TL versus energy different rep rates.opj`
▶ plot `chapter2_figures/11MHz/setup.pdf`

Figure 2.8

Two nonlinear pulse compression stages. b) Spectrum after the second stage, transform-limit: 7 fs, pulse energy: 0.4 μJ; d) Spectrum after the crystal.

▶ raw data	`chapter2_figures/11MHz/2stage/wlg`
▶ Origin file	`chapter2_figures/11MHz/2stage/lma25.opj` `chapter2_figures/11MHz/2stage/wlg.opj`
▶ plot	`chapter2_figures/11MHz/2stage/2stage.pdf`

Figure 2.9

d) Coupled-mode of LMA-100 fiber in far-field; e) and f) Input (blue) and output (black) spectra with 75 mm fiber and 150 mm fiber, respectively. Coupled pulse energy 7 μJ (4 MW peak power) in both cases. Linear laser polarization. Transform-limited pulse duration: 85 fs and 60 fs, input pulse energy: 9 μJ and 10 μJ, respectively.

▶ raw data	`chapter2_figures/3kHz/spectra raw`
▶ plot	`chapter2_figures/3kHz/setup/setup.pdf`

Figure 2.10

b) Transform-limited pulse duration for different fiber lengths with linear and circular polarization. For comparison: Damage threshold of LMA-35 (red diamonds); LMA-35 with 1.1 ps input pulses at 50 kHz repetition rate, linear polarization (grey squares); c) Measured spectra, autocorrelation and transform-limited pulse intensity with LMA-100 fiber. Fiber length 120 mm, 47 W output power, circular polarization in the fiber.

▶ raw data	`chapter2_figures/20MHz/raw data`
▶ Origin file	`chapter2_figures/20MHz/TL with comparison.opj` `chapter2_figures/20MHz/100521AC.opj`
▶ plot	`chapter2_figures/3kHz/setup/setup.pdf`

Figure 2.12

Polarization extinction ratio (PER) versus pulse energy in the fiber core and transform-limited pulse duration of the spectra: a) LMA-35 fiber, 100 mm length, 1.1 ps input pulses at 50 kHz repetition rate; b) LMA-100 fiber, 150 mm length, 1.6 ps input pulses at 3 kHz repetition rate. Linear polarization.

▶ Origin file	`chapter2_figures/PER_3kHz_50kHz.opj`
▶ plot	`chapter2_figures/PER.pdf`

Figure 2.13

a) Spectra of SPM and FWM at 2.0 μJ and at 2.3 μJ output pulse energy; b) Long-term stability of input, output and transform-limit of the spectra. Fiber length 100 mm.

▶ raw data	`chapter2_figures/50kHz/data/red raw`
▶ Origin file	`chapter2_figures/50kHz/data/red stability.opj`
▶ plot	`chapter2_figures/50kHz/red.pdf`

Figure 3.4

b) Ti:sapphire spectrum (orange) in comparison with a spectrum after the highly-nonlinear fiber (blue) in a logarithmic scale; c) Soliton spectra measured after filters F_1 and F_2; d) Monitoring of coupling stability by measuring reflected spectra after filter F_2.

▶ raw data	`chapter3_figures/spectrumTiSa_NLF/data raw`
▶ Origin file	`chapter3_figures/spectrum_TiSa_NLF/spectrum_TiSa_NLF.opj`
	`chapter3_figures/soliton stability.opj`
▶ plot	`chapter3_figures/spectrum_TiSa_NLF.pdf`

Figure 3.5

a) Output spectrum of the fiber amplifier, total average power 100 mW; b) Autocorrelation of the output of the fiber amplifier, autocorrelation pulse duration 4.9 ps, pulse duration 3.5 ps.

▶ raw data	`chapter3_figures/Fiber Amplifier/data raw`
▶ Origin file	`chapter3_figures/Fiber Amplifier/Stretcher.opj`
	`chapter3_figures/Fiber Amplifier/FiberAmp_autocorrelation.opj`
▶ plot	`chapter3_figures/fiber_amplifier.pdf`

Figure 3.8

b) Theoretical refractive efficiency versus angle of incidence.

▶ raw data	`chapter3_figures/Grating/efficiency.txt`
▶ Origin file	`chapter3_figures/Grating/efficiency.opj`
▶ plot	`chapter3_figures/grating.pdf`

Figure 3.9

a) Pulse duration after stretcher, 2 nm FWHM for 6 nm spectral bandwidth FWHM; b) Photodiode response function; c) Input (blue) and output (black) spectra of the stretcher. Spectral power density is calibrated to the output power.

▶ raw data	`chapter3_figures/Stretcher/1ps_ultrafast_diode.dat`
	`chapter3_figures/Stretcher/Spectrum_stretcher/spectrum_stretcher_raw.txt`
▶ Origin file	`chapter3_figures/Stretcher/pulse_duration.opj`
	`chapter3_figures/Stretcher/Spectrum_stretcher/spectrum_stretcher.opj`
▶ plot	`chapter3_figures/stretcher_pulse.pdf`
	`chapter3_figures/1ps_diode.pdf`
	`chapter3_figures/stretcher_amp_cal.pdf`

Figure 3.11

Regenerative amplifier output power versus pump power for different seed input powers.

▶ Origin file	`chapter3_figures/seedRegen/seedRegen.opj`
▶ plot	`chapter3_figures/seedRegen.pdf`

Figure 4.2
LHG spectra of 5th and 7th harmonic at different Xe gas backing pressures.

▶ raw data	`chapter4_figures/spectra/raw`
▶ Origin file	`chapter4_figures/spectra.opj`
▶ Math. script	`chapter4_figures/spectra/efficiency estimation`
▶ plot	`chapter4_figures/spectra1.pdf`

Figure 4.3
LHG spectra of 5th (a) and 7th (b) harmonic at different Xe gas backing pressures; Total flux versus backing pressure for 5th (c) and 7th (d) harmonic.

▶ raw data	`chapter4_figures/spectra/raw`
▶ Origin file	`chapter4_figures/spectra.opj`
▶ Math. script	`chapter4_figures/spectra/efficiency estimation`
▶ plot	`chapter4_figures/spectra2.pdf`

Bibliography

[1] C. Gohle, T. Udem, M. Herrmann, J. Rauschenberger, R. Holzwarth, H. A. Schuessler, F. Krausz, and T. W. Hänsch, “A frequency comb in the extreme ultraviolet,” *Nature*, vol. 436, no. 7048, pp. 234–237, 2005.

[2] H. Carstens, M. Högner, T. Saule, S. Holzberger, N. Lilienfein, A. Guggenmos, C. Jocher, T. Eidam, D. Esser, V. Tosa, *et al.*, “High-harmonic generation at 250 MHz with photon energies exceeding 100 eV,” *Optica*, vol. 3, no. 4, pp. 366–369, 2016.

[3] A. Vernaleken, J. Weitenberg, T. Sartorius, P. Russbueldt, W. Schneider, S. L. Stebbings, M. F. Kling, P. Hommelhoff, H.-D. Hoffmann, R. Poprawe, F. Krausz, T. W. Hänsch, and T. Udem, “Single-pass high-harmonic generation at 20.8 MHz repetition rate,” *Opt. Lett.*, vol. 36, no. 17, pp. 3428–3430.

[4] S. Hädrich, M. Krebs, A. Hoffmann, A. Klenke, J. Rothhardt, J. Limpert, and A. Tünnermann, “Direct and efficient high harmonic generation at 10 MHz repetition rate,” in *The European Conference on Lasers and Electro-Optics*, p. CG_2_5, Optical Society of America, 2015.

[5] D. Schulz-Ertner, A. Nikoghosyan, B. Didinger, M. Münter, O. Jäkel, C. P. Karger, and J. Debus, “Therapy strategies for locally advanced adenoid cystic carcinomas using modern radiation therapy techniques,” *Cancer*, vol. 104, no. 2, pp. 338–344, 2005.

[6] D. Schulz-Ertner, C. P. Karger, A. Feuerhake, A. Nikoghosyan, S. E. Combs, O. Jäkel, L. Edler, M. Scholz, and J. Debus, “Effectiveness of carbon ion radiotherapy in the treatment of skull-base chordomas,” *Int. J. Radiat. Oncol. Biol. Phys.*, vol. 68, no. 2, pp. 449–457, 2007.

[7] R. R. Allison, R. M. Patel, and R. A. McLawhorn, “Radiation oncology: physics advances that minimize morbidity,” *Future Oncol.*, vol. 10, no. 15, pp. 2329–2344, 2014.

[8] H. N. Chapman, P. Fromme, A. Barty, T. A. White, R. A. Kirian, A. Aquila, M. S. Hunter, J. Schulz, D. P. DePonte, U. Weierstall, *et al.*, “Femtosecond X-ray protein nanocrystallography,” *Nature*, vol. 470, no. 7332, pp. 73–77, 2011.

[9] M. M. Seibert, T. Ekeberg, F. R. Maia, M. Svenda, J. Andreasson, O. Jönsson, D. Odić, B. Iwan, A. Rocker, D. Westphal, *et al.*, “Single mimivirus particles intercepted and imaged with an X-ray laser,” *Nature*, vol. 470, no. 7332, pp. 78–81, 2011.

[10] J. Küpper, S. Stern, L. Holmegaard, F. Filsinger, A. Rouzée, A. Rudenko, P. Johnsson, A. V. Martin, M. Adolph, A. Aquila, S. c. v. Bajt, A. Barty, C. Bostedt, J. Bozek, C. Caleman, R. Coffee, N. Coppola, T. Delmas, S. Epp, B. Erk, L. Foucar, T. Gorkhover, L. Gumprecht, A. Hartmann, R. Hartmann, G. Hauser, P. Holl, A. Hömke, N. Kimmel, F. Krasniqi, K.-U. Kühnel, J. Maurer, M. Messerschmidt, R. Moshammer, C. Reich, B. Rudek, R. Santra, I. Schlichting, C. Schmidt, S. Schorb, J. Schulz, H. Soltau, H. Spence, John C. D. Starodub, L. Strüder, J. Thøgersen, J. Vrakking, Marc J. G. Weidenspointner, T. A. White, C. Wunderer, G. Meijer, J. Ullrich, H. Stapelfeldt, D. Rolles, and H. N. Chapman, "X-ray diffraction from isolated and strongly aligned gas-phase molecules with a free-electron laser," *Phys. Rev. Lett.*, vol. 112, p. 083002, 2014.

[11] M. B. Luu, G. A. van Riessen, B. Abbey, M. W. M. Jones, N. W. Phillips, K. Elgass, M. D. Junker, D. J. Vine, I. McNulty, G. Cadenazzi, C. Millet, L. Tilley, K. A. Nugent, and A. G. Peele, "Fresnel coherent diffractive imaging tomography of whole cells in capillaries," *New J. Phys.*, vol. 16, no. 9, p. 093012, 2014.

[12] J. Messinger, W. Lubitz, and J.-R. Shen, "Photosynthesis: from natural to artificial," *Physical Chemistry Chemical Physics*, vol. 16, no. 24, pp. 11810–11811, 2014.

[13] CMS Collaboration, "Observation of a new boson at a mass of 125 GeV with the CMS experiment at the LHC," *Phys. Lett.*, vol. 716, p. 30, 2012.

[14] Collaboration ATLAS, "Observation of a new particle in the search for the standard model Higgs boson with the ATLAS detector at the LHC," *Phys. Lett.*, vol. 716, p. 1, 2012.

[15] L. Xu, T. W. Hänsch, C. Spielmann, A. Poppe, T. Brabec, and F. Krausz, "Route to phase control of ultrashort light pulses," *Opt. Lett.*, vol. 21, no. 24, pp. 2008–2010, 1996.

[16] T. Wittmann, B. Horvath, W. Helml, M. G. Schatzel, X. Gu, A. L. Cavalieri, G. G. Paulus, and R. Kienberger, "Single-shot carrier-envelope phase measurement of few-cycle laser pulses," *Nat. Phys.*, vol. 5, pp. 357–362, 2012.

[17] C. Spielmann, N. H. Burnett, S. Sartania, R. Koppitsch, M. Schnrer, C. Kan, M. Lenzner, P. Wobrauschek, and F. Krausz, "Generation of coherent X-rays in the water window using 5-femtosecond laser pulses," *Science*, vol. 278, no. 5338, pp. 661–664, 1997.

[18] Z. Chang, A. Rundquist, H. Wang, M. M. Murnane, and H. C. Kapteyn, "Generation of coherent soft X-rays at 2.7 nm using high harmonics," *Phys. Rev. Lett.*, vol. 79, pp. 2967–2970, 1997.

[19] T. Brabec and F. Krausz, "Intense few-cycle laser fields: Frontiers of nonlinear optics," *Rev. Mod. Phys.*, vol. 72, pp. 545–591, 2000.

[20] K. Zhao, Q. Zhang, M. Chini, Y. Wu, X. Wang, and Z. Chang, "Tailoring a 67 attosecond pulse through advantageous phase-mismatch," *Opt. Lett.*, vol. 37, no. 18, pp. 3891–3893, 2012.

[21] M. Hentschel, R. Kienbergerlink, C. Spielmann, G. A. Reider, N. Milosevic, T. Brabec, P. Corkum, U. Heinzmann, M. Drescher, and F. Krausz, "Attosecond metrology," *Nature*, vol. 414, pp. 509–513, 2001.

[22] A. Baltuska, T. Udem, M. Uiberacker, M. Hentschel, E. Goulielmakis, C. Gohle, R. Holzwarth, V. S. Yakovlev, A. Scrinzi, T. W. Hansch, and F. Krausz, "Attosecond control of electronic processes by intense light fields," *Nature*, vol. 421, pp. 611–615, 2003.

[23] B. Bergues, M. Kübel, N. G. Johnson, B. Fischer, N. Camus, K. J. Betsch, O. Herrwerth, A. Senftleben, A. M. Sayler, T. Rathje, *et al.*, "Attosecond tracing of correlated electron-emission in non-sequential double ionization," *Nat. Commun.*, vol. 3, p. 813, 2012.

[24] F. Süßmann, S. Zherebtsov, J. Plenge, N. G. Johnson, M. Kübel, A. Sayler, V. Mondes, C. Graf, E. Rühl, G. Paulus, *et al.*, "Single-shot velocity-map imaging of attosecond light-field control at kilohertz rate," *Rev. Sci. Instrum.*, vol. 82, no. 9, p. 093109, 2011.

[25] P. Corkum and F. Krausz, "Attosecond science," *Nat. Phys.*, vol. 3, no. 6, pp. 381–387, 2007.

[26] T. Tajima and J. M. Dawson, "Laser electron accelerator," *Phys. Rev. Lett.*, vol. 43, pp. 267–270, 1979.

[27] K. Nakajima, T. Kawakubo, H. Nakanishi, A. Ogata, Y. Kato, Y. Kitagawa, R. Kodama, K. Mima, H. Shiraga, K. Suzuki, T. Zhang, Y. Sakawa, T. Shoji, Y. Nishida, N. Yugami, M. Downer, D. Fisher, B. Newberger, and T. Tajima, "A proof-of-principle experiment of laser wakefield acceleration," *Physica Scripta*, vol. 1994, no. T52, p. 61, 1994.

[28] T. Fujii, Y. Oishi, T. Nayuki, Y. Takizawa, K. Nemoto, T. Kayoiji, K. Horioka, Y. Okano, Y. Hironaka, K. G. Nakamura, and K.-i. Kondo, "MeV-order proton and carbon ion acceleration by irradiation of 60 fs TW laser pulses on thin copper tape," *Appl. Phys. Lett.*, vol. 83, no. 8, 2003.

[29] A. M. March, A. Stickrath, G. Doumy, E. P. Kanter, B. Krässig, S. H. Southworth, K. Attenkofer, C. A. Kurtz, L. X. Chen, and L. Young, "Development of high-repetition-rate laser synchrotron facilities," *Rev. Sci. Instrum.*, vol. 82, no. 7, p. 073110, 2011.

[30] M. Herrmann, M. Haas, U. D. Jentschura, F. Kottmann, D. Leibfried, G. Saathoff, C. Gohle, A. Ozawa, V. Batteiger, S. Knünz, N. Kolachevsky, H. A. Schüssler, T. W. Hänsch, and T. Udem, "Feasibility of coherent XUV spectroscopy on the 1S-2S transition in singly ionized helium," *Phys. Rev. A*, vol. 79, p. 052505, 2009.

[31] T. Udem, R. Holzwarth, and T. W. Hansch, "Optical frequency metrology," *Nature*, vol. 416, pp. 233–237, 2002.

[32] T. Hänsch, J. Alnis, P. Fendel, M. Fischer, C. Gohle, M. Herrmann, R. Holzwarth, N. Kolachevsky, T. Udem, and M. Zimmermann, "Precision spectroscopy of hydrogen and femtosecond laser frequency combs," *Phil. Trans. A*, vol. 363, no. 1834, pp. 2155–2163, 2005.

[33] E. Peik and C. Tamm, "Nuclear laser spectroscopy of the 3.5 eV transition in Th-229," *EPL (Europhysics Letters)*, vol. 61, no. 2, p. 181, 2003.

[34] S. Chew, F. Süßmann, C. Späth, A. Wirth, J. Schmidt, S. Zherebtsov, A. Guggenmos, A. Oelsner, N. Weber, J. Kapaldo, *et al.*, "Time-of-flight-photoelectron emission microscopy on plasmonic structures using attosecond extreme ultraviolet pulses," *Appl. Phys. Lett.*, vol. 100, no. 5, p. 051904, 2012.

[35] J. C. Solem and G. C. Baldwin, "Microholography of living organisms," *Science*, vol. 218, no. 4569, pp. 229–235, 1982.

[36] X. Zhang, E. Schneider, G. Taft, H. Kapteyn, M. Murnane, and S. Backus, "Multi-microjoule, MHz repetition rate Ti:sapphire ultrafast regenerative amplifier system," *Opt. Express*, vol. 20, no. 7, pp. 7015–7021, 2012.

[37] P. Russbueldt, T. Mans, J. Weitenberg, H. Hoffmann, and R. Poprawe, "Compact diode-pumped 1.1 kW Yb:YAG Innoslab femtosecond amplifier," *Opt. Lett.*, vol. 35, no. 24, pp. 4169–4171, 2010.

[38] T. Eidam, S. Hanf, E. Seise, T. V. Andersen, T. Gabler, C. Wirth, T. Schreiber, J. Limpert, and A. Tünnermann, "Femtosecond fiber CPA system emitting 830 W average output power," *Opt. Lett.*, vol. 35, no. 2, pp. 94–96, 2010.

[39] J. Rothhardt, S. Demmler, S. Hädrich, T. Peschel, J. Limpert, and A. Tünnermann, "Thermal effects in high average power optical parametric amplifiers," *Opt. Lett.*, vol. 38, no. 5, pp. 763–765, 2013.

[40] R. Riedel, A. Stephanides, M. Prandolini, B. Gronloh, B. Jungbluth, T. Mans, and F. Tavella, "Power scaling of supercontinuum seeded megahertz-repetition rate optical parametric chirped pulse amplifiers," *Opt. Lett.*, vol. 39, no. 6, pp. 1422–1424, 2014.

[41] R. Riedel, J. Rothhardt, K. Beil, B. Gronloh, A. Klenke, H. Höppner, M. Schulz, U. Teubner, C. Kränkel, J. Limpert, A. Tünnermann, M. Prandolini, and F. Tavella, "Thermal properties of borate crystals for high power optical parametric chirped-pulse amplification," *Opt. Express*, vol. 22, no. 15, pp. 17607–17619, 2014.

[42] A. Schwarz, M. Ueffing, Y. Deng, X. Gu, H. Fattahi, T. Metzger, M. Ossiander, F. Krausz, and R. Kienberger, "Active stabilization for optically synchronized optical parametric chirped pulse amplification," *Opt. Express*, vol. 20, no. 5, pp. 5557–5565, 2012.

[43] P. Dombi, P. Rácz, L. Veisz, and P. Baum, "Conversion of chirp in fiber compression," *Opt. Lett.*, vol. 39, no. 8, pp. 2232–2235.

[44] L. Lötscher, L. Vámos, L. Veisz, and A. Apolonski, "Long-term stability of nonlinear pulse compression using solid-core large-mode-area fibers," *J. Lasers Opt. Photon.*, vol. 2, pp. 1–5, 2015.

[45] P. Wnuk, H. Fuest, M. Neuhaus, L. Lötscher, E. Riedle, Z. Major, P. Russbüldt, D. Hoffmann, F. Krausz, and M. F. Kling, "Discrete dispersion scanning as a simple method for broadband femtosecond pulse characterization," *Opt. Express*, vol. 24, pp. 18551–18558, 2016.

[46] L. P. Lötscher, W. Schneider, P. Rußbüldt, B. Gronloh, H. D. Hoffmann, M. F. Kling, and A. Apolonski, "Direct low-harmonic generation in gas at MHz repetition rate," in *Lasers and Electro-Optics Europe (CLEO EUROPE/IQEC), 2013 Conference on Lasers and Electro-Optics, International Quantum Electronics Conference*, IEEE, 2013.

[47] H. Nakatsuka, D. Grischkowsky, and A. C. Balant, "Nonlinear picosecond-pulse propagation through optical fibers with positive group velocity dispersion," *Phys. Rev. Lett.*, vol. 47, pp. 910–913, 1981.

[48] C. V. Shank, R. L. Fork, R. Yen, R. H. Stolen, and W. J. Tomlinson, "Compression of femtosecond optical pulses," *Appl. Phys. Lett.*, vol. 40, no. 9, 1982.

[49] B. Nikolaus and D. Grischkowsky, "90 fs tunable optical pulses obtained by two stage pulse compression," *Appl. Phys. Lett.*, vol. 43, no. 3, 1983.

[50] J. G. Fujimoto, A. M. Weiner, and E. P. Ippen, "Generation and measurement of optical pulses as short as 16 fs," *Appl. Phys. Lett.*, vol. 44, no. 9, 1984.

[51] J. M. Halbout and D. Grischkowsky, "12 fs ultrashort optical pulse compression at a high repetition rate," *Appl. Phys. Lett.*, vol. 45, no. 12, pp. 1281–1283, 1984.

[52] W. H. Knox, R. L. Fork, M. C. Downer, R. H. Stolen, C. V. Shank, and J. A. Valdmanis, "Optical pulse compression to 8 fs at a 5 kHz repetition rate," *Appl. Phys. Lett.*, vol. 46, no. 12, 1985.

[53] R. L. Fork, C. H. B. Cruz, P. C. Becker, and C. V. Shank, "Compression of optical pulses to six femtoseconds by using cubic phase compensation," *Opt. Lett.*, vol. 12, no. 7, pp. 483–485, 1987.

[54] A. Baltuska, Z. Wei, M. S. Pshenichnikov, and D. A. Wiersma, "Optical pulse compression to 5 fs at a 1-MHz repetition rate," *Opt. Lett.*, vol. 22, no. 2, pp. 102–104, 1997.

[55] M. Nisoli, S. Stagira, S. De Silvestri, O. Svelto, S. Sartania, Z. Cheng, M. Lenzner, C. Spielmann, and F. Krausz, "A novel-high energy pulse compression system: generation of multigigawatt sub-5-fs pulses," *Appl. Phys. B*, vol. 65, no. 2, pp. 189–196, 1997.

[56] V. Yakovlev, P. Dombi, G. Tempea, C. Lemell, J. Burgdörfer, T. Udem, and A. Apolonski, "Phase-stabilized 4-fs pulses at the full oscillator repetition rate for a photoemission experiment," *Appl. Phys. B*, vol. 76, no. 3, pp. 329–332, 2003.

[57] S. Demmler, J. Rothhardt, A. M. Heidt, A. Hartung, E. G. Rohwer, H. Bartelt, J. Limpert, and A. Tünnermann, "Generation of high quality, 1.3 cycle pulses by active phase control of an octave spanning supercontinuum," *Opt. Express*, vol. 19, no. 21, pp. 20151–20158, 2011.

[58] M. Nisoli, S. De Silvestri, and O. Svelto, “Generation of high energy 10 fs pulses by a new pulse compression technique,” *Appl. Phys. Lett.*, vol. 68, no. 20, 1996.

[59] G. P. Agrawal, *Nonlinear Fiber Optics.* Academic Press, 2012.

[60] T. Südmeyer, F. Brunner, E. Innerhofer, R. Paschotta, K. Furusawa, J. C. Baggett, T. M. Monro, D. J. Richardson, and U. Keller, “Nonlinear femtosecond pulse compression at high average power levels by use of a large-mode-area holey fiber,” *Opt. Lett.*, vol. 28, no. 20, pp. 1951–1953, 2003.

[61] C. Jocher, T. Eidam, S. Hädrich, J. Limpert, and A. Tünnermann, “Sub 25-fs pulses from solid-core nonlinear compression stage at 250 W of average power,” *Opt. Lett.*, vol. 37, no. 21, pp. 4407–4409, 2012.

[62] A. Klenke, M. Kienel, T. Eidam, S. Hädrich, J. Limpert, and A. Tünnermann, “Divided-pulse nonlinear compression,” *Opt. Lett.*, vol. 38, no. 22, pp. 4593–4596, 2013.

[63] O. H. Heckl, C. J. Saraceno, C. R. E. Baer, T. Südmeyer, Y. Y. Wang, Y. Cheng, F. Benabid, and U. Keller, “Temporal pulse compression in a xenon-filled Kagome-type hollow-core photonic crystal fiber at high average power,” *Opt. Express*, vol. 19, no. 20, pp. 19142–19149, 2011.

[64] F. Emaury, C. F. Dutin, C. J. Saraceno, M. Trant, O. H. Heckl, Y. Y. Wang, C. Schriber, F. Gerome, T. Südmeyer, F. Benabid, and U. Keller, “Beam delivery and pulse compression to sub-50 fs of a modelocked thin-disk laser in a gas-filled Kagome-type HC-PCF fiber,” *Opt. Express*, vol. 21, no. 4, pp. 4986–4994, 2013.

[65] K. Mak, M. Seidel, O. Pronin, M. Frosz, A. Abdolvand, V. Pervak, A. Apolonski, F. Krausz, J. Travers, and P. S. J. Russell, “Compressing μJ-level pulses from 250 fs to sub-10 fs at 38-MHz repetition rate using two gas-filled hollow-core photonic crystal fiber stages,” *Opt. Lett.*, vol. 40, no. 7, pp. 1238–1241, 2015.

[66] J. C. Travers, W. Chang, J. Nold, N. Y. Joly, and P. St J Russell, “Ultrafast nonlinear optics in gas-filled hollow-core photonic crystal fibers,” *J. Opt. Soc. Am. B*, vol. 28, no. 12, pp. 11–26, 2011.

[67] S. Hädrich, J. Rothhardt, T. Eidam, J. Limpert, and A. Tünnermann, “High energy ultrashort pulses via hollow fiber compression of a fiber chirped pulse amplification system,” *Opt. Express*, vol. 17, no. 5, pp. 3913–3922, 2009.

[68] S. Hädrich, H. Carstens, J. Rothhardt, J. Limpert, and A. Tünnermann, “Multi-gigawatt ultrashort pulses at high repetition rate and average power from two-stage nonlinear compression,” *Opt. Express*, vol. 19, no. 8, pp. 7546–7552, 2011.

[69] S. Hädrich, A. Klenke, A. Hoffmann, T. Eidam, T. Gottschall, J. Rothhardt, J. Limpert, and A. Tünnermann, “Nonlinear compression to sub-30-fs, 0.5 mJ pulses at 135 W of average power,” *Opt. Lett.*, vol. 38, no. 19, pp. 3866–3869, 2013.

[70] O. Pronin, M. Seidel, F. Lücking, J. Brons, E. Fedulova, M. Trubetskov, V. Pervak, A. Apolonski, T. Udem, and F. Krausz, "High-power multi-megahertz source of waveform-stabilized few-cycle light," *Nat. Commun.*, vol. 6, 2015.

[71] M. E. Fermann, M. L. Stock, M. J. Andrejco, and Y. Silberberg, "Passive mode locking by using nonlinear polarization evolution in a polarization-maintaining erbium-doped fiber," *Opt. Lett.*, vol. 18, no. 11, pp. 894–896, 1993.

[72] R. Paschotta, "The Encyclopedia of Laser Physics and Technology."

[73] I. H. Malitson, "Interspecimen comparison of the refractive index of fused silica," *J. Opt. Soc. Am.*, vol. 55, no. 10, pp. 1205–1208, 1965.

[74] "Refractive index database." http://refractiveindex.info/.

[75] D. Nodop, C. Jauregui, D. Schimpf, J. Limpert, and A. Tünnermann, "Efficient high-power generation of visible and mid-infrared light by degenerate four-wave-mixing in a large-mode-area photonic-crystal fiber," *Opt. Lett.*, vol. 34, no. 22, pp. 3499–3501, 2009.

[76] G. Genty, M. Lehtonen, and H. Ludvigsen, "Effect of cross-phase modulation on supercontinuum generated in microstructured fibers with sub-30 fs pulses," *Opt. Express*, vol. 12, no. 19, pp. 4614–4624, 2004.

[77] A. Dubietis, G. Jonusauskas, and A. Piskarskas, "Powerful femtosecond pulse generation by chirped and stretched pulse parametric amplification in {BBO} crystal," *Opt. Commun*, vol. 88, no. 46, pp. 437 – 440, 1992.

[78] I. Ross, P. Matousek, M. Towrie, A. Langley, and J. Collier, "The prospects for ultrashort pulse duration and ultrahigh intensity using optical parametric chirped pulse amplifiers," *Opt. Commun*, vol. 144, no. 13, pp. 125 – 133, 1997.

[79] I. N. Ross, P. Matousek, G. H. New, and K. Osvay, "Analysis and optimization of optical parametric chirped pulse amplification," *J. Opt. Soc. Am. B*, vol. 19, no. 12, pp. 2945–2956, 2002.

[80] F. Tavella, K. Schmid, N. Ishii, A. Marcinkevičius, L. Veisz, and F. Krausz, "High-dynamic range pulse-contrast measurements of a broadband optical parametric chirped-pulse amplifier," *Appl. Phys. B*, vol. 81, no. 6, pp. 753–756, 2005.

[81] T. Metzger, A. Schwarz, C. Y. Teisset, D. Sutter, A. Killi, R. Kienberger, and F. Krausz, "High-repetition-rate picosecond pump laser based on a Yb:YAG disk amplifier for optical parametric amplification," *Opt. Lett.*, vol. 34, no. 14, pp. 2123–2125, 2009.

[82] T. Fuji, J. Rauschenberger, A. Apolonski, V. S. Yakovlev, G. Tempea, T. Udem, C. Gohle, T. W. Hänsch, W. Lehnert, M. Scherer, *et al.*, "Monolithic carrier-envelope phase-stabilization scheme," *Opt. Lett.*, vol. 30, no. 3, pp. 332–334, 2005.

[83] C. Hauri, P. Schlup, G. Arisholm, J. Biegert, and U. Keller, "Phase-preserving chirped-pulse optical parametric amplification to 17.3 fs directly from a Ti:sapphire oscillator," *Opt. Lett.*, vol. 29, no. 12, pp. 1369–1371, 2004.

[84] R. T. Zinkstok, S. Witte, W. Hogervorst, and K. Eikema, “High-power parametric amplification of 11.8-fs laser pulses with carrier-envelope phase control,” *Opt. Lett.*, vol. 30, no. 1, pp. 78–80, 2005.

[85] J. Rothhardt, S. Demmler, S. Hädrich, J. Limpert, and A. Tünnermann, “Octave-spanning OPCPA system delivering CEP-stable few-cycle pulses and 22 W of average power at 1 MHz repetition rate,” *Opt. Express*, vol. 20, no. 10, pp. 10870–10878, 2012.

[86] C. Teisset, N. Ishii, T. Fuji, T. Metzger, S. Köhler, R. Holzwarth, A. Baltuška, A. Zheltikov, and F. Krausz, “Soliton-based pump-seed synchronization for few-cycle OPCPA,” *Opt. Express*, vol. 13, no. 17, pp. 6550–6557, 2005.

[87] J. Rothhardt, A. M. Heidt, S. Hädrich, S. Demmler, J. Limpert, and A. Tünnermann, “High stability soliton frequency-shifting mechanisms for laser synchronization applications,” *J. Opt. Soc. Am. B*, vol. 29, no. 6, pp. 1257–1262, 2012.

[88] M. Krebs, S. Hädrich, S. Demmler, J. Rothhardt, A. Zaïr, L. Chipperfield, J. Limpert, and A. Tünnermann, “Towards isolated attosecond pulses at megahertz repetition rates,” *Nature Photon.*, vol. 7, no. 7, pp. 555–559, 2013.

[89] R. Riedel, M. Schulz, M. Prandolini, A. Hage, H. Höppner, T. Gottschall, J. Limpert, M. Drescher, and F. Tavella, “Long-term stabilization of high power optical parametric chirped-pulse amplifiers,” *Opt. Express*, vol. 21, no. 23, pp. 28987–28999, 2013.

[90] M. Schulz, R. Riedel, A. Willner, T. Mans, C. Schnitzler, P. Russbueldt, J. Dolkemeyer, E. Seise, T. Gottschall, S. Hädrich, *et al.*, “Yb:YAG Innoslab amplifier: efficient high repetition rate subpicosecond pumping system for optical parametric chirped pulse amplification,” *Opt. Lett.*, vol. 36, no. 13, pp. 2456–2458, 2011.

[91] C. Homann, M. Bradler, M. Förster, P. Hommelhoff, and E. Riedle, “Carrier-envelope phase stable sub-two-cycle pulses tunable around 1.8 μm at 100 kHz,” *Opt. Lett.*, vol. 37, no. 10, pp. 1673–1675, 2012.

[92] M. Puppin, Y. Deng, O. Prochnow, J. Ahrens, T. Binhammer, U. Morgner, M. Krenz, M. Wolf, and R. Ernstorfer, “Tunable sub-20 fs pulses from a 500 kHz OPCPA with 15 W average power based on an all-ytterbium laser,” *arXiv preprint arXiv:1409.6642*, 2014.

[93] M. Bradler, P. Baum, and E. Riedle, “Femtosecond continuum generation in bulk laser host materials with sub-μJ pump pulses,” *Appl. Phys. B*, vol. 97, no. 3, pp. 561–574, 2009.

[94] N. Ishii, L. Turi, V. S. Yakovlev, T. Fuji, F. Krausz, A. Baltuska, R. Butkus, G. Veitas, V. Smilgevicius, R. Danielius, and A. Piskarskas, “Multimillijoule chirped parametric amplification of few-cycle pulses,” *Opt. Lett.*, vol. 30, no. 5, pp. 567–569, 2005.

[95] S. Koke, C. Grebing, H. Frei, A. Anderson, A. Assion, and G. Steinmeyer, “Direct frequency comb synthesis with arbitrary offset and shot-noise-limited phase noise,” *Nature Photon.*, vol. 4, no. 7, pp. 462–465, 2010.

[96] F. Lücking, A. Assion, A. Apolonski, F. Krausz, and G. Steinmeyer, “Long-term carrier-envelope-phase-stable few-cycle pulses by use of the feed-forward method,” *Opt. Lett.*, vol. 37, no. 11, pp. 2076–2078, 2012.

[97] C. Manzoni, G. Cerullo, and S. De Silvestri, “Ultrabroadband self-phase-stabilized pulses by difference-frequency generation,” *Opt. Lett.*, vol. 29, no. 22, pp. 2668–2670, 2004.

[98] G. Cerullo, A. Baltuška, O. D. Mücke, and C. Vozzi, “Few-optical-cycle light pulses with passive carrier-envelope phase stabilization,” *Laser Photon. Rev.*, vol. 5, no. 3, pp. 323–351, 2011.

[99] P. Rußbüldt, J. Weitenberg, T. Sartorius, G. Rotarius, H. Hoffmann, and R. Poprawe, “Ytterbium innoslab amplifiers – the high average power approach of ultrafast lasers,” in *LIGHT AT EXTREME INTENSITIES 2011*, vol. 1462, pp. 120–123, AIP Publishing, 2012.

[100] J. Limpert, N. Deguil-Robin, I. Manek-Hönninger, F. Salin, F. Röser, A. Liem, T. Schreiber, S. Nolte, H. Zellmer, A. Tünnermann, *et al.*, “High-power rod-type photonic crystal fiber laser,” *Opt. Express*, vol. 13, no. 4, pp. 1055–1058, 2005.

[101] A. Galvanauskas, M.-Y. Cheng, K.-C. Hou, and K.-H. Liao, “High peak power pulse amplification in large-core yb-doped fiber amplifiers,” *Selected Topics in IEEE J. Quant. Electron.*, vol. 13, no. 3, pp. 559–566, 2007.

[102] F. Jansen, F. Stutzki, H.-J. Otto, M. Baumgartl, C. Jauregui, J. Limpert, and A. Tünnermann, “The influence of index-depressions in core-pumped Yb-doped large pitch fibers,” *Opt. Express*, vol. 18, no. 26, pp. 26834–26842, 2010.

[103] R. Paschotta, J. Nilsson, A. C. Tropper, and D. C. Hanna, “Ytterbium-doped fibre amplifiers,” *IEEE J. Quant. Electron.*, vol. 33, no. 7, pp. 1049–1056, 1997.

[104] A. V. Smith, B. T. Do, G. R. Hadley, and R. L. Farrow, “Optical damage limits to pulse energy from fibers,” *IEEE J. Sel. Top. Quantum Electron*, vol. 15, no. 1, pp. 153–158, 2009.

[105] T. Eidam, J. Rothhardt, F. Stutzki, F. Jansen, S. Hädrich, H. Carstens, C. Jauregui, J. Limpert, and A. Tünnermann, “Fiber chirped-pulse amplification system emitting 3.8 GW peak power,” *Opt. Express*, vol. 19, no. 1, pp. 255–260, 2011.

[106] C. J. Saraceno, C. Schriber, F. Emaury, O. H. Heckl, C. R. Baer, M. Hoffmann, K. Beil, C. Kränkel, M. Golling, T. Südmeyer, *et al.*, “Cutting-edge high-power ultrafast thin disk oscillators,” *Appl. Sci.*, vol. 3, no. 2, pp. 355–395, 2013.

[107] O. Pronin, J. Brons, C. Grasse, V. Pervak, G. Boehm, M.-C. Amann, A. Apolonski, V. Kalashnikov, and F. Krausz, “High-power Kerr-lens mode-locked Yb:YAG thin-disk oscillator in the positive dispersion regime,” *Opt. Lett.*, vol. 37, no. 17, pp. 3543–3545, 2012.

[108] J. Brons, V. Pervak, E. Fedulova, D. Bauer, D. Sutter, V. Kalashnikov, A. Apolonskiy, O. Pronin, and F. Krausz, “Energy scaling of kerr-lens mode-locked thin-disk oscillators,” *Opt. Lett.*, vol. 39, no. 22, pp. 6442–6445, 2014.

[109] J.-P. Negel, A. Voss, M. A. Ahmed, D. Bauer, D. Sutter, A. Killi, and T. Graf, “1.1 kW average output power from a thin-disk multipass amplifier for ultrashort laser pulses,” *Opt. Lett.*, vol. 38, no. 24, pp. 5442–5445, 2013.

[110] W. Koechner, *Solid-State Laser Engineering.* Springer, 5 ed., 1999.

[111] W. Schneider, A. Ryabov, C. Lombosi, T. Metzger, Z. Major, J. Fülöp, and P. Baum, “800-fs, 330-μJ pulses from a 100-W regenerative Yb: YAG thin-disk amplifier at 300 kHz and THz generation in LiNbO3,” *Opt. Lett.*, vol. 39, no. 23, pp. 6604–6607, 2014.

[112] P. Russbueldt, T. Mans, G. Rotarius, J. Weitenberg, H. Hoffmann, and R. Poprawe, “400W Yb:YAG Innoslab fs-amplifier,” *Opt. Express*, vol. 17, no. 15, pp. 12230–12245, 2009.

[113] F. Brandi, *Table-top tunable narrow-band extreme-ultraviolet sources: from low to high-order optical harmonic generation.* PhD thesis, University of Amsterdam, 2004.

[114] J. Reintjes, *Nonlinear optical parametric processes in liquids and gases.* Elsevier, 2012.

[115] H. Tsuchida, “Pulse timing stabilization of a mode-locked Cr:LiSAF laser,” *Opt. Lett.*, vol. 24, no. 22, pp. 1641–1643, 1999.

[116] A. Vernaleken, J. Weitenberg, T. Sartorius, P. Russbueldt, W. Schneider, S. L. Stebbings, M. F. Kling, P. Hommelhoff, H.-D. Hoffmann, R. Poprawe, *et al.*, “Single-pass high-harmonic generation at 20.8 MHz repetition rate,” *Opt. Lett.*, vol. 36, no. 17, pp. 3428–3430, 2011.

[117] E. A. Gibson, A. Paul, N. Wagner, D. Gaudiosi, S. Backus, I. P. Christov, A. Aquila, E. M. Gullikson, D. T. Attwood, M. M. Murnane, *et al.*, “Coherent soft x-ray generation in the water window with quasi-phase matching,” *Science*, vol. 302, no. 5642, pp. 95–98, 2003.

[118] A. Paul, R. Bartels, R. Tobey, H. Green, S. Weiman, I. Christov, M. Murnane, H. Kapteyn, and S. Backus, “Quasi-phase-matched generation of coherent extreme-ultraviolet light,” *Nature*, vol. 421, no. 6918, pp. 51–54, 2003.

[119] X. Zhang, A. L. Lytle, T. Popmintchev, X. Zhou, H. C. Kapteyn, M. M. Murnane, and O. Cohen, “Quasi-phase-matching and quantum-path control of high-harmonic generation using counterpropagating light,” *Nat. Phys.*, vol. 3, no. 4, pp. 270–275, 2007.

[120] C. Y. Teisset, *Few-Cycle High-Repetition-Rate Optical Parametric Amplifiers And Their Synchronisation Schemes.* PhD thesis, Technical University of Berlin, 2009.

[121] V. A. Lobastov, R. Srinivasan, and A. H. Zewail, “Four-dimensional ultrafast electron microscopy,” *Proc. Natl. Acad. Sci. USA*, vol. 102, no. 20, pp. 7069–7073, 2005.

[122] A. H. Zewail, “Four-dimensional electron microscopy,” *Science*, vol. 328, no. 5975, pp. 187–193, 2010.

[123] M. Aidelsburger, F. O. Kirchner, F. Krausz, and P. Baum, “Single-electron pulses for ultrafast diffraction,” *Proc. Natl. Acad. Sci. USA*, vol. 107, no. 46, pp. 19714–19719, 2010.

[124] F. Kirchner, A. Gliserin, F. Krausz, and P. Baum, “Laser streaking of free electrons at 25 keV,” *Nature Photon.*, vol. 8, no. 1, pp. 52–57, 2014.

[125] J. Hebling, K.-L. Yeh, M. C. Hoffmann, and K. A. Nelson, “High-power THz generation, THz nonlinear optics, and THz nonlinear spectroscopy,” *IEEE J. Sel. Top. Quantum Electron*, vol. 14, no. 2, pp. 345–353, 2008.

[126] H. Hirori and K. Tanaka, “Nonlinear optical phenomena induced by intense single-cycle terahertz pulses,” *IEEE J. Sel. Top. Quantum Electron*, vol. 19, no. 1, pp. 8401110–8401110, 2013.

[127] E. Fill, L. Veisz, A. Apolonski, and F. Krausz, “Sub-fs electron pulses for ultrafast electron diffraction,” *New J. Phys.*, vol. 8, no. 11, p. 272, 2006.

[128] A. Gliserin, A. Apolonski, F. Krausz, and P. Baum, “Compression of single-electron pulses with a microwave cavity,” *New J. Phys.*, vol. 14, no. 7, p. 073055, 2012.

[129] S. Hooker, *Laser Physics.* Oxford Master Series in Physics, 2010.

[130] “NKT Photonics homepage, LMA-35 datasheet.”

[131] A. V. Smith and B. T. Do, “Bulk and surface laser damage of silica by picosecond and nanosecond pulses at 1064 nm,” *Appl. Opt.*, vol. 47, no. 26, pp. 4812–4832, 2008.

[132] C. Saraceno, O. Heckl, C. Baer, T. Südmeyer, and U. Keller, “Pulse compression of a high-power thin disk laser using rod-type fiber amplifiers,” *Opt. Express*, vol. 19, no. 2, pp. 1395–1407, 2011.

[133] D. J. Kane and R. Trebino, “Characterization of arbitrary femtosecond pulses using frequency-resolved optical gating,” *IEEE Journal of Quantum Electronics*, vol. 29, no. 2, pp. 571–579, 1993.

[134] K. S. Kim, W. A. Reed, K. W. Quoi, and R. H. Stolen, “Measurement of the nonlinear index of silica-core and dispersion-shifted fibers,” *Opt. Lett.*, vol. 19, pp. 257–259, Feb 1994.

[135] “NKT Photonics homepage, LMA-15 datasheet.”

[136] “NKT Photonics homepage, LMA-25 datasheet.”

[137] H. Fattahi, *Third-generation femtosecond technology.* PhD thesis, LMU Munich, 2015.

[138] J. Limpert, T. Schreiber, A. Liem, S. Nolte, H. Zellmer, T. Peschel, V. Guyenot, and A. Tünnermann, “Thermo-optical properties of air-clad photonic crystal fiber lasers in high power operation,” *Opt. Express*, vol. 11, no. 22, pp. 2982–2990, 2003.

[139] P. Russell, “Photonic crystal fibers,” *Science*, vol. 299, no. 5605, pp. 358–362, 2003.

[140] J. Limpert, A. Liem, M. Reich, T. Schreiber, S. Nolte, H. Zellmer, A. Tünnermann, J. Broeng, A. Petersson, and C. Jakobsen, “Low-nonlinearity single-transverse-mode ytterbium-doped photonic crystal fiber amplifier,” *Opt. Express*, vol. 12, no. 7, pp. 1313–1319, 2004.

[141] Y. Deng, A. Schwarz, H. Fattahi, M. Ueffing, X. Gu, M. Ossiander, T. Metzger, V. Pervak, H. Ishizuki, T. Taira, *et al.*, “Carrier-envelope-phase-stable, 1.2 mJ, 1.5 cycle laser pulses at 2.1 μm,” *Opt. Lett.*, vol. 37, no. 23, pp. 4973–4975, 2012.

[142] E. M. Dianov, I. A. Bufetov, and A. A. Frolov, “Destruction of silica fiber cladding by the fuse effect,” *Opt. Lett.*, vol. 29, no. 16, pp. 1852–1854, 2004.

[143] R. Kashyap and K. Blow, “Observation of catastrophic self-propelled self-focusing in optical fibres,” *Electron. Lett.*, vol. 24, no. 1, pp. 47–49, 1988.

[144] T. Driscoll, J. Calo, and N. M. Lawandy, “Explaining the optical fuse,” *Opt. Lett.*, vol. 16, no. 13, pp. 1046–1048, 1991.

[145] D. Nodop, C. Jauregui, D. Schimpf, J. Limpert, and A. Tünnermann, “Efficient high-power generation of visible and mid-infrared light by degenerate four-wave-mixing in a large-mode-area photonic-crystal fiber,” *Opt. Lett.*, vol. 34, no. 22, pp. 3499–3501, 2009.

[146] A. Couairon, L. Sudrie, M. Franco, B. Prade, and A. Mysyrowicz, “Filamentation and damage in fused silica induced by tightly focused femtosecond laser pulses,” *Phys. Rev. B*, vol. 71, no. 12, p. 125435, 2005.

[147] O. Pronin, J. Brons, C. Grasse, V. Pervak, G. Boehm, M.-C. Amann, V. Kalashnikov, A. Apolonski, and F. Krausz, “High-power 200 fs kerr-lens mode-locked yb: Yag thin-disk oscillator,” *Opt. Lett.*, vol. 36, no. 24, pp. 4746–4748, 2011.

[148] O. Pronin and A. A. personal communication.

[149] E. Desurvire and J. R. Simpson, “Amplification of spontaneous emission in erbium-doped single-mode fibers,” *J. Lightwave Technol.*, vol. 7, no. 5, pp. 835–845, 1989.

[150] CMN Optics, Jena IOF.

[151] D. Strickland and G. Mourou, “Compression of amplified chirped optical pulses,” *Opt. Commun*, vol. 55, no. 6, pp. 447–449, 1985.

[152] O. Martinez, J. Gordon, and R. Fork, “Negative group-velocity dispersion using refraction,” *J. Opt. Soc. Am. A*, vol. 1, no. 10, pp. 1003–1006, 1984.

[153] G. Pretzler, “Höchstleistungs-kurzpulslaser.” Lecture notes.

[154] I. Ahmad, *Development of an optically synchronized seed source for a high-power few-cycle OPCPA system.* PhD thesis, LMU Munich, 2011.

[155] P. Russbueldt. personal communication.

[156] E. Treacy, “Chirped optical pulses,” *Ann. N. Y. Acad. Sci.*, vol. 168, no. 3, pp. 400–418, 1969.

[157] J. Beránek, M. Hugenschmidt, U. Keller, G. Marowsky, K. Rohlena, W. Schulz, W. Seelig, P. Simon, U. Sowada, S. Szatmári, *et al.*, *Laser Physics and Applications.* Springer, 2007.

[158] M. Pessot, P. Maine, and G. Mourou, "1000 times expansion/compression of optical pulses for chirped pulse amplification," *Optics communications*, vol. 62, no. 6, pp. 419–421, 1987.

[159] S. Karsch, "Generation of high-intensity laser pulses." Lecture notes.

[160] M. Bradler, C. Homann, and E. Riedle, "Broadband difference frequency mixing between visible and near-infrared pulses for few-cycle pulse generation with stable carrier-envelope phase," *Applied Physics B*, vol. 113, no. 1, pp. 19–25, 2013.

[161] J. Tate, T. Auguste, H. Muller, P. Salieres, P. Agostini, and L. DiMauro, "Scaling of wave-packet dynamics in an intense midinfrared field," *Phys. Rev. Lett.*, vol. 98, no. 1, p. 013901, 2007.

[162] A. Shiner, C. Trallero-Herrero, N. Kajumba, H.-C. Bandulet, D. Comtois, F. Légaré, M. Giguère, J. Kieffer, P. Corkum, and D. Villeneuve, "Wavelength scaling of high harmonic generation efficiency," *Phys. Rev. Lett.*, vol. 103, no. 7, p. 073902, 2009.

[163] B. Bernhardt, A. Ozawa, A. Vernaleken, I. Pupeza, J. Kaster, Y. Kobayashi, R. Holzwarth, E. Fill, F. Krausz, T. W. Hänsch, *et al.*, "Vacuum ultraviolet frequency combs generated by a femtosecond enhancement cavity in the visible," *Opt. Lett.*, vol. 37, no. 4, pp. 503–505, 2012.

[164] K. Boller, R.-P. Haelbich, H. Hogrefe, W. Jark, and C. Kunz, "Investigation of carbon contamination of mirror surfaces exposed to synchrotron radiation," *Nucl. Instr. Meth. Phys. Res.*, vol. 208, no. 1, pp. 273–279, 1983.

[165] J. Hollenshead and L. Klebanoff, "Modeling radiation-induced carbon contamination of extreme ultraviolet optics," *J. Vac. Sci. Technol. B*, vol. 24, no. 1, pp. 64–82, 2006.

[166] A. Shiner, B. Schmidt, C. Trallero-Herrero, H. Wörner, S. Patchkovskii, P. Corkum, J. Kieffer, F. Légaré, and D. Villeneuve, "Probing collective multi-electron dynamics in xenon with high-harmonic spectroscopy," *Nat. Phys.*, vol. 7, no. 6, pp. 464–467, 2011.

[167] T. Popmintchev, M.-C. Chen, D. Popmintchev, P. Arpin, S. Brown, S. Ališauskas, G. Andriukaitis, T. Balčiunas, O. D. Mücke, A. Pugzlys, *et al.*, "Bright coherent ultrahigh harmonics in the keV X-ray regime from mid-infrared femtosecond lasers," *Science*, vol. 336, no. 6086, pp. 1287–1291, 2012.

[168] M. Lewenstein, P. Balcou, M. Y. Ivanov, A. Lhuillier, and P. B. Corkum, "Theory of high-harmonic generation by low-frequency laser fields," *Phys. Rev. A*, vol. 49, no. 3, p. 2117, 1994.

[169] P. B. Corkum, "Plasma perspective on strong field multiphoton ionization," *Phys. Rev. Lett.*, vol. 71, no. 13, p. 1994, 1993.

Acknowledgements

First of all I would like to express my deep and sincere gratitude to Prof. Ferenc Krausz who provided lots of good ideas and encouragement. I sincerely appreciate the research opportunities he gave me, his scientific experience, and research insight. I am deeply grateful to Dr. Alexander Apolonski for supervising this thesis. His constructive comments and great ideas contributed greatly to this work. I have the pleasure of thanking Prof. Matthias Kling for the inspiring collaboration with his team and for the encouragement to participate in the DAAD RISE program. Likewise, I am grateful to Dr. Peter Baum for the fruitful discussions we had. His knowledge and experience left a significant mark in this work. I extend my gratitude to Dr. László Veisz for the illuminating discussions regarding SPM GDD and SSFS. I truly appreciate Dr. Nicholas Karpowicz for his help with simulations and data estimation. I am happy to thank Dr. Zsuzsanna Major and Dr. Helena Barros for their great organization and support.

I wish to thank Prof. Peter Hommelhoff, Prof. Ulf Kleineberg, Prof. Toshiki Tajima, Dr. Thomas Udem, and Dr. Vladislav Yakovlev for the inspiring lectures or IMPRS block lectures. I want to express my gratitude to Dr. Ernst Fill for the insights into the theory of OHG generation, and to Dr. Hartmut Schröder for the discussions on the propagation of ultrashort pulses.

I had the chance to collaborate with many very bright and very inspiring colleagues. I am sincerely thankful to Dr. Volodymyr Pervak, Dr. Ivan Angelov, Dr. Elena Fedulova and Dr. Olga Razskazovskaya for the chirped mirrors and their specifications. I want to express my appreciation to Dr. Yunpei Deng, Dr. Hanieh Fattahi, Dr. Oleg Pronin, and Dr. Alexander Schwarz for the laser beam time and fruitful discussion. Also, to Dr. Georg Wachter for the theoretical simulations. I have learned a lot from you, guys! Special thanks to Dr. Victoria Henderson for being such a great summer student and for contributing to this thesis during the summer internship. Special praise to Dr. Harald Fuest, who is a great team player. I profited a lot from his good organization skills and practicality. Particularly, I would like to express my gratitude to Dr. Lénárd Vámos and Dr. Marcus Seidel for helping out with FROG measurements and retrievals, simulations and support in the lab. I want to express my appreciation to the best specialist in electronics and LabVIEW Dr. Alexander Gliserin. Thanks a lot for the LabVIEW batch. I am thankful to Dr. Waldemar Schneider for helping out with his excellent skills in vacuum technology and solid-state lasers. Also, to Dr. Andrey Ryabov for helping out with the pulse-to-pulse stability measurements and the amplifier. I am grateful to Dr. Thomas Ganz for his introduction into the NPC project. Furthermore, I want to thank Roswitha Graf for the calculations with the grating stretcher and compressor and the advice regarding laser alignment. I am grateful to Dr. Peter Rußbüldt, Guido Rotarius, Thomas Sartorius, and Dr. Johannes Weitenberg from ILT Aachen for the laser beam time and the hospitality during my four month stay in Aachen.

I also got to know a number of great researchers, with whom I didn't actually work, but enjoyed spending time together and having interesting discussions with, be it during the LAP or IMPRS meetings. I have the pleasure to thank Dr. Klaus Allinger, Dr. Boris Berques, Dr. Elisabeth Bothschafter, Dr. Jonathan Brons, Dr. Alexander Buck, Dr. Henning Carstens, Dr. Soo Hoon Chew, Dr. Shao-Wei Chou, Dr. Katharina Doblhoff-Dier, Dr. Michael Förster, Dr. Justin Gagnon, Dr. Mohammed Hassan, Dr. Patrick Heissler, Dr. Wolfram Helml, Dr. Johannes Hoffrogge, Dr. Michael Hofstetter, Dr. Florian Holy, Dr. Simon Holzberger, Dr. Christian Homann, Dr. Nicole Humble, Dr. Konrad Hütten, Dr. Sabine Keiber, Dr. Alexander Kessel, Dr. Konstantin Khrennikov, Dr. Friedrich Kirchner, Dr. Constantin Klier, Dr. Nora Kling, Dr. Michael Korbman, Dr. Jindrich Krcmar, Dr. Matthias Kübel, Dr. Hui Li, Dr. Mattia Lupetti, Dr. Tran Trung Luu, Dr. Andreas Mair, Dr. Antoine Moulet, Dr. Tim Paasch-Colbert, Dr. Renate Pazourek, Dr. Kellie Pearce, Dr. Antonia Popp, Dr. Ioachim Pupeza, Dr. Sebastian Raith, Dr. Annkatrin Sommer, Dr. Frederik Süßman, Dr. Markus Schenk, Dr. Wolfgang Schweinberger, Dr. Moritz Ueffing, Dr. Matthew Walbran, Dr. Johannes Wenz, Dr. Jasper Werhahn, Dr. Alissa Wiengarten, Dr. Sergey Zherebtsov, Dr. Irina Znakovskaya.

I appreciate Wirgler Klaus, Tobias Kleinhenz and Dr. Johannes Wulz for the technical drawings and their time for consultations on optical holders. Their excellent knowledge on materials and their properties were very helpful in planning unique mounts. I am grateful to the LMU mechanical workshop for the realization of the specially designed components. I want to express my gratitude to Anton Horn for his patience and his excellent work with the electronics for the laser system.

Moreover, I thank Katharina Adler, Klaus Franke, and Petra Mayrhofer for their help in placing the orders and the help to organize the trips. Thorsten Naeser for the professional and representative pictures of the lab and Monika Wild for the organization of the IMPRS annual meetings.

I am grateful to NKT Photonics for the prototype of the passive LMA-100 fiber. Also, I acknowledge the funding from the Munich-Centre for Advanced Photonics.

Last but not least, I am very grateful to my family for their love, patience and encouragement during these years. Thank you for being by my side and providing endless support.